Quantification of Collagen Fiber Morphologies in Human Arterial Walls: Novel Experimental Methodologies with 2D and 3D Structural Data

Zur Erlangung des akademischen Grades des
Doktors der technischen Wissenschaften

eingereicht an der
Fakultät für Elektrotechnik und Informationstechnik
der Technischen Universität Graz

von

Dipl.-Ing. Andreas Jörg Schriefl, B.Sc.

Betreuer: Univ.-Prof. Dipl.-Ing. Dr.techn. Gerhard A. Holzapfel

Graz, Dezember 2012

EIDESSTATTLICHE ERKLÄRUNG

Ich erkläre an Eides statt, dass ich die vorliegende Arbeit selbstständig verfasst, andere als die angegebenen Quellen/Hilfsmittel nicht benutzt und die den benutzten Quellen wörtlich und inhaltlich entnommenen Stellen als solche kenntlich gemacht habe.

Graz, am ....

Datum Unterschrift

STATUTORY DECLARATION

I declare that I have authored this thesis independently, that I have not used other than the declared sources/resources and that I have explicitly marked all material which has been quoted either literally or by content from the used sources.

Graz, ...

Date Signature

Preface

Three years ago after having completed my Master's in Engineering Physics, I noticed an announcement for a PhD position at the Institute of Biomechanics, calling for candidates interested in experimental research of the human cardiovascular system. Intrigued by the topic I looked into it more closely and realized quickly that I would be working in a small but highly diverse and multicultural group, where the working language was English; which for someone who is married to a Canadian, was right up my alley. It was after the interview that I became certain that this position would not only be interesting from an engineering perspective, but that the outcome could be clinically relevant and, therefore, constitute also a meaningful contribution to the advancement of health care for society. Three years later I feel that I have been able to contribute my small share towards this goal, none of which would have been possible without the help, support and guidance of many people.

I would like to begin by thanking my wife who, of all people, has supported me every day throughout my PhD, not only by proofreading my publications but also by actively maintaining a constant and sincere interest in my work. Together with my family I was given as much moral support as anyone could hope for.

Special thanks is owed to all the collaborators on my peer-reviewed publications for their highly productive and efficient working style, namely, Georg Zeindlinger, David M. Pierce, Melissa J. Collins, Laura E. Niklason, Andreas J. Reinisch, Sethuraman Sankaran, Heimo Wolinski and Sepp D. Kohlwein.

This work would not have been possible without the competent team at the Institute of Pathology, Medical University Graz. I owe special gratitude to Prof. Peter Regitnig for his support and medical expertise throughout the years and to the team of Augustin Donnerer for regularly providing me with the required valuable human tissues for my research.

During my second year I was honored to have spent four months performing research at the Yale School of Engineering and Applied Science at Yale University under the guidance of Prof. Jay D. Humphrey, to whom I am very grateful for providing such a welcoming, open and highly motivating research environment. Despite my relatively short stay, I still felt like part of the team and to that end I would especially like to thank my colleagues there: Jacopo Ferruzzi, David Simon, Sara Roccabianca, Yongung Lee and John Wilson.

I would also like to thank all of my colleagues in Graz, namely Michael J. Unterberger, Arturo Valentin, Gerhard Sommer, Jianhua Tong, Thomas Eriksson, Hannah Weisbecker and Bettina Strametz for their insightful contributions and continuous openness to questions. I can honestly say that working with all of you has made the last three years a uniquely positive experience and I feel very lucky to have gotten to know many of you better during this time.

Finally, I want to express my sincere gratitude to my supervisor Prof. Gerhard A. Holzapfel. As the head of the Institute of Biomechanics it was you who took a chance on me, a physicist with limited experience in Biomedical Engineering, and it was your intimate knowledge of the field and sense of direction that put me on the path that allowed me to work most efficiently during my PhD.

Andreas Jörg Schriefl
Graz, December 2012

Abstract

The arterial wall consists of three major microstructural components, collagen, elastin, and smooth muscle cells; all of which play important roles in the cardiovascular function of health and disease. From a biomechanical perspective, collagen with its high tensile strength constitutes the most important component, endowing the arterial wall with strength and load resistance. Changes in the mechanical properties of a healthy wall play a role in pathological and degenerative processes such as increased wall stiffness, atherosclerosis, or enlargement of intracranial aneurysms. To that end we studied the fundamental role of collagen in intramural healing through the remodeling processes of arterial or aneurysmal dissections in an apolipoprotein-E null mouse model. A meaningful quantification of morphological collagen data in healthy arteries is fundamental to a better understanding of the underlying mechanical principles governing the biomechanical response of the vessel wall. Furthermore, such data can be utilized for modeling of the cardiovascular system and to increase our understanding of disease progression.

Towards obtaining such data we started with the quantification of collagen fiber angles in the human thoracic and abdominal aorta and common iliac artery, using a well established experimental approach based on measuring (by hand) individual fiber angles from histological sections through polarized light microscopy in combination with a universal stage. The study yielded mean data for each of the three individual layers of the arterial wall, which was quantified using a dispersion model.

In trying to overcome several limitations inherent to this traditional method, we began to develop an automatic approach for the quantification of collagen fiber distributions from 2D images. Not only were we able to speed up the measuring process, but the new method also enabled us to assess and evaluate entire fiber distributions among varying length-scales using statistical approaches, which has implications for numerical modeling, e.g., on determining appropriate mesh densities.

Finally, we hoped to move beyond a two-dimensional quantification of collagen structures by trying to obtain image stacks throughout the entire thickness of a human arterial wall. The major experimental challenge to overcome was the limited application of optical techniques to assess the orientation of collagen throughout approximately $800 - 1500\,\mu$m of non-transparent wall tissue. We succeeded by developing a novel approach which combines a new sample preparation method with optical tissue clearing and subsequent imaging using second-harmonic generation microscopy. To extract and quantify the morphological collagen structures from image stacks we advanced our 2D image analysis approach, now yielding a 3D distribution of amplitudes (1° resolution) representing the orientations of the collagen fibers throughout the tissue. With that we can now identify isotropic regions in the tissue where no preferred fiber orientations are observed and quantify regions of anisotropy by calculating structural parameters which can directly be utilized in numerical codes using fiber-reinforced constitutive laws.

Kurzfassung

Die menschliche Arterienwand setzt sich vor allem aus den drei Hauptkomponenten Kollagen, Elastin und glatten Muskelzellen zusammen. Alle Drei spielen eine wichtige Rolle in der gesunden sowie kranken kardiovaskulären Funktion, wobei Kollagen auf Grund der hohen Zugfestigkeit die aus biomechanischer Sicht wichtigste Komponente darstellt. Es verleiht der Arterienwand die notwendige Festigkeit und Resistenz gegen Belastungen. Veränderungen der mechanischen Eigenschaften von gesunden Arterienwänden können zu degenerativen sowie pathologischen Prozessen führen, wie zum Beispiel der Versteifung der Arterienwand, Atherosklerose, oder der Ausdehnung von intrakraniellen Aneurysmen. Diesbezüglich untersuchten wir die Rolle des Kollagens in der Stabilisierung von intraarteriellen Aneurysmen an genetisch modifizierten (ApoE -/-) Mäusen. Eine sinnvolle Quantifizierung morphologischer Kollagendaten ist essenziell für ein besseres Verständnis zugrundeliegender Prinzipien der Arterienwandmechanik. Weiters können solche Daten zur Modellierung des kardiovaskulären Systems verwendet werden und dadurch helfen Krankheitsverläufe besser verstehen zu lernen.

Um solche Strukturdaten zu erfassen, begannen wir mit der Quantifizierung von Kollagenfaserwinkeln an histologischen Präparaten von menschlichen thorakalen und abdominalen Aorten und Beckenarterien mittels der traditionellen Methode der Polarisationsmikroskopie. Aus der Studie folgten schichtenspezifische, gemittelte Faserverteilungen, welche anhand eines Dispersionsmodelles quantifiziert wurden. Um damit einhergehende Limitationen und den enormen Zeitaufwand der Messungen zu verbessern wurde eine automatisierte Bildverarbeitungsmethode entwickelt die es schafft, Kollagenfaserverteilungen aus 2D Bildern zu extrahieren. Dadurch haben sich einerseits die Messzeiten um ein vielfaches verkürzt, andererseits ermöglichte die neue Methode auch eine statistische Analyse der Strukturdaten über verschiedenen Längenskalen, was in der numerischen Modellierung Vorteile bringt wie zum Beispiel im Bestimmen von Netzdichten.

Letztendlich wollten wir über eine zweidimensionale Quantifizierung hinaus gehen, indem wir versuchten Bilderstapel (z-stacks) durch die ganze Arterienwanddicke zu erzeugen. Die experimentelle Herausforderung dabei war durch den beschränkten Anwendungsbereich optischer Methoden zum Erfassen der Kollagenstrukturen in nicht transparenten Arterienwänden mit Dicken zwischen $800 - 1500\,\mu$m gegeben. Dies gelang schlussendlich durch die Entwicklung einer umfassenden Methode, die sich aus einer neuartigen Probenpräparation, dem Durchsichtigmachen der Präparate und der Bildaufnahme mittels Multiphotonenmikroskopie zusammensetzt. Um die Morphologie der Kollagenstrukturen von den Bilderstapeln zu extrahieren und quantifizieren wurde die 2D Bildverarbeitungsmethode weiterentwickelt, sodass wir jetzt eine 3D Amplitudenverteilung erhalten, welche einerseits die Faserorientierungen innerhalb der Arterienwand widerspiegelt und zusätzlich Informationen bezüglich isotropen und anisotropen Bereichen im inneren der Arterienwand liefert, die in der numerischen Modellierung direkt verwendet werden können.

CONTENTS

1 INTRODUCTION AND MOTIVATION

1.1 Fibrillar Collagen

1.1.1 Synthesis and assembly

Collagen is a structural protein containing at least one domain in the triple helical conformation, constituted by three polypeptide chains (α chains). The central collagen domain consists of repeating Gly-Xaa-Yaa triplets, a high concentration of proline, alanine, and lysine residues with non-collagenous domains at their terminal ends [1, 2]. In humans, 28 different types of collagen have been detected to date, which can be categorized according to their structural properties [3]:

- Fibrillar: Type I, III, V
- Sheet-forming: Type IV, VIII
- Fibril-associated: Type XV, XVIII, XIX
- Microfibrillar: Type VI

While the major types in human vasculature are the classical fibrillar types I and III [4], generally the arterial collagen content and distribution is species-dependent [5].

Most collagens in the intima and media of vascular walls are synthesized by smooth muscle cells and in the adventitia by fibroblasts [6]. The secreted procollagen molecules have their non-collagenous domains removed by specific proteinases, leaving the characteristic collagen triple helices aggregate in quarter-staggered fibrils. Regarding their biomechanical properties, the newly formed collagen fibrils initially have no tensile strength (and are still soluble). Only during the subsequent formation of both inter- and intramolecular covalent cross-links does their tensile strength progressively increase (and they become increasingly insoluble) [7]. This final stage in the biosynthesis of fibrillar collagens is mostly initiated by members of the lysyl oxidase family of copper-dependent amine oxidases [8, 9], which is another multifunctional enzyme involved in collagen cross-linking is tissue transglutaminase [10].

The driving factor in the self-assembling collagen fibril formation is entropy. The process can be characterized by three phases: first, a lag phase during which collagen molecules associate to form a metastable nuclei; second, a rapid growth phase during which more

molecules accrete around the nuclei followed by growth in fibril length and width and third, a plateau region where no further growth is observed [11].

1.1.2 Hierarchical structure

The tensile properties of fibrillar collagen mostly serve biomechanical roles in tissues (note that the structural signaling roles of collagen are less well understood). Its mechanical properties are grounded in the structural organization within a collagen fibril with its characteristic axial and lateral organization and topology [12, 13]. Structural details of the fibril are complex but some key structural features can be observed that are shared by almost all fibrillar collagens. Foremost is its characteristic 67 nm *D*-spacing (or *D*-period) along the axial orientation, visible as highly regular alternating electron densities in projection regions of electron micrographs [14]. These overlap and gap regions arise from the repeating molecular stagger between five 300 nm-long collagen molecules. The resulting 234-amino acid pseudo-periodicity within the fibrillar collagen sequence is key to ideal electrostatic pairings between adjacent triple helices and maximizes the contact between hydrophobic regions [15–19].

Fibril length and diameter vary greatly depending on anatomical location, and the reasons for this wide distribution are not well understood. Estimating an effective fibril length has been proven difficult, as the following quote illustrates: 'Analysis of groups of collagen fibrils within individual micrographs from mature tendon or ligament did not reveal any fibril ends. Examination of consecutive overlaid micrographs from mature medial collateral ligaments did not reveal any collagen fibril ends. In addition, evaluation of consecutive overlaid micrographs from mature tendon did not reveal any collagen fibril ends. Combined, 7275 fibrils were examined at high magnification ($10,000 - 50,000\times$) over a total combined tissue length of approximately 2.1 mm without revealing an end in mature tissue. These data show that unlike fetal tissues, virtually all of the collagen fibrils in mature ligament and tendon are very long' [20]. Fibril diameters are known to increase with maturation of the tissue [21], are also dependent on anatomical locations, and reported thickness values range from 50 to a few hundred nanometers (see [22] and references therein).

Collagen fibers consist of a group of collagen fibrils bound together by a matrix rich in proteoglycans, which also contribute to the mechanical properties of the fibers. Within the fiber, fibrils are mostly (but not only) oriented longitudinally, running in various directions, e.g., parallel, across each other, forming spirals, cross-plys or even spiral-type plaits [23]. This hierarchical organization, from collagen molecules to fibers, continues, for example, in tendons where several fibers are bound together to form primary fiber bundles which are again bound together to form secondary fiber bundles and so forth [23, 24].

1.1.3 Mechanical properties

The hierarchical structure of collagen fibers, built of parallel fibrils which themselves are aggregates of parallel collagen molecules, leads to important consequences regarding the mechanical properties of the fiber. Firstly, the ultimate strength of a single collagen fiber is not affected by its subdivision into multiple, parallel threads [25]. Secondly, the hierarchical structure yields the so-called Cook-Gordon effect, describing the stopping of an occasional crack at the surface of each fibril, therefore making it harder for a crack to propagate across an entire fiber. Thirdly, the flexibility of collagen fibers is significantly increased because it is directly proportional to the fibril number and inversely proportional to the fourth power of the radius [22, 25]. With an ultimate tensile strength in the range of $50 - 100\,\mathrm{MPa}$ [26], an excellent elastic resilience [27], and the tiny size of the fibrils, collagen fibers are uniquely suited to withstand high tensile stresses and simultaneously endow the extracellular matrix with a high compliance.

A typical stress-strain curve of collagen (e.g., from a tendon) shows a nonlinear behavior which can be subdivided into three regions [28, 29]. An initial 'toe' region is observed for small strains, where little force is needed for the extension of fibers due to the removal of macroscopic crimps of the fibrils [30]. Next comes the so-called 'heel' region, corresponding to a straightening of molecular kinks in the gap [31], followed by a 'linear' region where molecular gliding within the fibrils takes place until the rupture of the structure [32].

1.1.4 Optical properties

The birefringent properties of collagen have long been known and were first described by the Scottish naturalist and clergyman Sir David Brewster in 1847 [33]. Birefringence denotes the optical property of a material in which the refractive index is dependent on the polarization and propagation direction of light. Collagen type I exhibits *positive, intrinsic* and *form birefringence* with respect to the length of the fibrils [34], three terms that require a more detailed definition: (i) positive birefringence means that in an elongated structure (e.g., fibril) the light velocity is higher in a plane parallel to the length of the structure; (ii) intrinsic birefringence denotes the effect on the velocity of light caused by different chemical groups in a ordered configuration; (iii) form birefringence arises when rod- or plate-like structures are immersed in a medium with a different refractive index. The intensely positive birefringence of collagen is caused by the superimposed right-handed superhelix of the left-handed helix consisting of the three polypeptide chains, yielding a consequent alignment of the amino acid chains approximately parallel to the molecular axis [35, 36].

The birefringent properties can be intensified when treated with certain stains. Most marked changes were caused with Picrosirius red stain, an acid dye increasing the pos-

itive birefringence of collagen [37–39] (note: original claims by the authors that collagen type I and III could be distinguished based on different polarization colors had to be retracted later, because it turned out that the color changes were in fact a due to different fiber widths).

Besides possessing birefringent properties, collagen is also a well-documented source of tissue second-harmonic generation (SHG) [40–42] and autofluorescence [43–45]. Both types of nonlinear light-matter interactions (SHG and two-photon excited autofluorescence) are utilized in the multiphoton microscopy (MPM) technique [46–48] to yield high contrast and optical sectioning capabilities. Importantly, it is a completely non-destructive method which does not require the addition of contrast agents, rendering it well suited for the determination of collagen-based morphometric features [49, 50].

1.2 The Healthy Arterial Wall

Generally, arteries can be classified into three types based on their properties and sizes, namely *elastic arteries*, *muscular arteries*, and *arterioles* [51]. The group of elastic arteries consists of the larger vessels closer to the heart and exhibits distinct elastic properties (hence their name). They include the ascending, thoracic and abdominal aorta, the branches originating from the aortic arch, and the pulmonary artery. Their elastic properties are crucial for the smoothing of pulsating blood pressure waves (systolic-diastolic) originating from the heart, exposing them to high circumferential elastic strain. The group of muscular arteries is located closer to the periphery and includes the carotid, brachial, iliac, and the coronary arteries. Their function includes the regulation of blood flow via vasoconstriction or vasodilatation, mediated mainly by their smooth muscle cells. The last group, the arterioles, are the smallest type of arteries and part of the microcirculation, leading to the capillaries where the exchange of oxygen, water, and other nutrients takes place. Arterioles have a small lumen and a thick muscular wall, making them the primary site of peripheral resistance to blood flow which is again regulated via vasoconstriction or vasodilatation [52–55].

The walls of healthy arteries consist of three concentric layers: the *tunica intima* (innermost layer), *tunica media* (middle layer), and the *tunica adventitia* (outermost layer). A representative schematic is provided in Fig. 1.1.

1.2.1 Tunica intima

The region from and including the endothelial surface at the lumen to the luminal margin of the media constitutes the tunica intima. The border to the media is formed by the internal elastic lamina, which generally is considered to be part of the media [57]. In newborns

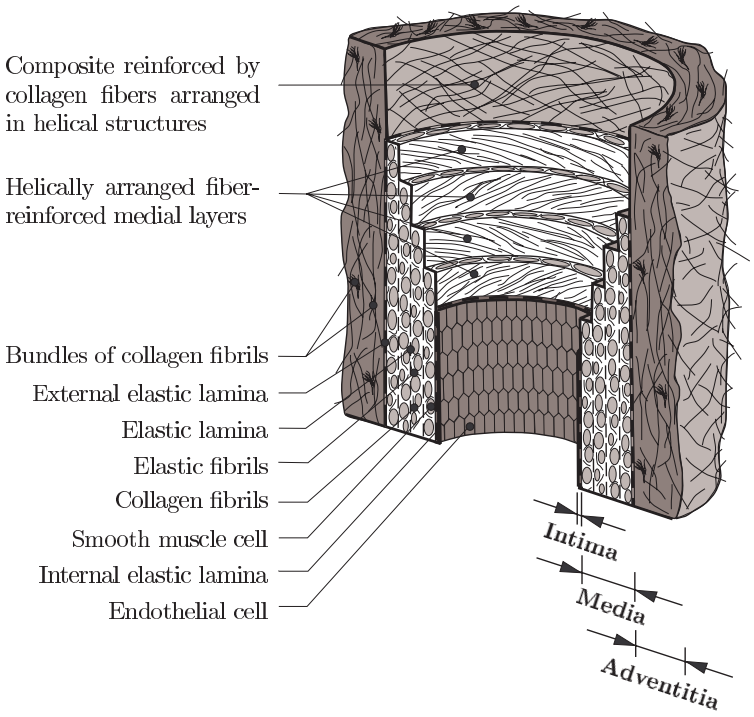

Figure 1.1: Schematic of the arterial wall featuring the three concentric layers, the *tunica intima*, *tunica media*, and the *tunica adventitia* and other major components of a healthy elastic artery (Figure with permission from [56]).

and very young arteries the intima is a single layer of endothelial cells attached to a thin collagenous basal lamina. At this healthy stage it has no structural importance to the vessel wall but only becomes mechanically significant with aging and the onset of arteriosclerosis [58]. Its main purpose is to provide a non-clotting interface between the blood stream and the vessel wall and simultaneously is a gateway for the transport of nutrients from and to the bloodstream [54].

1.2.2 Tunica media

The media is situated between the internal elastic lamina (the border to the intima) and the external elastic lamina (the border to the adventitia). Structurally, it is comprised of a complex three-dimensional network of collagen fiber bundles, elastin and smooth muscle cells [52]. The three components are organized in a varying number of medial lamellar units [59]. Mechanically, at physiological *in vivo* pressures the media is the most significant layer due to its more circumferentially oriented collagen fibers [56]. Quantifying the orientations of collagen fibers in arterial walls was the main focus of this dissertation, therefore, an extensive and detailed discussion regarding the structural organization of collagen within the media can be found in subsequent chapters.

1.2.3 Tunica adventitia

The adventitia consists of a network of mostly collagen type I fiber bundles [60], interspersed with fibroblasts, fibrocytes, histological ground matrix, some elastic fibers, nerves, and vasa vasorum providing the vessel with its blood supply [54, 55]. Its thickness is dependent on the type of artery and, therefore, on its anatomical location. In human aortas, the thick collagen fiber bundles are often organized as two counter-rotating fiber families, mostly oriented between the major axes of the vessel [61]. Mechanically, the looser adventitia adds further structural integrity to the arterial wall by forming a 'jacket-like' tube at increased blood pressures [56]. A detailed discussion of the morphological features and structural organization of collagen fibers in the adventitia can be found in subsequent chapters.

1.2.4 Collagen and the biomechanical response of arterial walls

From a biomechanical perspective, the healthy arterial wall is a deformable composite structure, exhibiting a highly nonlinear stress-strain response with a characteristic (exponential) stiffening at higher pressures [56]. The reason for this nonlinear gradual stiffening effect is the progressive recruitment of the embedded wavy collagen fibers, the main load-carrying element in the arterial wall. Anisotropic behavior of arterial segments was first reported by [62] on dog specimens, later it was the classical work by Roach and Burton [63] that identified the individual contributing tissue components to the overall nonlinear response of human arteries. At low pressures, stress is almost independent of strain causing even small tension loadings to produce large extensions. In this region the mechanical behavior is (mostly) governed by the elastic tissue components. With increasing strains at higher blood pressures the load is progressively carried by collagen fibers, which are continuously straightened and become increasingly more aligned leading to the characteristic stiffening effect and the anisotropic mechanical behavior [56, 64].

The stress-strain regime of arterial walls can be divided into two domains: the (visco)elastic domain in which cyclic loading and unloading is associated with initial stress softening effects (in, e.g., typical uniaxial extension experiments) causing a pre-conditioning of the tissue which subsequently behaves (perfectly) elastically or viscoelastically [58]. When loading beyond the (visco)elastic regime we enter the inelastic domain, in which the material undergoes inelastic deformation (e.g., elastoplastic and/or damage mechanisms) causing significant irreversible changes in the mechanical behavior [65]. Such deformations are far beyond the range of physiological loading but often occur during surgical treatments such as percutaneous transluminal angioplasty [66, 67].

It should be mentioned that in addition to collagen and elastin, also smooth muscle cell contraction/relaxation yields active forces which contribute to the mechanical stability of the vessel and influence the diameter and flow resistance, especially in anatomical regions

further removed from the heart where arteries become increasingly muscular [68, 69]. While its contractile function is less well explored, efforts are being undertaken to increase our understanding of its role and contribution in arterial mechanics through computational models [70–73].

The mechanical response of the vessels is not only dependent on different regions of the same arteries, but variations in both the structural composition and mechanical properties have been reported for different species [74–76], different ethnic groups [57], and are also expected among different age groups of a single species [77, 78].

1.3 Age Related Changes and Pathological Considerations

1.3.1 Adaptive intimal thickening

Non-pathological intimal thickening in the human aorta was first reported in 1883 by Thoma [79], describing it to be a universal feature in human arterial development [80]. Similar intimal thickening was later reported by Wolkoff [81, 82] in 1923/24 for coronary arteries of infants, children, adults, as well as in different animal species.

Adaptive intimal thickening can be differentiated into two types: focal (eccentric) and more extensive (diffuse). Eccentric thickening denotes a sudden and focal increase in the intima thickness, often associated with orifices or arterial branches. Diffuse thickening on the other hand is more spread-out, not specific to certain anatomical locations such as orifices or branches and often shows a circumferential pattern. Generally, both types of intimal thickening can not easily be distinguished because they run into one another, while sometimes they are clearly identifiable. In any case they represent physiological adaptations to changes of flow and/or wall tension that do not obstruct the lumen [57]. Other terminologies for adaptive intimal thickening that include both types (eccentric and diffuse) are: musculoelastic intimal lesion [83], musculoelastic intimal thickening [84], musculoelastic layering [85] or fibromuscular intimal thickening [86].

The reason for adaptive intimal thickening has been attributed to a variety of physiological stimuli. The intima constitutes a reactive tissue component at the luminal border of the arterial wall which corresponds to hemodynamic alterations as well as altered mechanical wall stresses. It adapts its thickness in an attempt to maintain ‘normal’ conditions [87, 88]. Evidence suggests that locations of eccentric and diffuse intimal thickening might be an adaptive response to reduced wall shear stress. On the other hand, a smaller lumen diameter caused by intimal thickening could lead to elevated blood flow velocity as an attempt to restore normal baseline values [89].

From a biomechanical perspective, a thickened intima becomes mechanically increasingly important [56] and could strengthen the arterial wall in response to increased tensile

stresses in order to keep such values constant. As part of a remodeling process, the intima will adapt locally to changes in mechanical stimuli, which helps explain the evenly distributed, diffuse thickening observed in straight arterial segments versus the local and eccentric thickening at arterial branches and bifurcations, where both shear and tensile stresses are not uniformly distributed [57].

1.3.2 Atherosclerosis

Atherosclerosis denotes a chronic disease of the arterial wall, constituting the leading cause of death and resulting in reduced life span worldwide. The development of atheromatous plaques in the intima of arterial walls is referred to as atherogenesis. Our current understanding of atherogenesis in humans begins with an initial change in the endothelial cell monolayer, the inner lining of the intima and interface between the blood stream and the vessel wall [57]. Instead of resisting white blood cells streaming past them, the changed endothelial cells express adhesion molecules leading to the attachment of leukocytes on their surfaces. At the same time endothelial permeability and the extracellular matrix composition change, leading to an increased entry of cholesterol-containing low-density lipoproteins (LDL) into the vessel wall [90]. Intracellular cholesterol accumulation is promoted via leukocyte adhesion as well as particle endocytosis through monocyte-derived macrophages. Leukocytes migrate to the intima, directed by upregulated chemokines (chemotactic movement). Once the numerous monocytes enter the arterial wall they begin to differentiate into tissue macrophages. The macrophages (mononuclear phagocytes) engulf lipoproteins, turning them into lipid-laden foam cells [91, 92]. Additionally, the atheroma formation involves the recruitment of smooth muscle cells (SMCs) which are part of the intima in human arteries (unlike in many animal models such as, e.g., mice, where SMCs migrate from the adventitia to the intima during lesion formation [93]).

Intimal SMCs secrete extracellular matrix proteins such as interstitial collagen and elastin, and form a fibrous cap covering the plaque consisting of a collection of foam cells, lipids and dead cells. Efferocytosis is a process describing the inefficient clearing of dead cells, leading to the formation of a necrotic core within the plaque containing cell debris and extracellular lipids. Advanced plaques include cholesterol crystals and microvessels and can ultimately rupture, enabling tissue factors to come in contact with blood coagulation components, triggering thrombus formation into the lumen of the vessel where it can lead to flow-limiting stenoses [91, 92].

While advanced lesions may lead to symptoms for the patient, preceding lesions are generally clinically silent. The precursors of advanced lesions can be divided into several types, as illustrated in Fig. 1.2 [94, 95]:

1. Type I lesions contain increased macrophages and scattered (macrophage derived) foam cells, preferably at locations showing adaptive intimal thickening.

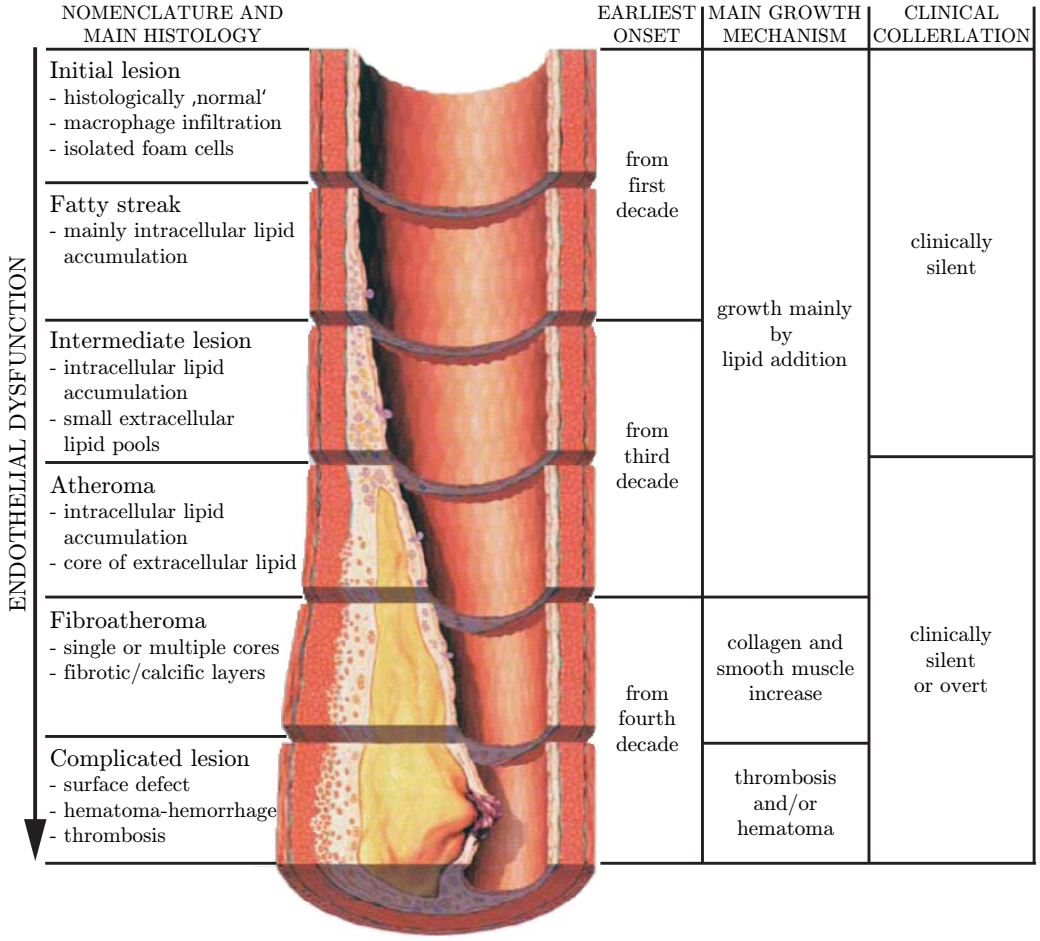

Figure 1.2: Illustration of an artery showing six types of progressively severe lesions. Adapted from the Wikimedia Commons file *Endo dysfunction Athero.png*.

2. Type II lesions consist of layers of foam cells and lipid-laden smooth muscle cells and include fatty streaks.

3. Type III lesions contain scattered groups of extracellular lipid droplets and particles, disrupting the coherent intimal SMCs.

4. Type IV lesions, also known as atheromas, can be symptom-producing and are characterized by a larger, confluent, and more disruptive core of extracellular lipid.

5. Type V lesions generally have a lipid core including thick layers of fibrous connective tissue and/or fissures and hematomas. Some are largely calcified (type Vb), while others consist of fibrous connective tissue with little to no lipid or calcium content (type Vc).

6. Type VI lesions contain hematomas/hemorrhages, surface defects and/or thrombi.

1.3.3 Abdominal aortic aneurysm

An arterial aneurysm denotes a focal expansion of the blood vessel compared to the original shape of the artery. While aneurysms can occur at different locations (e.g., cerebral aneurysm, thoracic aneurysm, etc.), this brief overview focuses on the abdominal aortic aneurysm (AAA) which is defined as a dilatation of the abdominal aorta by at least 50% at the height of the renal arteries [96]. AAAs are a common and life-threatening degenerative disease [97], causing over 4500 deaths each year in the United States alone due to AAA rupture [98].

Among others, the major risk factors associated with AAAs include smoking, age, sex and ethnicity. Among these, smoking was reported to be most influential with a direct relation between the number of years of smoking and AAA formation [99]. AAA risk shows a dramatic increase for age groups above 60 and is besides smoking also often linked with pulmonary emphysema, coronary artery disease, and advanced (occlusive) atherosclerotic lesions [99–101]. It takes years for an AAA to arise, partially because the gradual degeneration of the aortic wall is a complex process which includes destructive remodeling of the connective tissue [102]. Four factors have been identified which are believed to play a role during the pathological remodeling process [103]:

1. Chronic inflammation, especially within the adventitia, accompanied by neovascularization and an upregulation of proinflammatory cytokines.
2. Significant (local) upregulation and dysregulation of matrix-degrading proteinases.
3. Continuous digestion of the major structural matrix proteins, specifically collagen and elastin, resulting in a weakening and widening of the vessel wall.
4. Depletion of SMCs in the media of the aortic wall.

While the exact initiation event triggering the pathological process is unclear, it seems that a medial and adventitial deposition of inflammatory cells is crucial during the early stages of the pathogenesis [93, 104]. Once an inflammation is present and matrix degradation has begun, chemoattractant molecules are released amplifying the amount of inflammatory cells in the outer aortic wall [105].

Currently, the strongest indicator of the AAA rupture risk is the size of the aneurysm. Based on statistical evidence, the Joint Council of the American Association for Vascular Surgery and Society for Vascular Surgery released the following estimation for AAA rupture risk as a function of the AAA diameter [106]:

- Less than 4.0 cm in diameter $\Rightarrow$ 0%
- 4.0 cm to 4.9 cm in diameter $\Rightarrow$ 0.5% to 5%
- 5.0 cm to 5.9 cm in diameter $\Rightarrow$ 3% to 15%

- 6.0 cm to 6.9 cm in diameter $\Rightarrow$ 10% to 20%
- 7.0 cm to 7.9 cm in diameter $\Rightarrow$ 20% to 40%
- 8.0 cm in diameter or greater $\Rightarrow$ 30% to 50%

Besides its size, the rate of expansion of an AAA could also be an indicator for the rupture risk [107]. An AAA expanding by more than $\sim$ 1 cm per year is considered to be in the high risk group regarding AAA rupture [96]. Treatments of high risk AAAs include regular observations, medical therapy, surgery and endovascular stenting.

1.3.4 Genetic collagen diseases

Collagen has a very large and complex mutation spectrum which can lead to a whole range of clinical syndromes. For example, fragile bone structure is often due to anomalous or insufficient collagen formation and the biomechanical properties of collagen are affected by variations in collagen fibril structure, deficient mineralization, and/or altered cellular processes. Without a fundamental understanding of collagen synthesis, secretion and assembly, a correct and full comprehension of the pathological conditions arising from genetic mutations (such as altered COL1A1 and COL1A2 genes) will remain difficult to accomplish [108]. Additionally, processes involved in the collagen assembly to macroscopic hierarchical structures (collagen molecules to fibril to fiber, etc.) and its cross-linking and interactions with the extracellular matrix are still not fully understood [109].

Generally, pathologies based on collagen abnormalities lead to severe consequences because collagen constitutes one of the major structural proteins of most human soft tissues (e.g., a collagen type I defect can affect bone, skin, eyes, dentin, tendons, ligament, blood vessels and ears). Collagen mutations have been reported for all types of fibrillar collagens [110] and result in a broad spectrum of diseases including osteogenesis imperfecta (OI, a condition leading to bone fragility and reduced bone mass) and some forms of osteoporosis. Besides bone related pathologies, diseases involving the 'OI phenotype' include vascular complications, hearing abnormalities, translucent skin, blue sclera, dentin abnormalities and hyperlaxity of ligaments and skin [111]. A large number of pathogenic mutations have been reported for the COL1A1 and COL1A2 genes, some of the better known associated diseases include Marfan syndrome [112], cervical artery dissection [113], and Caffey disease [114]. Additional better known 'collagen diseases' including the involved collagen types are summarized in Table 1.1 [108].

Disease	Collagen type	Phenotype
OI	I	Brittle bones, blue sclera, dentin defects, short stature
EDS	I, III, V, VII	Joint laxity, bruising, vascular complications
SEDS, MEDS	II, IX, X, XI	Growth plate and growth abnormalities
		Abnormal cartilage calcification
		In Stickler syndrome ocular defects
EB	IV, VII	Skin blistering
Alport Syndrome	IV	Renal and basement membrane disease

Table 1.1: Selected overview of some better known 'collagen diseases', including their associated collagen type and phenotype. OI: osteogenesis imperfecta, EDS: Ehlers-Danlos Syndromes, SEDS: spondyloepiphyseal dysplasia, MEDS: metaphyseal spondylodysplacia, EB: epidemylosis bulosa.

1.4 Collagen Structure in Constitutive and Numerical Modeling

The mechanics of biological systems have been studied since the antiquity by Aristotle, but it was the combination of the rise of computers and the early work by Fung in the 1960's and thereafter who coined the term biomechanics and gave birth to biomechanical modeling [115–119]. State of the art numerical modeling of soft biological tissues is utilized for simulations of biological functions which helps to improve our understanding of, e.g., growth and remodeling processes or the development and progression of various diseases such as AAAs. One day patient specific simulations might potentially help guide clinicians in their treatment choices or even during surgical procedures.

1.4.1 Continuum mechanical framework

Numerical modeling of soft biological tissues is mostly performed within the framework of continuum mechanics. Within this framework the soft tissue is treated as a continuum in which the behavior of individual particles is translated into the overall behavior of the continuum. The model does therefore not capture the 'true' physical state of the tissue at an atomistic level, instead, in continuum mechanics a point in space denotes a finite volume around this point. This volume, on the one hand, has to be large enough to include a sufficient number of atoms or molecules necessary to yield macroscopic behaviors such as material density or hydrostatic pressure. On the other hand it has to be small enough to justify the analytical treatment of problems within this framework. In the case of arterial mechanics this means that $\delta/\Delta \ll 1$, with δ denoting the lengths of tissue components at a microscopic scale (e.g., cells) and Δ denoting the lengths at the macroscopic scale of arteries (e.g., the circumference length of an artery).

In the following an overview of the basic relations in kinematics and stress measures is provided, essential for understanding subsequent sections on constitutive equations and

structural models for arterial walls. Since neither biomechanical testing nor numerical modeling is the main focus of this work, the overview is kept brief but will include appropriate references for further reading on this subject. A solid and detailed foundation on continuum mechanics is provided in the book by Holzapfel [120].

Kinematics

We define a continuum body $\mathcal{B} = \{P_k\}$ consisting of a discrete set of particles $\{P_k\}$. The Euclidean space in which the body is located has an origin O from which it is spanned by the orthonormal basis vectors $\mathbf{e}_i$ with $i = \{1,2,3\}$. At any given time t the body occupies a region $\Omega(t)$, at an initial time $t_0 = 0$ the body occupies the initial (reference) region $\Omega_0(t_0)$, where the body is in its undeformed configuration. The position of a particle P set in the reference region Ω_0 at time t_0 is described by the position vector $\mathbf{X}(P,t_0)$. At a time $t > t_0$ the body $\mathcal{B}$ may have transformed from its reference configuration $\Omega_0(t_0)$ to its current configuration $\Omega(t)$, therefore, also changing the positions of its particles P_k. The deformation $\boldsymbol{\chi} : \Omega_0 \to \mathbb{R}^3$ transforms the position of a particle from the reference configuration $\mathbf{X}(P,t_0) \in \Omega_0$ to its new position in the current configuration $\mathbf{x}(P,t) = \boldsymbol{\chi}(\mathbf{X},t_0)$, yielding the deformation gradient

$$\mathbf{F}(\mathbf{X},t) = \frac{\partial \boldsymbol{\chi}(\mathbf{X},t)}{\partial \mathbf{X}} \tag{1.1}$$

used to describe motions of the body $\mathcal{B}$. To describe a potential change in volume of the body between configurations we use $J = \mathrm{d}v/\mathrm{d}V$, with $\mathrm{d}V$ and $\mathrm{d}v$ denoting infinitesimal volume elements in the reference and current configurations, respectively. The Jacobian determinant $J = \det \mathbf{F}(\mathbf{X},t) > 0$ (the determinant of the deformation gradient) can also be used to obtain volume changes.

To transform a vector $\mathbf{M}$ between configurations, the deformation gradient can be utilized according to $\mathbf{m} = \mathbf{F}\mathbf{M}$, with $\mathbf{M}$ denoting a vector with length $|\mathbf{M}| = 1$ in the reference configuration and $\mathbf{m}$ denoting the transformed vector in the current configuration. The (usual) change in vector length between $\mathbf{M}$ and $|\mathbf{m}|$ is given by the stretch ratio λ.

A polar decomposition of $\mathbf{F}$ shows that such a deformation includes rotating and stretching of a vector, and the deformation gradent can then be written as

$$\mathbf{F} = \mathbf{R}\mathbf{U} = \mathbf{v}\mathbf{R}, \tag{1.2}$$

with $\mathbf{R}$ denoting the rotation tensor and $\mathbf{U}$ and $\mathbf{v}$ denoting the right and left stretch tensors, respectively. The unique and orthogonal tensor $\mathbf{R}$ has the properties $\mathbf{R}^{\mathrm{T}}\mathbf{R} = \mathbf{I}$ ($\mathbf{I}$ denotes the second-order identity tensor) and $\det \mathbf{R} = 1$. Both unique and positive definite stretch tensors $\mathbf{U}$ and $\mathbf{v}$ are symmetric, the squares of the tensors are given by

$$\mathbf{C} = \mathbf{F}^{\mathrm{T}}\mathbf{F} = \mathbf{U}^2, \tag{1.3}$$

denoted as the right Cauchy-Green tensor and by

$$\mathbf{b} = \mathbf{F}\mathbf{F}^{\mathrm{T}} = \mathbf{v}^2, \tag{1.4}$$

the left Cauchy-Green tensor. Using the right Cauchy-Green tensor $\mathbf{C}$ yields the Green-Lagrange strain tensor

$$\mathbf{E} = \frac{1}{2}(\mathbf{C} - \mathbf{I}), \tag{1.5}$$

as a measure for the strain in the reference configuration Ω_0. Similarly we can describe the strain in the current configuration Ω through the Euler-Almansi strain-tensor given by

$$\mathbf{e} = \frac{1}{2}(\mathbf{I} - \mathbf{b}^{-1}), \tag{1.6}$$

in which the left Cauchy-Green tensor $\mathbf{b}$ is utilized.

Stress measures
Let us consider an infinitesimal spatial surface element $ds \in \Omega$ with its orientation defined by the outward normal (to the surface) unit vector $\mathbf{n}$. An infinitesimal force acting on the surface element may be denoted $d\mathbf{f}$, and the Cauchy traction vector $\mathbf{t}$ describing the (actual) force measured per unit surface area is then given by

$$d\mathbf{f} = \mathbf{t}ds. \tag{1.7}$$

Through Cauchy's stress theorem we can now relate the surface traction $\mathbf{t}$ with a the normal vector $\mathbf{n}$ by the unique symmetric second-order stress tensor field $\boldsymbol{\sigma}$ according to

$$\mathbf{t} = \boldsymbol{\sigma}\mathbf{n}. \tag{1.8}$$

Using Nanson's formular yields

$$\mathbf{P} = J\boldsymbol{\sigma}\mathbf{F}^{-\mathrm{T}}, \tag{1.9}$$

where $\mathbf{P}$ denotes the first Piola-Kirchhoff stress tensor (also know as the engineering stress tensor). Generally $\mathbf{P}$ is not symmetric, but it does fullfill the relation $\mathbf{P}\mathbf{F}^{\mathrm{T}} = \mathbf{F}^{\mathrm{T}}\mathbf{P}$. Another popular measure for stress is the symmetric second Piola-Kirchhoff stress tensor

$$\mathbf{S} = \mathbf{F}^{-1}\mathbf{P} = J\mathbf{F}^{-1}\boldsymbol{\sigma}\mathbf{F}^{-\mathrm{T}}, \tag{1.10}$$

obtained using the Piola transformation.

In addition to considerations regarding kinematics and stress, balance laws have been formulated which serve as basic axioms in continuums mechanics. The most important laws relevant for this work state that: (i) mass in a closed system has to be conserved and can, therefore, neither be created nor destroyed; (ii) changes in linear momentum of a region Ω have to be equal to external forces acting upon Ω; (iii) changes in angular momentum of a region Ω have to be equal to external moments acting upon Ω. For a more detailed mathematical discussion of all balance laws see [120].

1.4.2 Constitutive equations

If we consider hyperelastic materials (note, that the characteristic stress-strain response of arterial walls is considered to fall into this category), then we can describe the biomechanical response using a scalar-valued Helmholtz free-energy (strain-energy density) function $\Psi(\mathbf{F})$. The idea behind the usage of a strain-energy function for arterial walls is such, that the work required to deform the tissue is stored reversibly as deformation energy in the tissue and that only in a (stress-free, undeformed) reference configuration the stored energy becomes zero.

Before a strain-energy function can be utilized it has to fulfill several requirements. For one, the strain-energy must be positive for all deformations, i.e.

$$\Psi(\mathbf{F}) > 0 \qquad \text{for} \qquad \mathbf{F} \neq \mathbf{I}, \tag{1.11}$$

and zero for the special case of

$$\Psi(\mathbf{F} = \mathbf{I}) = 0, \tag{1.12}$$

where the deformation gradient is equal the identity tensor. This can be interpreted as no energy being stored in the undeformed material. Next, the strain-energy function must go towards $+\infty$ for infinite expansion or compression of a body, i.e.

$$\det \mathbf{F} \to +\infty \qquad \Rightarrow \qquad \Psi(\mathbf{F}) \to +\infty, \tag{1.13}$$

$$\det \mathbf{F} \to +0 \qquad \Rightarrow \qquad \Psi(\mathbf{F}) \to +\infty, \tag{1.14}$$

ensuring that the body volume can never vanish or infinitely expanded. Finally, material objectivity requires the following relations to be fulfilled:

$$\Psi(\mathbf{F}) = \Psi(\mathbf{U}) = \Psi(\mathbf{C}) = \Psi(\mathbf{E}). \tag{1.15}$$

With these requirements satisfied, we can now postulate a constitutive equation for a hyperelastic material according to, e.g.,

$$\mathbf{P} = \frac{\partial \Psi(\mathbf{F})}{\partial \mathbf{F}}, \tag{1.16}$$

describing the relation between the deformation of a material (given by **F**), and the stress in the material given by the first Piola-Kirchhoff stress tensor **P**. Considering requirement (1.15) on the strain-energy function, the constitutive stress relation can also be written in terms of the right Cauchy-Green tensor **C** or the Green-Lagrange strain tensor **E** according to

$$\mathbf{P} = 2\mathbf{F}\frac{\partial \Psi(\mathbf{C})}{\partial \mathbf{C}} \qquad \text{and} \qquad \mathbf{P} = \mathbf{F}\frac{\partial \Psi(\mathbf{E})}{\partial \mathbf{E}}. \tag{1.17}$$

1.4.3 Two fiber family structural model

To describe the mechanical behavior of the arterial wall we use a constitutive model in which the soft material is reinforced by two collagen fiber families. The strain-energy function is additively split into two parts according to

$$\Psi(\mathbf{C},\mathbf{M},\mathbf{M}') = \Psi_{\text{iso}}(\mathbf{C}) + \Psi_{\text{aniso}}(\mathbf{C},\mathbf{M},\mathbf{M}'), \tag{1.18}$$

where Ψ_{iso} and Ψ_{aniso} are associated with the non-collagenous ground-matrix and the embedded collagen fiber families, respectively, while $\mathbf{C}$ denotes the right Cauchy-Green tensor and both $\mathbf{M}$ and $\mathbf{M}'$ are direction vectors in the reference configuration corresponding to the principle directions of each collagen fiber familiy (note that $|\mathbf{M}| = |\mathbf{M}'| = 1$). For the isotropic contribution Ψ_{iso} it has been shown that the (classical) neo-Hookean model is a satisfactory descriptor of the ground-matrix [121], which can be written as

$$\Psi_{\text{iso}}(I_1) = \frac{c}{2}(I_1 - 3), \tag{1.19}$$

where $c > 0$ denotes a stress-like material parameter and $I_1 = \text{tr}(\mathbf{C})$ is the first invariant of the right Cauchy-Green tensor. For the anisotropic contribution Ψ_{aniso} caused by the progressive recruitment of collagen fibers we use an exponential function according to Holzapfel et al. [56], given by

$$\Psi_{\text{aniso}}(I_4,I_6) = \frac{k_1}{2k_2} \sum_{i=4,6} \left\{ \exp\left[k_2(I_i - 1)^2\right] - 1 \right\}, \tag{1.20}$$

with the stress-like material parameter $k_1 > 0$ and a dimensionless paramter $k_2 > 0$. The two invariants I_4 and I_6 are given by

$$I_4 = \mathbf{C} : \mathbf{A}_1 \qquad \text{and} \qquad I_6 = \mathbf{C} : \mathbf{A}_2, \tag{1.21}$$

where $\mathbf{A}_1$ and $\mathbf{A}_2$ are second-order structural tensors, determined by the tensor product of the preferred (or principal) orientations of both collagen fiber families, represented by $\mathbf{M}$ and $\mathbf{M}'$, i.e.

$$\mathbf{A}_1 = \mathbf{M} \otimes \mathbf{M} \qquad \text{and} \qquad \mathbf{A}_2 = \mathbf{M}' \otimes \mathbf{M}'. \tag{1.22}$$

To identify the individual components of the direction vectors $\mathbf{M}'$ and $\mathbf{M}$ we use a cylindrical polar coordinate system with the basis vectors $\mathbf{E}_R, \mathbf{E}_\Theta, \mathbf{E}_Z$ corresponding to the radial, circumferential and longitudinal directions of the arterial tube, respectively. The direction vectors then take on the form

$$[\mathbf{M}] = \begin{bmatrix} 0 \\ \cos\varphi \\ \sin\varphi \end{bmatrix} \qquad \text{and} \qquad [\mathbf{M}'] = \begin{bmatrix} 0 \\ -\sin\varphi \\ \cos\varphi \end{bmatrix}, \tag{1.23}$$

with φ denoting the angles between the principal directions of the two collagen fiber families, symmetrically arranged as two counter-rotating helices around the major vessel axes.

Finally, by combining equations (1.19) and (1.20) we can write the free-energy function $\Psi(I_1, I_4, I_6)$ in the form

$$\Psi = \frac{c}{2}(I_1 - 3) + \frac{k_1}{2k_2} \sum_{i=4,6} \left\{ \exp\left[k_2 (I_i - 1)^2\right] - 1 \right\}, \tag{1.24}$$

according to the constitutive model by Holzapfel et al. [56]. For modeling a young healthy human artery it is appropriate to treat the arterial wall as a two-layer thick-walled tube, because a young intima is mechanically not significant (its significance increases with age due to adaptive intimal thickening). In this case the strain-energy function according to equation (1.24) can be specified by using layer-specific material parameters c, k_1, k_2 and stuctural parameters φ for the media and adventitia.

1.4.4 Structural model including dispersion

Constitutive models using structural material parameters have been developed further to not only consider, e.g., principal directions of collagen fiber families, but to additionally include collagen fiber dispersion inherent to every layer of the arterial wall. A brief overview of the model is provided [122], including its shortcomings and resulting open issues for future dispersion models.

Based on the model by Holzapfel et al. (equation (1.20)), one additional scalar structure parameter κ is added as a measure for the collagen fiber dispersion. Thus

$$\Psi_{\text{aniso}}(I_1, I_4, I_6) = \frac{k_1}{2k_2} \sum_{i=4,6} \left\{ \exp\left[k_2 (I_i^* - 1)^2\right] - 1 \right\}, \tag{1.25}$$

with

$$I_i^* = \kappa I_1 + (1 - 3\kappa) I_i \qquad \text{with} \qquad i = 4, 6, \tag{1.26}$$

where k_1, k_2 and I_4, I_6 are the same parameters as in equation (1.20). The dispersion parameter ranges from $\kappa = 1/3$, corresponding to an isotropic fiber distribution, to $\kappa \to 0$, where it approaches the *Dirac* delta function (ideal fiber alignment). In its integral form κ can be written as

$$\kappa = \frac{1}{4} \int_0^{\pi} \rho(\Theta) \sin^3 \Theta \, \mathrm{d}\Theta, \tag{1.27}$$

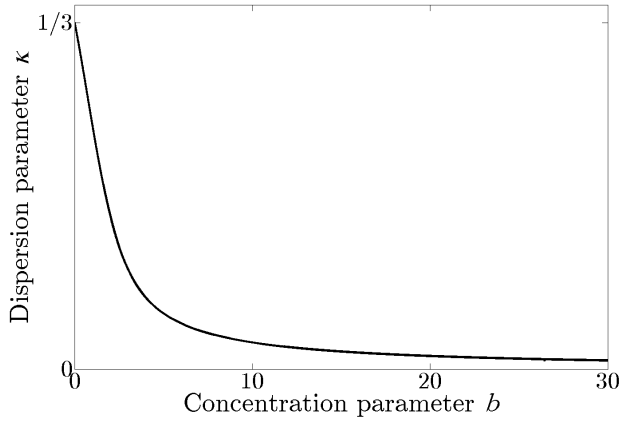

Figure 1.3: Behavior of the dispersion parameter κ as a function of the experimentally obtainable structural parameter b. At $b = 0$ the dispersion parameter $\kappa = 1/3$, corresponding to an isotropic fiber distribution; with $b \to \infty$, κ becomes the *Dirac* delta function representing ideal fiber alignment.

with $\rho(\Theta)$ denoting a density function representing the dispersed distribution of the collagen fibers in the reference configuration, and the Eulerian angle $\Theta \in [0, \pi]$. In this model $\rho(\Theta)$ was assumed to be a π-periodic *von Mises* distribution given by

$$\rho(\Theta) = 4\sqrt{\frac{b}{2\pi}}\frac{\exp[b(\cos(2\Theta)+1)]}{\operatorname{erfi}(\sqrt{2b})}, \tag{1.28}$$

with the concentration parameter b and imaginary error function

$$\operatorname{erfi}(x) = -\mathrm{i}\operatorname{erf}(\mathrm{i}x), \qquad \operatorname{erf}(x) = \frac{2}{\sqrt{\pi}}\int_0^x \exp(-t^2)\mathrm{d}t. \tag{1.29}$$

From equation (1.28) it becomes clear that the concentration parameter b determines the shape of the density function $\rho(\Theta)$ (and, therefore, also κ); for example, with higher b-values $\rho(\Theta)$ becomes increasingly narrower (more aligned). Figure 1.3 illustrations the influence of b on κ. Since b is a structurally-based scalar value it can be experimentally obtained by simply fitting a given angular fiber distribution (see subsequent sections).

One drawback of this model is the assumption of a rotationally symmetric density function to represent the dispersed collagen fibers. It has been well established (and will become evident during subsequent chapters of this work) that in a healthy artery the collagen fibers are almost completely aligned in-plane of the arterial wall. This in-plane arrangement is less pronounced in diseased arteries where increased out-of-plane deviations are observed, but even then the distribution of collagen fibers is far from being rotationally symmetric.

Therefore, even though the above discussed dispersion model, based on a density function according to equation (1.28), is the best option available at the time, it is not a good representation of true fiber morphologies and leaves room for improvement. There exists an experimentally motivated need for the development of a structurally-based dispersion model, capable of reflecting dispersed collagen fiber orientations obtained through experimental investigations.

1.5 Organization of the PhD Thesis

The PhD thesis is a compilation of four scientific papers, focusing on the structural organization and role of fibrillar collagen in human arterial walls. During the course of this thesis, several new experimental and numerical tools for the quantification of collagen fiber distributions have been developed: experimental advancements of existing laboratory protocols, development and building of novel sample preparation equipment, implementation of new tissue clearing procedures, and programming of Matlab code for extracting, fitting, and characterizing collagen fiber morphologies from 2D images as well as 3D image stacks. During a four month research assignment at Yale University, USA, new insights into the role of collagen remodeling in dissecting aortic aneurysms were discovered. All of these advancements have been published in the following four journal papers:

1. *Determination of the Layer-specific Distributed Collagen Fibre Orientations in Human Thoracic and Abdominal Aortas and Common Iliac Arteries*
   A.J. Schriefl, G. Zeindlinger, D.M. Pierce, P. Regitnig and G.A. Holzapfel, Journal of the Royal Society Interface, 9:1275–1286, 2012.

   In this study we used a well established experimental approach to obtain collagen fiber angles from histological sections through polarized light microscopy in combination with a universal stage. We recorded over $37,000$ fiber angles from 11 human non-atherosclerotic thoracic and abdominal aortas and common iliac arteries. Special attention was given to the sample preparation method by applying planar axial and circumferential pre-stretches before tissue fixation. The study yielded mean data for each of the three individual layers of the arterial wall, which was quantified using a dispersion model. Distinct fiber families were observed in all vessels, usually two in the medias and adventitias and sometimes a third or fourth in the intimas. The fiber families were generally arranged symmetrically with respect to the cylinder axes, and closer to the circumferential direction in the media and to the axial direction in the adventitia. However, in the media of the common iliac artery only one fiber family in the circumferential direction was observed. Besides collagen fiber angles we additionally recorded layer-specific thickness data for each vessel. For the aortas and the common iliac artery the mean total wall thickness was 1.39 and 1.05 mm, respectively.

2. *Remodeling of Intramural Thrombus and Collagen in an Ang-II Infusion ApoE-/- Model of Dissecting Aortic Aneurysms*
   A.J. Schriefl, M.J. Collins, D.M. Pierce, G.A. Holzapfel and J.D. Humphrey, Thrombosis Research, 130:e139–e146, 2012.

   The study focuses on the role of collagen and intramural thrombus remodeling in dissecting aortic aneurysms. The investigated histological cross-sections were obtained from five lesions from angiotensin-II (Ang-II) infused, apolipoprotein-E null (ApoE$-/-$) mice, a commonly used animal model to generate dissecting aortic aneurysms. The mostly histological investigations resulted in new observations related to collagen remodeling. In both, the adventitia as well as the intramural thrombus, remarkable remodeling was observed in regions well separated from the flowing blood. Thrombotic material was replaced by collagenous tissue, constituting a favorable wound healing type response. Such gained insight could potentially have a broader impact, e.g., in the use of endografts to treat aortic aneurysms or for flow-diverting stents used to treat intracranial aneurysms. Finally, regardless of the specific mechanisms responsible for the pathogenesis, we suggested a possible scenario explaining the initiation and progression of the lesion, resulting in a dissecting aortic aneurysm in the Ang-II mouse model after only 28 days of treatment with Ang-II.

3. *Quantitative Assessment of Collagen Fiber Orientations from 2D Images of Soft Biological Tissues*
   A.J. Schriefl, A.J. Reinisch, S. Sankaran, D.M. Pierce and G.A. Holzapfel, Journal of the Royal Society Interface, 9:3081–3093, 2012.

   In this study a new method was developed for the quantification of collagen fiber orientations and associated dispersions at different length-scales, which can be utilized in numerical modeling of soft biological tissues. Instead of measuring individual collagen fiber angles by hand from stained histological sections using polarized light and a universal stage (as it was done traditionally), we focused on extracting the fiber angles fully automated from 2D images using various image analysis techniques. Specifically our new method combines 2D Fast Fourier Transformation, Fourier power spectrum analysis and wedge filtering to extract relative amplitude distributions representing the fiber orientations in the original image. Furthermore, we showed how progressive regions of interest splitting can be utilized to obtain useful orientation information among different length-scales. The amplitude distributions were fitted using maximum likelihood estimation and a π-periodic von Mises distribution (either one or a mixture of two von Mises distributions in the case of one or two fiber families, respectively). Regarding material parameters for numerical modeling we focused on three key parameters: first, the dispersion parameter κ, a well established measure of anisotropy; second, the location parameter μ, describing the preferred (or principal) direction of a fiber family; third, the weighted

error entropy E_w, as a measure of changes in the entire fiber distributions at different length-scales (which also has implications for numerical modeling, e.g., on determining appropriate mesh densities).

4. *An Automated Approach for 3D Quantification of Fibrillar Structures in Optically Cleared Soft Biological Tissues*
   A.J. Schriefl, H. Wolinski, P. Regitnig, S.D. Kohlwein and G.A. Holzapfel

   In this study we introduce a new approach for imaging and analyzing the entire thickness of the intact human aortic wall. To this end we developed a novel sample preparation method, allowing us to chemically fixate (using formalin) an intact segment of the aortic tube as a whole, that has been axially pre-stretched and simultaneously pressurized based on *in vivo* values. To enhance the laser penetration range for subsequent nonlinear optical imaging, the fixed vessel segment was optically cleared using a solution of benzyl alcohol to benzyl benzoate, increasing the penetration depth almost tenfold from $\sim 120\,\mu$m to $\sim 1.2\,$mm. Image stacks throughout the thickness of the cleared wall were made by detecting the second-harmonic generation signal originating from the collagen fibers. To extract and quantify the 3D morphological data from image stacks in a simple, fast and automated fashion we combined Fourier-based image analysis for characterizing collagen organization with maximum likelihood estimation for distribution fitting of 3D-orientational data sets. For the first time we were able to visualize collagen structures throughout the thickness of the aortic wall and extract the corresponding 3D distribution of amplitudes (1° resolution) representing the orientations of the collagen fibers. Furthermore we identified isotropic regions in the tissue where no preferred fiber orientations are observed and quantified regions of anisotropy by calculating two structural parameters: (i) μ, describing the principal fiber orientation and (ii) b, describing the degree of fiber alignment about μ. Both, μ and b, can directly be utilized in numerical modeling codes using fiber-reinforced constitutive laws.

Additionally, the following conference proceedings and accepted (extended) abstracts were part of the thesis:

- A.J Schriefl, D.M. Pierce, P. Regitnig and G.A. Holzapfel: *Experimental determination of the distributed collagen fiber orientations in the human descending aorta and common iliac artery.* 82nd Annual Meeting of the International Association of Applied Mathematics and Mechanics (GAMM), Graz, Austria, April 18–22, 2011.

- G. Zeindlinger, A.J. Schriefl, P. Regitnig, D.M. Pierce and G.A. Holzapfel: *A sample preparation method for the measurement of distributed collagen fiber orientations in human soft tissues.* 82nd Annual Meeting of the International Association of Applied Mathematics and Mechanics (GAMM), Graz, Austria, April 18–22, 2011.

- D.M Pierce, H. Weisbecker, A.J. Schriefl, B.R. Villa, E.J. Gómez Aguilera and G.A. Holzapfel: *Modeling aortic tissue and intraluminal thrombus: experimental and numerical results.* 2nd International Conference on Material Modelling and 12th European Mechanics of Materials Conference, Paris, France, August 31–September 2, 2011.
- A.J. Schriefl, G. Zeindlinger, D.M. Pierce and G.A. Holzapfel: *Experimental quantification of the layer-specific distribution of collagen fiber orientations in human descending aorta and common iliac arteries.* Joint Workshop on New Technologies for Computer/Robot Assisted Surgery, Graz, Austria, July 11–13, 2011.
- G.A. Holzapfel, A.J. Schriefl, A.J. Reinisch, D.M. Pierce, S. Murtada, M. Böl and J. Stålhand: *Advances in the modeling of soft collagenous tissues: the role of distributed collagen fiber orientations and active tone in arteries.* IUTAM-Symposium on Computer Models in Biomechanics: from Nano to Macro, Stanford, USA, August 29–September 2, 2011.
- A.J. Schriefl, P. Regitnig, D.M. Pierce and G.A. Holzapfel: *Layer-specific distributed collagen fiber orientations in human arteries, from thoracic aorta to common iliac artery.* ASME 2011 Summer Bioengineering Conference, Farmington, USA, June 22–25, 2011.
- G. Sommer, G. Zeindlinger, A. Katzensteiner, A.J. Schriefl, H. Ainödhofer, A. Saxena and G.A. Holzapfel: *Passive mechanical response and residual deformations of ovine esophagus: impact on esophagus tissue engineering.* 8^{th} European Solid Mechanics Conference, Graz, Austria, July 9–13, 2012.
- A.J. Reinisch, A.J. Schriefl and G.A. Holzapfel: *Modeling of dispersed fibers in continua.* 8^{th} European Solid Mechanics Conference, Graz, Austria, July 9–13, 2012.
- A.J. Schriefl, G.A. Holzapfel and J.D. Humphrey: *Roles of thrombus and collagen remodeling in intramural dissecting aortic aneurysms.* 8^{th} European Solid Mechanics Conference, Graz, Austria, July 9–13, 2012.

2 LAYER-SPECIFIC COLLAGEN FIBER ORIENTATIONS IN HUMAN ARTERIES

Abstract. The established method of polarized microscopy in combination with a universal stage is used to determine the layer-specific distributed collagen fiber orientations in 11 human non-atherosclerotic thoracic and abdominal aortas and common iliac arteries (63.0 ± 15.3 yr, mean $\pm$ SD). A dispersion model is used to quantify over $37,000$ recorded fiber angles from tissue samples. The study resulted in distinct fiber families, fiber directions, dispersion and thickness data for each layer and all vessels investigated. Two fiber families were present for the intima, media and adventitia in the aortas, with often a third and sometimes a fourth family in the intima in the respective axial and circumferential directions. In all aortas, the two families were almost symmetrically arranged with respect to the cylinder axis, closer to the axial direction in the adventitia, closer to the circumferential direction in the media and in between in the intima. The same trend was found for the intima and adventitia of the common iliac arteries; however, there was only one preferred fiber alignment present in the media. In all locations and layers the observed fiber orientations were always in the tangential plane of the walls, with no radial components and very small dispersion through the wall thickness. A wider range of in-plane fiber orientations was present in the intima than in the media and adventitia. The mean total wall thickness for the aortas and the common iliac artery was 1.39 and 1.05 mm, respectively. For the aortas a slight thickening of the intima and a thinning of the media in increasingly distal regions was observed. A clear intimal thickening was present distal to the branching of the celiac arteries. All data, except for the media of the common iliac arteries, showed two prominent collagen fiber families for all layers so that two-fiber family models seem most appropriate.

2.1 Introduction

Alterations of the underlying mechanical principles of the healthy arterial wall (for example, changes in the wall constituents) are believed to have implications upon arterial disease and degeneration [123]. Available evidence suggests: intimal thickening is due to specific mechanical stresses [57], atherosclerosis may be related to increased arterial wall stiffness [69], aortic disease may be linked to differences in the tissue organization and content in the proximal and distal regions of the aorta [124], and enlargement of intracranial aneurysms may result from growth and rearrangement of collagen due to stress (increasing the risk of rupture with a related mortality rate of 35–50%) [125]. Aging processes such

as stiffening of the vessel wall [77, 126, 127] are related to an increase of collagen content relative to elastin [128, 129], fibrosis and continuous depositions of amorphous substances for the elastin, and increased cross-linking of collagen, all of which lead to reduced mobility of the arterial wall constituents [130]. Additionally, for the human abdominal aorta, sex-dependent differences in the degrees of stiffening have been reported [77], and generally the interaction of the structural vessel wall components with the different constituents of the extracellular matrix is believed to be a key factor in understanding diseases; see, for example, [130].

The (passive) mechanical behavior of arterial walls is mainly determined by elastin and collagen in the media and adventitia [131]. These two constituents are embedded in an extracellular, non-fibrous, glycosaminoglycan-rich matrix [129], forming a complex three-dimensional (3D) network including smooth muscle cells [132]. The structural subdivision of the collagen fiber into fibrils and micro-fibrils significantly increases its flexibility (which is directly proportional to the number of subunits) and reduces the risk of rupture because cracks cannot easily propagate across a multiple fibrils [22, 25, 133]. With an ultimate tensile strength in the range of 50–100 MPa [26], it is the collagen fibers that give the arterial wall its strength and ability to resist loads. Thus, with regard to strength and load resistance, collagen fibers are mechanically the most important tissue constituents [22, 56, 134]. Together with proteoglycans, it is the elastin with its nearly perfect elastic properties which is responsible for the resilience of the matrix [135]. Elastin is load-bearing at low and high strains, with a less significant contribution at higher strains due to the increased bearing of load through collagen.

In humans there are 28 known different types of collagen; however, the collagen fibers investigated in this study are limited to the major types present in arterial walls, namely the classical fibrillar collagen of types *I* and *III* [4]. Collagen types *IV*, *V*, and *VI* are also present in human arteries (among others), but these constitute only about 0.5–1.0% of the total arterial collagen. While the significance of collagen fiber orientation and dispersion on the mechanical properties of arterial walls has been well-established (see, for example, [56, 122, 136]), and data of collagen organization in 2D and 3D for human vessels have been published, see, for example, [125, 137–140], limited structural data are available to date regarding collagen orientation in the human aorta and common iliac artery. In young and healthy arteries, the intima consists of a single layer of endothelial cells with no structural importance to the wall. It becomes mechanically significant with aging and the associated onset of arteriosclerosis [58]. In the media, the collagen fiber arrangement in human cerebral arteries is circumferential [141]. For the adventitia of human coronary arteries (fixed at distending pressure), a single circumferential order of collagen has been reported in [137], while for cerebral arteries a wide range of orientations are present [139].

It is known that variations exist in both the structural composition and the mechanical properties of arteries from different species, as well as in different regions of the same arteries,

and that they both influence the mechanical response of the vessels [74–76]. Differences were observed in intimal and internal muscular layers between different ethnic groups [57], and are also expected (in all likelihood) among different age groups of a single species [77, 78]. In the human aorta the elastin-to-collagen ratio decreases in progressively distal regions making the aorta most flexible at proximal regions [69]. Such differences in morphology among arteries may change the influence of pressure and wall shear stresses upon the vessels [142, 143]. Hence, experimental data on the collagen arrangement from human tissue samples of specific blood vessels are indispensable to facilitate better understanding of disease progression and improve modeling of the cardiovascular system.

The approach taken in this study differs from related research on cerebral arteries [136, 138] and intracranial aneurysms [125, 140], where investigations into the collagen fiber orientations were performed. We use the well-established method of picrosirius-polarization [38, 144], in combination with a universal stage, similar to the method pioneered and described in [145], to study samples from healthy, non-atherosclerotic, human aortas and common iliac arteries for the first time. The birefringent feature of the collagen fibers is utilized for the measurement of the collagen fiber orientations. Picrosirius red was used as a birefringence enhancement stain for collagen [38]. Qualitative and quantitative data with respect to the fiber alignments were obtained using polarized light microscopy [36]. To approximate the *in vivo* strain state of the blood vessel, all of the samples investigated were pre-stretched biaxially with a specially designed fixture, followed by chemical fixation in formalin while distended [57]. This process resulted in improved fiber orientation coherence [63, 74, 139]. The measurements were performed using a Zeiss universal stage attached to a Zeiss polarizing microscope (Carl Zeiss IMT GmbH, Vienna, Austria) [140], enabling the measurement of two Euler angles and thus fully defining the local orientation of the mostly straightened fibers in the 3D space. The measured data were fitted with the *von Mises* distribution allowing the determination of the orientation density function characterizing the 3D distribution of collagen fiber orientations in the (unloaded) reference configuration [122].

The quantitative structural information obtained through this study will not only improve our understanding of the biomechanical behavior of arterial walls, but will also have a broader impact on the modeling of the cardiovascular system, providing fundamental parameters for mathematical models which are becoming more widely used, and will even become more important in clinical decision making.

2.2 Methods and Materials

2.2.1 Tissue preparation

Eleven human non-atherosclerotic, descending aortas including the common iliac arteries (all are elastic-type vessel walls) were harvested within 24 hours from death (63.0 ± 15.3 yr, mean $\pm$ SD, 6 women ranging from 48 to 91 and 5 men ranging from 43 to 83). Precaution was taken not to include samples showing type *IV* lesions or higher, or other pathologies [146]. For the present study, the use of autopsy material from human subjects was approved by the Ethics Committee of Medical University Graz.

Seven square samples were removed from each axially cut vessel at specific locations labeled as T1, T2, T3, A1, A2, A3, and CI (see Fig. 2.1). The labeling T and A refer to the descending thoracic region T1–T3 and the abdominal region A1–A3 of the aorta, respectively, while CI refers to the common iliac artery. Anatomic landmarks like the branching of the celiac arteries were used to ensure consistent, repeatable sample locations. Samples from different vessels were always taken from the same seven locations and measured 15×15 mm. Two corners of each sample were removed to mark the circumferential direction of the vessel. Four black markers were placed at the center of each sample, separated by a distance of approximately 6.0 mm in each coordinate direction, for tracking with the video extensometer. A coordinate system was applied to this reference geometry, where X is the circumferential direction, Y the axial direction, and Z indicates the direction of the sample thickness. This geometry is referred to as the unloaded configuration, while in the deformed configuration the axes are labeled with lower case characters (x,y,z) to unambiguously distinguish between them.

To approximate the *in vivo* stress/strain state of the vessel wall and to ensure (mostly) straightened collagen fibers, a biaxial stretch was applied with a specially-designed fixture. The consideration of a biaxial pre-stretch is an important part of the sample preparation method because a pre-stretch has a substantial influence on the organization of the layered microscopic structure of collagen and muscle fibers [147]. To minimize boundary effects during the sample stretching, a suture-based gripping method was chosen with three hooks, serving as suture attachments for each edge of the sample. The three hooks spanned about 10 mm, and the area between the four markers was approximately 6×6 mm in the (planar un-stretched and unloaded) reference configuration.

Before stretching the sample, the distance between the markers in the X- and Y-directions, and the sample thickness (the Z-direction), were measured using a video extensometer, yielding the geometries of the unloaded configurations of the specimens. Using a displacement-controlled protocol, a strain of 22% in the circumferential direction and 12% in the axial direction was then applied with a custom made fixture. Our value for the axial strain is based on the lower bound of *in vivo* values reported in [148], and for the circumferential strain we used a similar value as described in [149]. Figure 2.2 shows a tissue

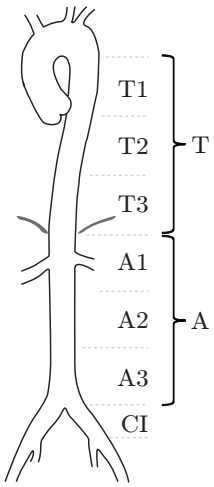

Figure 2.1: Seven locations T1, T2, T3, A1, A2, A3 and CI along the aortas and the common iliac arteries from which samples were extracted. T and A denote the descending thoracic and abdominal part of the aorta, and CI the common iliac arteries.

sample mounted in the fixture before stretching it biaxially. Applying a controlled stretch was essential during tissue preparation since it not only approximates the *in vivo* conditions of the vessel wall but also straightens the collagen fibers resulting in an increasingly coherent orientation necessary to perform accurate angular measurements [63, 139, 150]. The stretched sample and fixture were then put into a bath of 4% formaldehyde for chemical fixation. After approximately 10 hours in the formaldehyde bath, the sample was removed from the stretching fixture and sewn into a specially-designed aluminum frame to maintain the stretched state while the sample was dehydrated, and embedded in paraffin wax. At the beginning of the embedding process the specimen was dipped into the first hot paraffin bath while still mounted in the fixture to counteract shrinking due to the rapid temperature change of about 40°C. The sample was then removed from the aluminum frame for further processing.

The resulting paraffin block (with the embedded tissue sample) was cut into two halves, one was used to obtain in-plane sections (*x*-*y* plane) and the other to obtain transverse sections (*x*-*z* plane). A series of planar sections was made according to the following protocol: (i) begin sectioning from the luminal side (intima is sectioned first), (ii) make six subsequent sections at $8\,\mu$m, (iii) leave a gap of $100\,\mu$m before starting with the next series of six sections. This was repeated throughout the entire embedded sample as many times as possible. The preferred section thickness of $8\,\mu$m was determined in a pilot study on pig aortas during which we tested section thicknesses ranging from 2-12 μm (in $2\,\mu$m steps). We found that histological sections with a thickness below $7\,\mu$m were sometimes very fragile and often contained cracks and/or tears, while sections with a thickness above $8\,\mu$m often displayed a 3D topography which made it difficult to focus or achieve proper extinctions.

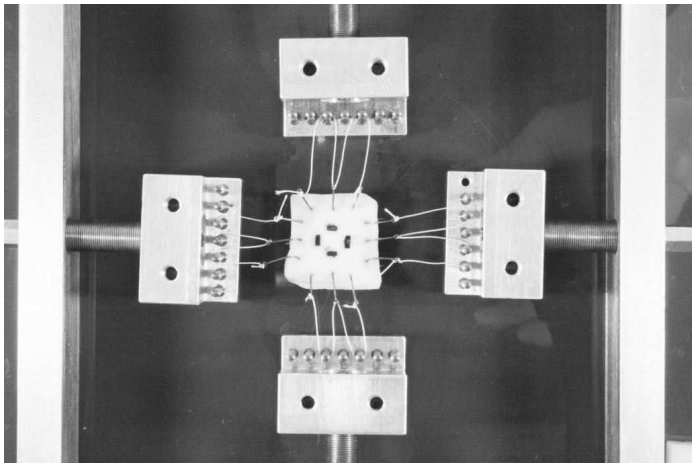

Figure 2.2: Tissue sample mounted in the test fixture under biaxial stretch to approximate the *in vivo* strain state prior to chemical fixation in 4% formaldehyde while distended. Four black markers at the center of the sample are used for measuring the biaxial stretch via a video extensometer.

Every first section out of each series of six was then stained with picrosirius red, a well known birefringent enhancement stain for collagen that does not change the optical axis of the unstained fibers [38]. Every second section was stained with hematoxylin and eosin for standard histological analysis to detect atherosclerotic lesions of type *IV* or higher according to [146], to determine if the sample could be included in this study. All sections were cut with a *Microm HM 335* (Microm, Walldorf/Baden, Germany).

To ensure that the sample preparation process caused no geometrical changes (for example, a shrinking of the wall during the fixing in paraffin), we measured the wall thicknesses of the stretched samples before paraffination and compared these with the thicknesses obtained from the microscopic images. In all cases the same results were obtained within the tolerance of the measurement procedures.

2.2.2 Method of measurement

A Zeiss three-axis universal rotary stage attached to the main stage of a Zeiss polarizing microscope was used for the determination of the 3D distribution of collagen fiber orientations. Each microscope slide with the histological section was fixed between two glass hemispheres, thus ensuring that the polarized light always enters the glass perpendicularly and minimizing light reflections in tilted positions. The hemispheres have an index of refraction of 1.516; additionally, to minimize internal reflections and refractions the inner surfaces were coated with Glycerol (index of refraction ~ 1.47). The area of interest on the tissue section was centered between the two glass hemispheres to avoid distortions that occured on the outer rim.

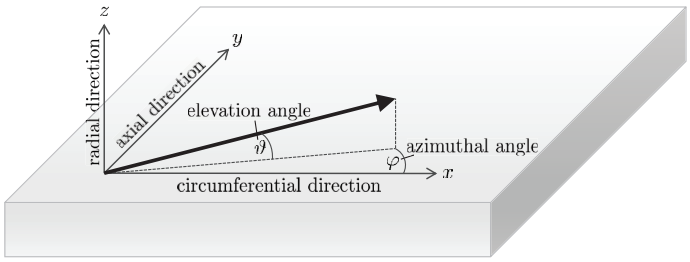

Figure 2.3: Definition of the coordinate system and two Euler angles φ and ϑ on a biaxially-stretched tissue sample.

The universal stage allowed the tissue sections to be tilted and rotated in angled planes around its three axes. All rotational angles can be measured. For an unambiguous definition of the orientation of a line (idealized straightened collagen fiber) in 3D, two Euler angles may be used. In our coordinate system the azimuthal angle φ denotes the in-plane rotations (circumferential-axial plane) of the sample where $\varphi = 0^\circ$ is then the circumferential direction. The elevation angle ϑ denotes the out-of-plane rotations (circumferential-radial plane) with $\vartheta = 0^\circ$ denoting no radial component in the orientation of the fiber, see Fig. 2.3.

To measure the collagen fiber directions, the polarizer and the analyzer were preset at extinction so that only the birefringent components of the tissue were visible. It has long been established that type *I* and type *III* collagen, the major types in arterial walls [151], exhibit a positive intrinsic and form birefringence [36]. In order to determine the best sample location for the angular measurements (for example, to avoid regions which were damaged during the tissue preparation process), the entire tissue section was first scanned with a relatively low magnification ($2.5\times$ objective lens). The region of interest was then centered and aligned to the in-plane ($\vartheta = 0^\circ$) and circumferential ($\varphi = 0^\circ$) direction. A $10\times$ objective lens was then used for all measurements. The slide was rotated in the azimuthal plane until the collagen fibers reached its darkest position yielding the first Euler angle φ, followed by tilting the slide in the elevation plane without further changing the azimuthal angle until the final darkest position was found, yielding the second Euler angle ϑ. Images were also taken of transversally cut tissue samples with the polarizing microscope, also allowing the elevation angle ϑ to be measured directly from the images using standard software (Axiovision 40, Carl Zeiss IMT GmbH, Vienna, Austria). To determine the layer-specific thicknesses of the arterial walls, images were taken from each transversely cut tissue sample from all vessels. Using Axiovision 40, approximately 20 thickness measurements for each of the intima, media and adventitia were performed from each image. The average thicknesses for each of the three layers were obtained by calculating the mean value and the standard deviation of the 20 measurements. To obtain the total wall thickness the three mean values were added, the total standard deviation was calculated by using $SD_{\text{tot}} = \sqrt{\sum_{i=1}^{3} n_i^2}$, where n is the standard deviation of each layer.

2.2.3 Data analysis

The collagen fiber directions φ, ϑ were measured in the deformed configuration to mimic the *in vivo* stress/strain condition and to ensure (mostly) fiber straightening. In the unstressed state the fibers generally exhibit wavy patterns, often without a clear spatial direction which is difficult to measure. However, material models consider the fiber directions in the reference configuration [56, 122]. To ensure unambiguous differentiation between the two configurations, all axes, vectors and angles are now denoted with lower case characters for the deformed configuration and with upper case characters for the reference configuration.

In the following we briefly introduce the required nonlinear kinematics. By Ω_0 we denote the reference configuration of a sample, while the deformation $\chi : \Omega_0 \to \mathbb{R}^3$ transforms a material point $\mathbf{X} \in \Omega_0$ to a new position $\mathbf{x} = \chi(\mathbf{X}) \in \Omega$ in the deformed configuration [120]. As a deformation we introduce the deformation gradient as $\mathbf{F}(\mathbf{X}) = \partial\chi(\mathbf{X})/\partial\mathbf{X}$. We consider the artery wall to be incompressible, which yields the condition $\lambda_x\lambda_y\lambda_z = 1$ for the three stretch ratios λ_x, λ_y and λ_z. Hence, for the biaxial pre-stretch in the x-, y-plane, when stretched along the fibers, the deformation gradient $\mathbf{F}$ in matrix notation takes on the form

$$[\mathbf{F}] = \mathrm{diag}[\lambda_x,\ \lambda_y,\ (\lambda_x\lambda_y)^{-1}]. \tag{2.1}$$

It is worth remarking here that it is important to minimize shear during biaxial stretching because of the inability to impose and control shear stresses. Shearing strains are usually much smaller than the extensional strains [152]; we therefore treated the shearing strains as negligible. For more details on this issue see [153].

All measured azimuthal and elevation angles from the deformed tissue samples are now described as a unit vector with the Cartesian components $x = \cos\vartheta\cos\varphi$, $y = \cos\vartheta\sin\varphi$ and $z = \sin\vartheta$, yielding a spatial fiber vector field corresponding to the measured fiber directions themselves in the deformed state. In the following we simply use the inverse deformation gradient $\mathbf{F}^{-1}$ for mapping back the vector field from the deformed to the reference configuration. Due to this pull-back operation, the corresponding X-, Y- and Z-coordinates in the reference configuration (assuming homogeneous deformation) result as

$$[X\ Y\ Z]^{\mathrm{T}} = [\mathbf{F}^{-1}][x\,y\,z]^{\mathrm{T}}. \tag{2.2}$$

To obtain the elevation angle Θ and the azimuthal angle Φ in the reference configuration the following relations are used (see also [150])

$$\Theta = \arctan\left(\frac{Z}{\sqrt{X^2+Y^2}}\right), \qquad \Phi = \arctan\left(\frac{Y}{X}\right). \tag{2.3}$$

All angle data in the reference configuration from all vessels were then averaged, resulted in mean values for the intima, media, and adventitia for the locations T1 to CI. The angles

were plotted with a 5° resolution, generating the fiber density, say ρ_{m}, of the measured data (indicated by the index m) as a function of Θ and Φ.

Since we ultimately desire to use the measured data in an existing constitutive model [122], we need to transform the Euler angles Θ and Φ from our coordinate system (see Fig. 2.3) to the coordinate system used in [122]. We denote the transformed angles by $\widetilde{\Theta}$ and $\widetilde{\Phi}$. Thus,

$$\widetilde{\Phi} = \arctan\left(\tan\Theta\frac{1}{\sin\Phi}\right), \qquad \widetilde{\Theta} = \arctan\left(\frac{\tan\Phi}{\cos\widetilde{\Phi}}\right). \tag{2.4}$$

In the new Cartesian coordinate system, the distributed collagen fiber orientations in Ω_0 are characterized by a density function $\rho(\mathbf{M}(\widetilde{\Theta},\widetilde{\Phi}))$ with respect to the undeformed orientation of an arbitrary unit vector $\mathbf{M}$. With $(\widetilde{\mathbf{e}}_1,\widetilde{\mathbf{e}}_2,\widetilde{\mathbf{e}}_3)$, an orthonormal Cartesian basis, and with the two Euler angles $\widetilde{\Theta}\in[0,\pi]$ and $\widetilde{\Phi}\in[0,2\pi]$, the unit vector $\mathbf{M}$ takes on the form

$$\mathbf{M}(\widetilde{\Theta},\widetilde{\Phi}) = \sin\widetilde{\Theta}\cos\widetilde{\Phi}\widetilde{\mathbf{e}}_1 + \sin\widetilde{\Theta}\sin\widetilde{\Phi}\widetilde{\mathbf{e}}_2 + \cos\widetilde{\Theta}\widetilde{\mathbf{e}}_3. \tag{2.5}$$

For simplicity, the distribution of the experimentally measured collagen fiber family is assumed to have rotational symmetry about a principal direction $\mathbf{a}_0$, consistent with [122]. Representation of a single collagen fiber family, which does not include dispersion, can be accomplished using a structure tensor of the form $\mathbf{a}_0\otimes\mathbf{a}_0$ [56]. By fiber family we mean a group of fibers oriented along a single common direction of alignment with some dispersion.

Without loss of generality, the preferred direction of the unit vector $\mathbf{a}_0$ is now taken to have the same direction as the basis vector $\widetilde{\mathbf{e}}_3$ making the density function $\rho(\mathbf{M}(\widetilde{\Theta},\widetilde{\Phi}))$ independent of $\widetilde{\Phi}$, i.e. $\rho(\mathbf{M}(\widetilde{\Theta},\widetilde{\Phi}))\to\rho(\widetilde{\Theta})$. This allows the *generalized* structure tensor, which is an alternative measure of the fiber distribution in a continuum sense, to be written in the compact form [122]

$$\mathbf{H} = \kappa\mathbf{I} + (1-3\kappa)\,\mathbf{a}_0\otimes\mathbf{a}_0, \tag{2.6}$$

with the identity tensor $\mathbf{I}$ and the dispersion (or structure) parameter κ, given by

$$\kappa = \frac{1}{4}\int_0^\pi \rho(\widetilde{\Theta})\sin^3\widetilde{\Theta}\,\mathrm{d}\widetilde{\Theta}. \tag{2.7}$$

To model the rotational symmetry about a preferred fiber direction $\mathbf{a}_0$, a transversely isotropic and π-periodic *von Mises* distribution is used according to [122], with the density function $\rho(\widetilde{\Theta})$ as

$$\rho(\widetilde{\Theta}) = 4\sqrt{\frac{b}{2\pi}}\frac{\exp[b(\cos 2\widetilde{\Theta}+1)]}{\mathrm{erfi}(\sqrt{2b})}, \tag{2.8}$$

where $b>0$ is the so-called concentration parameter associated with the *von Mises* distribution, and $\mathrm{erfi}(x) = -\mathrm{i}\,\mathrm{erf}(\mathrm{i}x)$ denotes the imaginary error function [154]. From (2.7)

it is clear that the dispersion parameter κ describes the *degree of dispersion* in an integral sense, ranging from $\kappa = 1/3$ ($b = 0$), describing an isotropic distribution of fibers in a continuum sense, to $\kappa = 0$ ($b \to \infty$), describing perfect alignment of the collagen fibers. In the latter case the density function $\rho(\widetilde{\Theta})$ in (2.8) becomes the *Dirac* delta function.

The method of least squares was applied to determine the best fit for the fiber density $\rho_{\mathrm{m}}(\widetilde{\Theta},\widetilde{\Phi})$, by using the π-periodic *von Mises* distribution as a function of the concentration parameter b, the elevation angle $\widetilde{\Theta}$ and the azimuthal angle $\widetilde{\Phi}$. To facilitate fitting, the volumes enclosed by ρ_{m} and the *von Mises* distribution ρ were both normalized to 4π. The optimized value of the least squares fit was then obtained by minimizing the residual sum of squares given by

$$RSS = \sum_{i=1}^{n} [\rho_{\mathrm{m}}(\widetilde{\Theta},\widetilde{\Phi})_i - \rho(b,(\widetilde{\Theta},\widetilde{\Phi})_i)]^2, \tag{2.9}$$

where n denotes the number of observed angle pairs $(\widetilde{\Theta},\widetilde{\Phi})_i$, binned on a $5 \times 5^\circ$ grid, ranging from -90° to $+90^\circ$, and *RSS* denotes the squared distance between the (measured) fiber density $\rho_{\mathrm{m}}(\widetilde{\Theta},\widetilde{\Phi})_i$ of every angle and the corresponding density $\rho(b,(\widetilde{\Theta},\widetilde{\Phi})_i)$ of the *von Mises* distribution. Although the *von Mises* distribution is independent of $\widetilde{\Phi}$, we used it to obtain the values for $\rho(b,(\widetilde{\Theta},\widetilde{\Phi})_i)$ in (2.9). As a measure of the goodness-of-fit we calculated the coefficient of determination R^2 as

$$R^2 = 1 - \frac{RSS}{TSS} = 1 - \frac{\sum_{i=1}^{n} [\rho_{\mathrm{m}}(\widetilde{\Theta},\widetilde{\Phi})_i - \rho(b,(\widetilde{\Theta},\widetilde{\Phi})_i)]^2}{\sum_{i=1}^{n} [\rho_{\mathrm{m}}(\widetilde{\Theta},\widetilde{\Phi})_i - \overline{\rho_{\mathrm{m}}}(\widetilde{\Theta},\widetilde{\Phi})]^2}, \tag{2.10}$$

where $\overline{\rho_{\mathrm{m}}}(\widetilde{\Theta},\widetilde{\Phi})$ denotes the overall mean of the measured fiber density ρ_{m} for all angle pairs $(\widetilde{\Theta},\widetilde{\Phi})_i$ and TSS is the sum of the squared distances between every individual density value of the measured angle pairs and the overall mean fiber density. Hence, R^2 yields values between 0 and 1; the better the *von Mises* distribution ρ fits the measured data ρ_{m}, the closer the value of R^2 is to unity.

2.3 Results

Approximately 50 fiber angles were measured for each histological tissue section. Depending on the width and quality of the samples we were usually able to obtain 1–2 picrosirius red stained planar sections from the intima, 2–3 from the adventitia and 3–4 from the media from each sample. Given the number of samples (11 human aortas including the common iliac arteries), the total number of recorded fiber angles from all tissue sections was over $37,000$. Analysis of the layer-specific data from the samples investigated for the locations T to CI allowed us to determine: the number of fiber families, the mean angular data such as the azimuthal mean (Eulerian) angle Φ_{m} and the elevation mean (Eulerian)

Location		No. of fiber families	Azimuthal data (°) Φ_m	AD	Elevation data (°) Θ_m	AD	Fitting data κ	R^2
Intima	T	2–4	41.15 −39.48	22.07 23.11	4.02	9.44	0.052	0.60
	A	2–4	38.37 −37.14	23.39 23.92	1.42	8.53	0.048	0.55
	CI	2–3	45.02 −42.37	24.73 23.94	0.63	9.49	0.055	0.18
Media	T	2	27.75 −27.19	15.30 15.18	1.66	7.89	0.046	0.74
	A	2	24.79 −24.91	14.44 14.96	0.14	7.51	0.039	0.82
	CI	1	−0.11	19.70	−0.34	8.58	0.060	0.63
Adventitia	T	2	53.21 −50.55	17.30 16.74	−0.99	9.47	0.055	0.73
	A	2	50.09 −47.75	18.76 18.76	1.07	9.45	0.059	0.64
	CI	2	53.30 −54.27	17.55 18.08	1.43	9.32	0.054	0.69

Table 2.1: Layer-specific data from all 11 subjects of the descending thoracic aorta T, the abdominal aorta A, and the common iliac artery CI (compare also with Fig. 2.1). Summarized are number of fiber families, mean angular data such as azimuthal mean angle Φ_m and elevation mean angle Θ_m, then corresponding angular deviation (AD), dispersion parameter κ, and minimized R^2-value.

angle Θ_m, the corresponding angular deviation AD, the dispersion parameter κ, and the minimized R^2-value as a measure of the goodness-of-fit. Because no significant difference between the mean fiber directions was found among the locations T1–T3 and A1–A3, we summarized these data into the thoracic region T and the abdominal region A. All resulting data are summarized in Table 2.1.

Note that the listed mean fiber angles are obtained from the entire data using all subjects, hence yielding the overall mean values Φ_m and Θ_m. The dispersion parameter κ also represents a mean value, however, it is obtained by fitting the model only to data relating to two fiber families in the intima (omitting fiber orientations in the circumferential and axial directions) and to all data for the media and the adventitia. As can be seen from the table, we found that the mean angle Θ_m is close to 0° for all locations *and* for all three arterial layers. Consequently, the collagen fibers at all locations of the investigated vessels are located close to the tangential plane, i.e. the *x*-*y* plane.

Overall, the arterial layers from all locations showed two very distinct counter rotating fiber families, with a few exceptions, i.e. for the media of the common iliac artery, and the intima along the aortas and the iliac artery. Figure 2.4, for example, displays three representative images from the intima, the media, and the adventitia at location T2, all showing two distinct fiber families located in the *x*-*y* plane. We observed that in the media

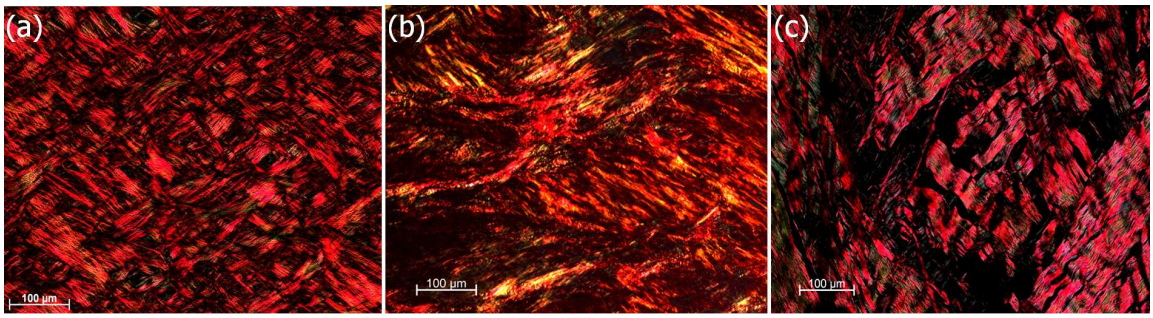

Figure 2.4: Representative polarized light micrographs, using crossed polars, of picrosirius-red stained sections of (a) the intima, (b) the media, and (c) the adventitia of the thoracic aorta. All three images show two distinct collagen fiber families located in the *x*-*y* plane of the arterial wall. The horizontal and vertical sides of the image denote the circumferential and axial directions, respectively.

and adventitia the two collagen fiber families are organized in separate layers (each layer containing one preferred fiber direction), which is observable by the appearance of a kind of 'plywood' structure when cutting through several of such layers. In the intima this organization in layers was less clear, the two fiber families displayed a 'carpet-like' structure, as shown in Fig. 2.4(a).

Remarkably, in the media of the common iliac artery we observed a very different result from two distinct fiber families to only one, which is oriented in the circumferential direction. In the case of the intima we observed a higher fiber dispersion with a varying number of fiber families, ranging from 2–4. The intimas of the thoracic and abdominal aortas showed up to four fiber families, while the intima of the common iliac arteries showed up to three. It is important to emphasize that not all intimas investigated had more than two fiber families, but that two prominent fiber families, placed between the major axes in the *x*-*y*-plane, were always visible. Several intimas showed a third peak in the axial direction and a fourth peak oriented circumferentially. To visualize the varying number of fiber families between the different locations, we provide an overview of the azimuthal angles Φ of the data from all samples in Fig. 2.5.

The analysis of the total wall thickness for the descending thoracic and abdominal aortas and the common iliac arteries yielded 1.39 ± 0.18 mm, 1.39 ± 0.16 mm, and 1.05 ± 0.15 mm, respectively. No significant variations in the thicknesses between the locations T1–T3 and A1–A3 were observed. While the descending thoracic and abdominal walls have the same thickness, we found a decrease of about 25% for the wall of the common iliac artery. Layer-specific changes in the thickness along the descending aorta, from T1 to A3 are shown in Fig. 2.6. Due to the much thinner wall of the common iliac artery we decided not to include these data in Fig. 2.6, because it would have distorted trends in the linear regression. Although not statistically significant, the overall wall thickness appeared to remain almost constant ($R^2 = 0.17$), while a slight thickening of the intima ($R^2 = 0.26$)

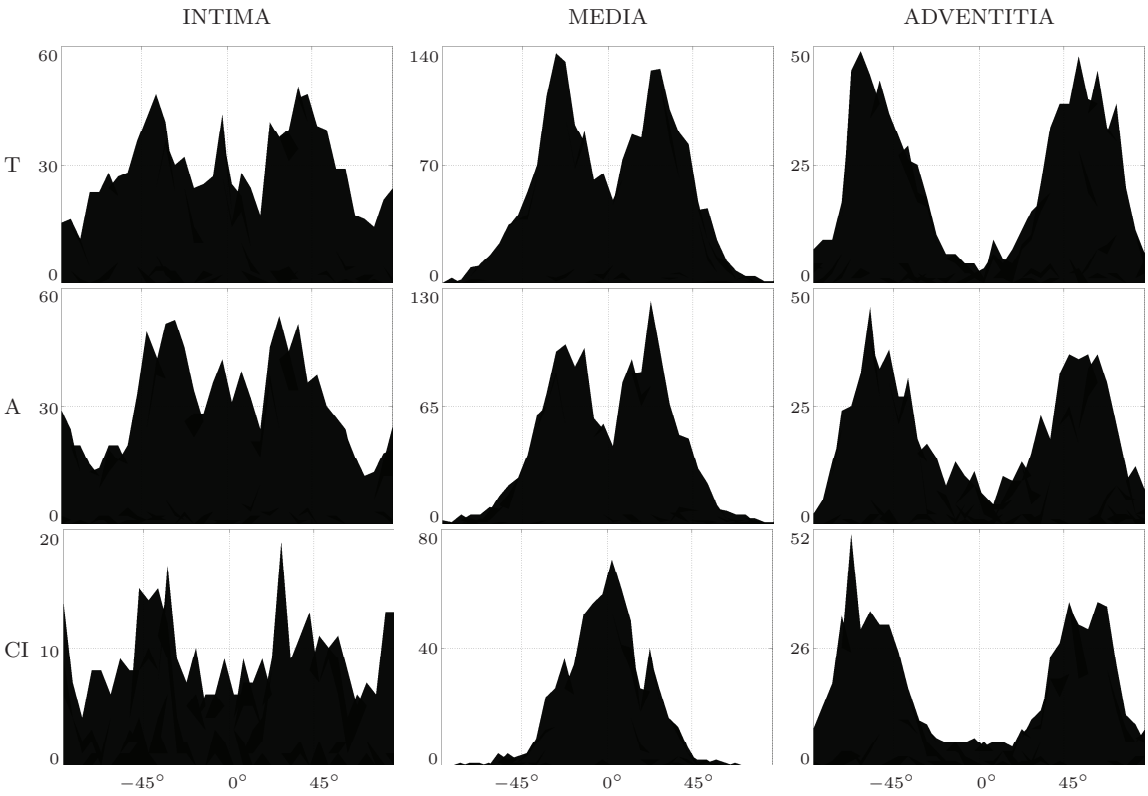

Figure 2.5: Layer-specific overview of the totality of the azimuthal angles Φ with respect to the reference configuration ($\Phi = 0^\circ$ is circumferential) from all subjects as a function of the location along the aortas and the common iliac arteries. The X-axis denotes $\Phi \in [-90^\circ, 90^\circ]$, the Y-axis denotes the density of the measured angles for the descending thoracic aorta T, the abdominal aorta A, and the common iliac arteries CI.

and a thinning of the media ($R^2 = 0.75$) in increasingly distal regions were observed. No significant variations were found for the adventitia ($R^2 = 0.27$).

Because the thickness of the arterial intima is not uniform due to adaptive intimal thickening [151], and the absolute thickness values might be misleading, we also provide intima/media and intima/media/adventitia ratios in Table 2.2. The listed values in Table 2.2 were calculated from the averaged mean thickness data using all subjects, therefore, yielding mean values for the thickness ratios. In Fig. 2.7 we illustrate the total wall thickness for the thoracic and abdominal aortas as a function of age for the limited number of subjects available (the positive slope of the linear regression is statistically not significant: $R^2 = 0$). An analysis of sex-related thickness variations for the total wall also showed no significant results.

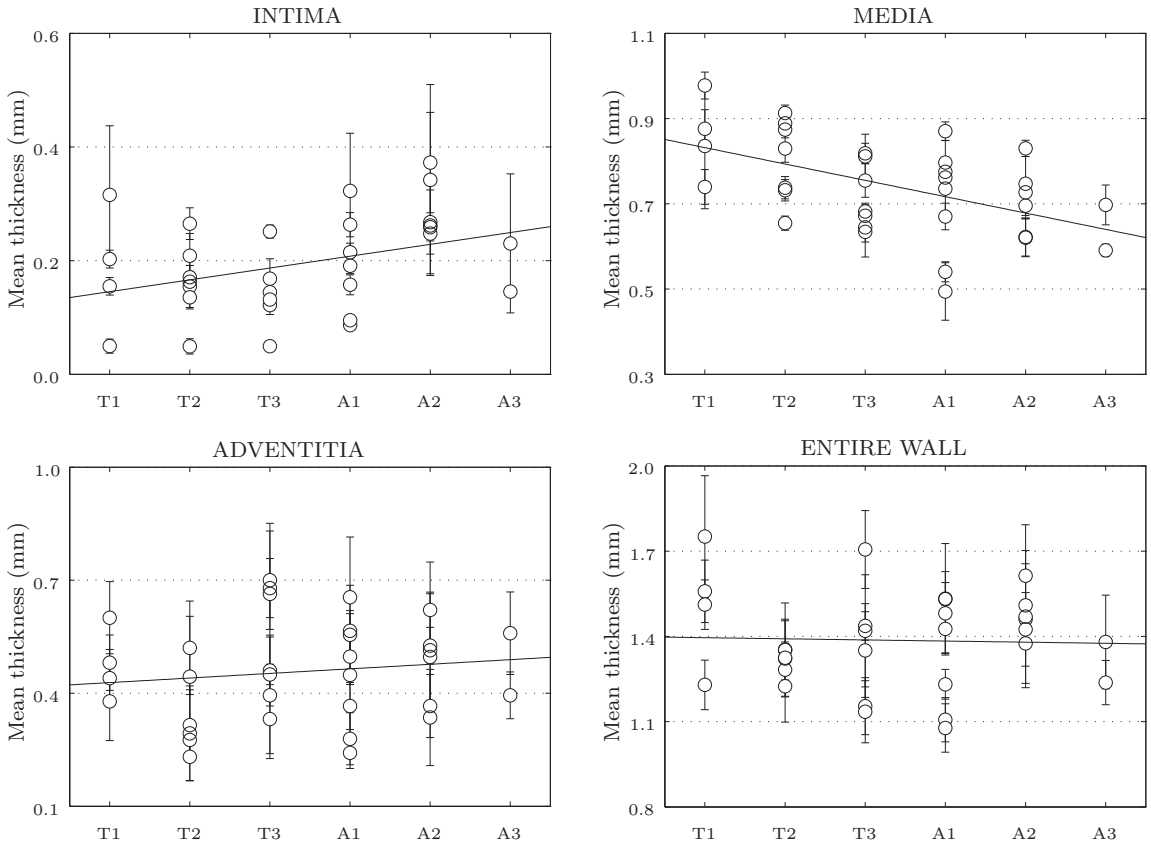

Figure 2.6: Layer-specific thickness data from locations T1 to A3 according to Fig. 2.1. To avoid distortions in the linear regression, data from the much thinner common iliac arteries were not included.

2.4 Discussion

The importance of collagen fiber angles on the mechanical behavior of arterial walls has been well-studied and established in the literature, see, for example, [56, 122, 140, 155]. Because of strong legal and institutional restrictions, only limited structural data on many human tissues are currently available. To our knowledge, this is the first experimental investigation on the structure of collagen fibers in human aortas and common iliac arteries with non-atherosclerotic intimal thickening. We were able to quantify the layer-specific distribution of collagen fiber orientations along the aortas and the common iliac arteries for the first time, providing essential data on the structural composition of the vessel walls. This study has demonstrated the strong variation and dependence of the distribution of collagen fiber orientations on the specific tissue location and especially on the wall layer.

Location	I/M (%)	I/M/A (%)
T1	21/79	12/57/31
T2	20/80	13/61/26
T3	20/80	10/52/38
A1	27/73	14/52/34
A2	41/59	20/48/32
A3	29/71	14/49/37
CI	33/67	14/44/42

Table 2.2: Intima/media and intima/media/adventitia arterial wall thickness ratios (in %) for the descending thoracic T1–T3, the abdominal aortas A1–A3, and the common iliac arteries CI. All values were obtained from the averaged mean thickness data using all subjects.

2.4.1 Fiber angle measurements

In our experiments we measured over 37,000 fiber angles from non-atherosclerotic descending thoracic and abdominal aortas and from common iliac arteries, providing a large body of data relative to previous studies on different arteries [136, 139]. The results of our analysis show two clear fiber families for the intima, media and adventitia in both the thoracic and abdominal aortas, with often a third and sometimes a fourth family of fibers present in the intima in the axial and circumferential directions. For the investigated human aortas the two families are almost symmetrically arranged with respect to the cylinder axis and are closer to the axial direction in the adventitia, closer to the circumferential direction in the media and in between in the intima, as shown in Table 2.1 and Fig. 2.5. The same trend was found for the intima and adventitia of the common iliac arteries; however, there was only one fiber family present in the media of the common iliac arteries. The differences of the mean fiber angles among different layers of the thoracic and abdominal aortas (more circumferential for the media and more axial for the adventitia) were expected to a certain degree. These differences correlate well with the mechanical response demonstrated in uniaxial tension tests on human iliac arteries, where a higher stiffness for the adventitia tested axially and the media tested circumferentially has been reported [58, 76]. However, it is important to note that the biaxial layering of the collagen fibers in the descending aortic media is not a universal quality among elastic arteries, as our results for the fiber distribution of the media in the common iliac artery show, where a unimodal distribution was observed (see Table 2.1 and Fig. 2.5).

In human brain arteries a highly aligned medial collagen in the circumferential direction has been documented [136, 139]. This result correlates well with our findings for the media in the common iliac arteries, but differs significantly for the media in the thoracic and abdominal aortas. The differences are not unexpected due to the different functions of the human aorta which is exposed to high circumferential elastic strain and a smoothing of blood pressure (systolic-diastolic) is important, versus brain arteries which are of the muscular type. Two helically-arranged fiber families (with different orientations in differ-

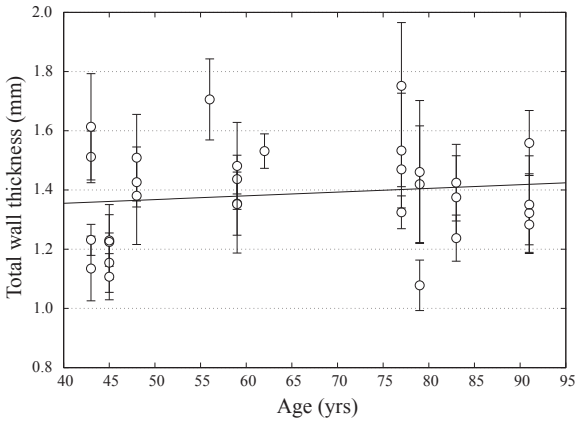

Figure 2.7: Age dependency of arterial wall thickening.

ent layers) in the elastic aorta allow the necessary distensions to absorb pulsating pressure waves originating from the heart, and also form a net-like structure to prevent the vessel wall from overstretching at increased blood pressures. A widely distributed collagen fiber orientation about a mean axial direction was reported for the adventitia in the brain arteries [136]. A mean helical orientation of 53° (0° is circumferential) was documented in [139], but the presence of two fiber families was not reported. At physiological (*in vivo*) pressures the media is the mechanically most significant layer with its more circumferentially oriented fibers in a healthy artery. The less stiff adventitia, however, adds additional structural integrity to the wall by forming a 'jacket-like' tube at elevated pressures [56].

In the intimal layer we consistently observed two fiber families, while often a third and sometimes a fourth (additional) fiber family was found in the axial and circumferential directions, respectively. Our finding of two prominent helically organized fiber families in the intima (symmetrically arranged with respect to the cylindrical axis) was also documented for the subendothelium of human brain arteries in [156]. As depicted in Fig. 2.5, there is generally a much wider range of fiber orientations present in the intima than in the media and adventitia. We did not find any significant correlation between the additional (third/fourth) fiber families and age or sex for our limited number of 11 subjects.

2.4.2 Statistics

We fitted the dispersion in prominent fiber families with a rotationally symmetric π-periodic *von Mises* distribution, as suggested in [122]. The listed dispersion data κ in Table 2.1 are mean values of both main fiber families (see Fig. 2.5), except for the media of the common iliac artery where only one fiber family was detected. A third or fourth fiber cluster in the intima was not included in the analysis. The dispersion parameter κ is lower in the media when compared to the adventitia, in the regions T and A. The result is also visible

in Fig. 2.5, where the peaks in the adventitia plots are slightly wider than the peaks in the media plots.

The R^2-values show that the symmetric *von Mises* distribution is certainly not an ideal statistical distribution for the obtained experimental data. While other non-symmetrical distributions might be more suited to fit our data, we want to emphasize that the rotationally symmetric *von Mises* was specifically chosen because it allows for the calculation of a single dispersion parameter κ (as introduced in [122]) yielding a quantitative value for the anisotropy within the framework of a two-fiber family material model, which has been implemented in various finite element analysis programs such as ABAQUS (Simulia Corp., RI, United States) and FEAP (University of California at Berkeley, CA, United States).

Although the study [157] documents some salient structural quantities in regard to arterial morphology, the present work highlights the fact that these quantities are highly layer-specific. We made no *a priori* assumptions regarding the number of fiber families; we measured distributions as a function of direction. From these data then we concluded mean fiber directions, fiber families and corresponding dispersions. By pre-stretching the arterial samples we have attempted to properly account for the *in vivo* condition. For the specific choice of circumferential and axial tissue pre-stretch (22% and 12%, respectively) we were guided by the work of [148] and [149]. The 22% circumferential strain is not matched to a known transmural pressure. While we believe that our data representation of overall mean values is well suited for illustrating the layer-specificity of our findings (see Table 2.1), we want to emphasize that one must always be respectful of the variability among different subjects, for example, in the present study a specific mean azimuthal angle can vary up to 8° among individual subjects. Although our reported angular deviations capture such variabilities statistically, we would like to accentuate that one needs to recognize such biological variations rather than seeking universal 'truths' in biological, physiological, or anatomical function.

2.4.3 Wall thickness measurements

We performed detailed thickness measurements, which resulted in a mean total wall thickness for the descending aorta of 1.39 ± 0.18 mm, 1.39 ± 0.16 mm for the abdominal aorta, and 1.05 ± 0.15 mm for the common iliac arteries. These values correlate well with the thicknesses documented in [158] for the non-atherosclerotic abdominal aortas, while in a multiethnic study of atherosclerosis the observed aortic wall thicknesses were significantly higher, in the range of 2.11–2.32 ± 0.06 mm, [159]. A similar result was shown for aortas with second- or third-degree atherosclerosis, where increased wall thickness was documented [160].

Our layer-specific analysis of the thoracic and abdominal aortas demonstrated a slight thickening of the intima and a thinning of the media in increasingly distal regions, while

the overall tissue thickness remained constant. Based on guidelines from the American Heart Associations' Council on Arteriosclerosis [151], we calculated the intima/media ratio as a method to determine normal intima thickness, and our results of 0.3–0.7 (see Table 2.2) are well within the range of normal human arteries. Interestingly, while the intima/media ratio remains almost constant for the thoracic aorta, a clear intimal thickening can be observed distal to location A1, starting at the branching of the celiac arteries where constant blood flow is disturbed. This regional observation also correlates well with the preferred locations for diffuse intimal thickening, between the orifice of the inferior mesenteric artery and the bifurcation of the common iliac arteries [151].

Despite the limited number of subjects and their relatively advanced age (63.0 ± 15.3 yr) we found that wall thickening depends (slightly) on age, as shown in Fig. 2.7. While the overall trend is consistent with documented data [159, 160], we would expect a stronger dependence of tissue thickness with age if younger subjects (with very little or no intimal thickening) were included in our analysis.

2.4.4 Implications for vascular physiology

Our results provide novel data on the structure of human arterial walls, with implications for the physiological performance of arteries with non-atherosclerotic intimal thickening. Significant differences in the mechanical behavior in both axial and circumferential directions have been established in the literature [76], but the underlying principle of such an anisotropic behavior has yet to be fully understood. While some authors already hypothesized that fiber angles might be responsible for the mechanical behavior [58], our structural data have the potential to provide a foundation for understanding these experimental observations.

The different responses of arteries (for example, aorta versus cerebral artery) are governed by the structure of the wall. Since the collagen fibers are the structurally most important constituent of the wall, and the significant influence of fiber dispersion on the mechanical properties has been established [155], our layer-specific data on the number of fiber families and the fiber angles (including their dispersion) constitute a step forward in the biomechanical understanding of the functions of human aortic walls and the walls of common iliac arteries.

Our expected observation of differences in fiber arrangement between the intima, media and adventitia explains the previously reported mechanical and functional differences of the three arterial layers [56, 58]. One of our key results show a variation of fiber distribution of the media among elastic arteries (descending aortic media versus common iliac media). This affirms that structural vessel composition cannot be assumed to be the same

even within a single species, much less among different species [74]. Therefore, experimental data from human tissues like those presented here will become increasingly indispensable for identification of pathological progressions and material modeling of arteries. In the future, studies of the influences of cardiovascular diseases such as atherosclerosis on the collagen fiber distribution in arterial tissue (compared to healthy tissue) would be a natural extension of the work presented here.

Limitations. To approximate *in vivo* stretches and ensure straightened collagen fibers our samples were stretched biaxially, yielding a planar geometry for each tissue sample. While this geometry was necessary to obtain in-plane histological sections for microscopical measurements, it does deviate from the (uncut) cylindrical *in vivo* shape of arteries, which could have caused slight changes in the mean fiber directions.

When measuring collagen fiber angles using polarized light it is a great challenge to ensure correct fiber sampling, because the nature of the method 'invites' the microscopist to preferably measure the more visible (brighter) fibers, therefore, possible biasing away from weaker fibers. Additionally, the usage of the universal stage does not allow for the use of a grid pattern in deciding on the location of the measurements in a practical manner. With this in mind we tried to sample as fairly as possible, but cannot completely exclude some human bias during measurements.

Another limitation of this study is that it does not allow the measurement of fiber angles continuously throughout the entire wall (in the radial direction, see Fig. 2.3), and we want to emphasize that our results are mean values for each layer. Because of the small variations in mean fiber directions among our investigated samples (see Results), we do not believe that major changes occur within each arterial layer.

Acknowledgement. The authors thank Mohamed Al-Effah for preparing histological sections of the arterial specimens. They gratefully acknowledge the generous help of Professor Peter B. Canham, The University of Western Ontario, Canada, who suggested valuable improvements to the substance of the text. Furthermore, we gratefully acknowledge the financial support of the European Commission under the 7th Framework Programme in the scope of the project SCATh – Smart Catheterization, Grant Agreement Number 248782.

3 COLLAGEN AND THROMBUS REMODELING IN DISSECTING AORTIC ANEURYSMS

Abstract. Fibrillar collagen endows the normal aortic wall with significant stiffness and strength and similarly plays important roles in many disease processes. For example, because of the marked loss of elastic fibers and functional smooth cells in aortic aneurysms, collagen plays a particularly important role in controlling the dilatation of these lesions and governing their rupture potential. Recent findings suggest further that collagen remodeling may also be fundamental to the intramural healing of arterial or aneurysmal dissections. To explore this possibility further, we identified and correlated regions of intramural thrombus and newly synthesized fibrillar collagen in a well-established mouse model of dissecting aortic aneurysms. Our findings suggest that intramural thrombus that is isolated from free-flowing blood creates a permissive environment for the synthesis of fibrillar collagen that, albeit initially less dense and organized, could protect that region of the dissected wall from subsequent expansion of the dissection or rupture. Moreover, alpha-smooth muscle actin positive cells appeared to be responsible for the newly produced collagen, which co-localized with significant production of glycosaminoglycans.

3.1 Introduction

Thoracic aortic aneurysms (TAAs) and abdominal aortic aneurysms (AAAs) are responsible for significant morbidity and mortality, with younger individuals (< 60 years old) affected more by the former and older individuals (> 70 years old) increasingly affected more by the latter in our aging society. Despite differences in etiology and natural history, fundamental mechanisms are shared by these two classes of lesions, including loss of elastin, apoptosis of smooth muscle, and remodeling of collagen [161, 162]. There is a continuing need, however, for an increased understanding of the biochemomechanical conditions that lead to dilatation, dissection, and rupture [107, 163, 164]. Motivated largely by the difficulty of collecting sufficient longitudinal information on lesion morphology, histology, cell biology, and biomechanical properties in humans, various animal models have been developed to study aortic aneurysms (cf. [165]). Of the different models, continuous subcutaneous infusion of angiotensin-II (Ang-II) in the apolipoprotein-E null (ApoE$-/-$) mouse has emerged as the most commonly used method to generate dissecting aortic aneurysms (e.g., [166–175]). Via these and many similar studies, it appears that these lesions initiate following an accumulation of macrophages within the media, which produce cytokines and proteases that lead to degradation, dissection, and dilatation

of the wall. Hence, although these lesions occur primarily in the suprarenal abdominal aorta, they exhibit some features (e.g., dissection and intramural thrombus) that are more common to TAAs than to AAAs in humans. Regardless of localization, for the purposes herein, lesions arising from the infusion of Ang-II in ApoE$-/-$ mice provide an excellent model of a dissecting aortic aneurysm, including development of an intramural thrombus and possible subsequent healing of the dissected wall.

Notwithstanding the availability of significant information on the histology and cell biology associated with the Ang-II mouse model of dissecting aneurysms (cf. [176] and references therein), little attention has been directed towards the turnover of fibrillar collagens and possible roles played therein by intramural or intraluminal thrombus. Because of the marked loss of elastic fibers and functional smooth muscle cells within the aneurysmal wall, fibrillar collagens play particularly important mechanical roles in controlling the rate of enlargement and governing the rupture-potential [107]. In particular, given that collagen is very stiff when straight (with an elastic modulus on the order of 1 GPa), vascular distensibility depends largely on the degree of undulation of the collagen fibers as well as on their density, fiber diameter, interactions with other matrix proteins and glycoproteins, and cross-linking [177]. In this paper, we examine for the first time the waviness and density of fibrillar collagens at different locations within serial cross-sections along the length of dissecting aortic aneurysms that developed due to a 28-day infusion of Ang-II, with particular attention to the replacement of intramural thrombus with fibrillar collagen during this period.

3.2 Methods

3.2.1 Animal Model

All animal protocols were approved by the Texas A&M University Institutional Animal Care and Use Committee. Following other reports (e.g., [166]), 8-week old male ApoE$-/-$ mice were anesthetized with isoflurane and implanted subcutaneously in the mid-scapular region with an Alzet mini-osmotic pump (Durect Corp., CA). These pumps delivered Ang-II continuously at 1000 ng/kg/min. Following 28 days of treatment with Ang-II, while maintained on a normal diet, the mice were euthanized with an overdose of sodium pentobarbital. The suprarenal aorta was then isolated via a mid-line incision and photographed, large branches were ligated with 7-O silk, and the vessel was excised en-bloc. Following biomechanical testing [178], the vessels were fixed in an unloaded configuration using a buffered 10% formalin.

3.2.2 Histology

Suprarenal aortas from five, 12-week old mice that developed significant aneurysms (>1.5 fold increase in outer diameter) were cut into distal and proximal halves, embedded in paraffin (both halves in one block), and sectioned at five microns. Serial cross-sections were obtained for each half of the specimen at three axial locations separated by 880 microns, hence yielding 6 sets of axially located cross-sections per lesion. Supplemental Fig.1 gives an overview of the many resulting cross-sections for each vessel and thus illustrates the sectioning protocol. Sections were then stained with Verhoeff Van Gieson (VVG) to highlight elastin, picrosirius red (PSR) to highlight fibrillar collagens, Alcian blue to highlight glycosaminoglycans (GAGs), and Movat's pentachrome to identify fibrin, elastin, collagen, and glycosaminoglycans within a single section. Additional sectionswere immunostained for α-smooth muscle actin (αSMA). All images were acquired with an Olympus BX51TF microscope using an Olympus DP70 camera in combination with Olympus CellSens Dimension 1.4.1 software. In the case of the PSR-stained sections, images were acquired using appropriate polarizing optics and dark-field imaging; all other images were acquired using bright-field imaging. Magnification was typically set at $10\times$ or $20\times$.

3.2.3 Image Analysis

As a measure of collagen waviness, we computed the 'entropy' H from dark-field PSR-stained images collected from multiple locations within each cross-section. Straighter (more organized) fibers yield lower values of entropy whereas increasingly wavy (more disorganized) fibers yield higher values of entropy. Toward this end, each original dark-field image was first converted to an 8-bit $(0-255)$ grayscale image that was then partitioned into five smaller images at each location to define multiple computational sub-domains for each calculation of waviness (Fig. 3.1a). Each sub-domain was then divided into $m \times m$ pixel regions of interest (ROI), thus yielding n ROIs at each location of interest (cf. Fig. 3.1b). The collagen fiber organization within each ROI was then represented by a distribution function $f(x,y)$, where (x,y) defines each point p in a 2-D real space. This distribution function was then transformed to the Fourier space using a 2-D fast Fourier transformation, which yielded $\mathcal{F}(f(x,y)) = F(u,v)$, where (u,v) is the associated point in Fourier space. The zero-frequency components were then shifted to the center and, finally, the 2-D power spectrum P of the Fourier transform (FT) was obtained by multiplying the FT with its complex conjugate*, namely

$$P(u,v) = F(u,v) \cdot F^*(u,v). \tag{3.1}$$

The overall collagen fiber orientation within each ROI was then obtained by fitting a line through the center of the power spectrum in a least square sense [179]. The orientation of

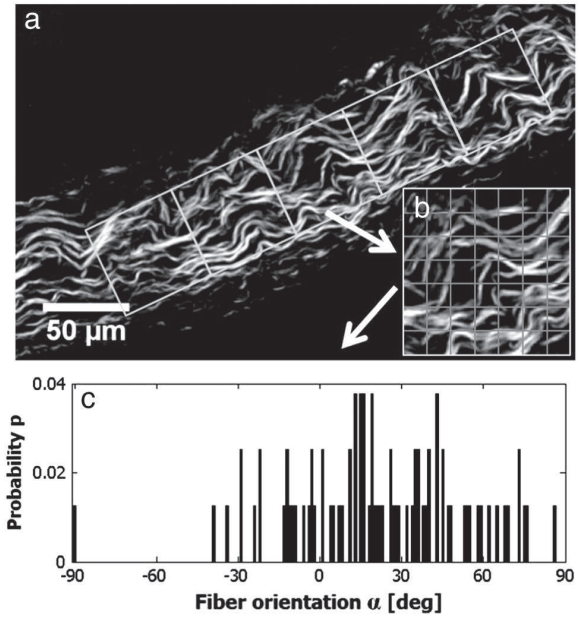

Figure 3.1: Schematic of steps to compute entropy H as a measure of collagen waviness or disorder. (a) An original dark-field image of a portion of the PSR-stained adventitia is shown with five associated sub-domains defined for separate computations. (b) Each sub-domain was divided into $m \times m$ pixel regions of interest (ROIs) as shown by the light grid lines in this representative sample. (c) The overall fiber orientation α was determined for each ROI and plotted as a normalized histogram to yield the probability mass function p as defined in the text.

the line yields the angle α as a measure of the overall fiber orientation for each ROI. All angles were then plotted as a histogram to yield a probability mass function $p(\alpha_i)$, which was normalized to $\sum_{i=1}^{n} p(\alpha_i) = 1$ (Fig. 3.1c). Finally, the entropy H was calculated from the probability mass function to yield a scalar measure of waviness of the collagen fibers, that is,

$$H = -\sum_{i=1}^{n} p(\alpha_i) \log_2 p(\alpha_i), \tag{3.2}$$

with n denoting the number of ROIs at each location of interest [180].

To quantify the local density (or, 'concentration') of the fibrillar collagen, we determined the area fraction of collagen present at multiple locations within each dark-field image. This quantification was performed on the same five computational sub-domains per location that were used to quantify waviness (cf. Fig. 3.1a). This concentration was determined by calculating the ratio of colored pixels (representing the birefringent collagen fibers) to the black background for each domain. We emphasize that the term 'concentration' is used loosely as a synonym for area fraction within a 2-D image and, therefore, should not be confused with the biochemical term concentration, as, for example, dry weight of collagen. All image analyses were performed using custom codes written in Matlab

(MathWorks Inc., MA, USA). For isolating colors and applying color thresholds, we used ImageJ (U.S. National Institutes of Health, MD, USA).

3.3 Results

Consistent with prior reports (e.g., [166]), AAAs excised from the five mice following 28 days of continuous infusion of Ang-II tended to involve most of the suprarenal aorta and to be on the order of 2.2 mm in maximum unloaded outer diameter. In comparison, the normal unloaded outer diameter is on the order of 0.8 mm [181]. Hence, Ang-II resulted in a mean 2.75-fold localized increase in diameter, consistent with the term aneurysm, which means 'widening' and is generally considered pathologic if the diameter increases by 1.5 fold or more. Upon gross examination in a pilot study, however, the true lumen appeared to be preserved throughout much of the lesion, thus most of the gross dilatation resulted from an intramural accumulation of thrombus or extracellular matrix material (Fig. 3.2). There also existed a large parallel intramural cavity (presumably a false lumen) in some regions, which merged with the true lumen in the center of the lesion to form a much larger 'merged' lumen.

Also consistent with the gross observations (cf. Fig. 3.2), serial histological sections revealed three distinctive formations in each of the five lesions (Fig. 3.3a–c). Formation (a) consistently appeared within the region of maximum dilatation, which was typically near the center of the lesion; it was characterized by a ruptured media, that is, completely severed elastic fibers and smooth muscle at a single circumferential location within the media. This rupture allowed a large cavity, presumably a false lumen, to merge with the true lumen. This merged lumen is illustrated well in the VVG-stained cross-section shown as Fig. 3.3a wherein the wavy elastic fibers appear black and the two arrows point to the site of medial rupture. Formation (b) typically existed close to and just distal and proximal to the site of the merged lumen; it was characterized by an intact lumen and parallel cavity that were separated by what appeared to be remodeled matrix (Fig. 3.3b). Note that the true lumen in these regions was circumscribed by an intact media consisting of concentric elastic lamellae as expected of a normal aortic wall (cf. [181]). Formation (c) was found the farthest from the site of the merged lumen, again both distal and proximal, and was characterized by an intact true lumen and an intramural thrombus that typically consisted of fibrin (Fig. 3.3c) but in some cases GAGs and fibrillar collagen (Figs. 3.4 and 3.5). Again, the true lumen was circumscribed by an apparently normal media. It should be noted that black fragments visible on the outer perimeter in all cross-sections in Fig. 3.3 are remnant India ink, which was used in mechanical tests that are reported elsewhere [178]. Furthermore, the symbols † and ‡ in Fig. 3.3 denote locations where the waviness and concentration of fibrillar collagen were calculated, as described below.

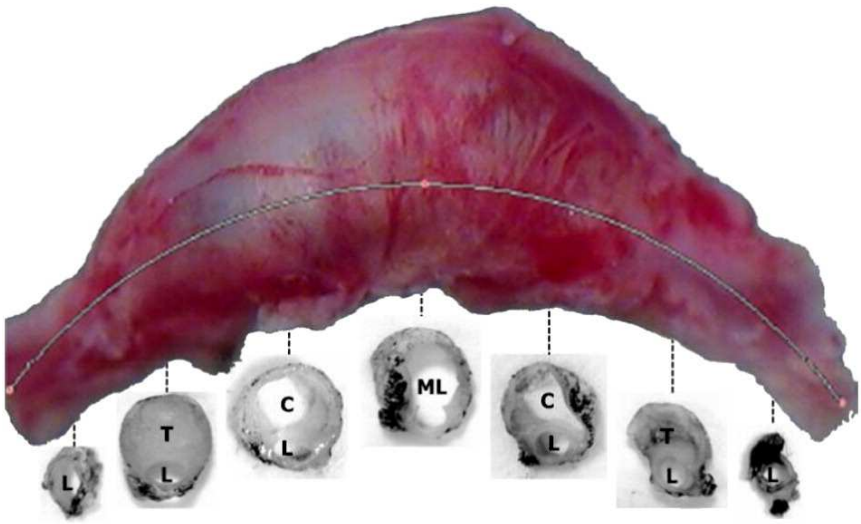

Figure 3.2: Photograph of a representative suprarenal aortic aneurysm that resulted following 28 days of a subcutaneous infusion of Ang-II in the ApoE$-/-$mouse; the maximum diameter is ~ 2.2 mm. Shown, too, are reduced magnification photographs of cross-sections obtained from regions indicated by the dashed lines: L Ű lumen, T Ű thrombus, C Ű cavity, and ML Ű merged lumen (i.e., probable merging of the true lumen L with a false lumen / cavity). As noted in the text, the thrombus contained different constituents depending on its position within the lesion as well as its distance from the region of maximal dilatation. Note that the black in the photographs of the cross-sections is India ink from a prior mechanical test.

Staining with Movat's pentachrome and PSR revealed marked spatial distributions of fibrillar collagen, fibrin, and GAGs (Figs. 3.4 and 3.5). Recall, therefore, that collagen appears brownish/gray in sections stained with Movat's pentachrome while fibrin appears pink/red, GAGs light blue, and elastic fibers black. In contrast, type I, or thick, collagen fibers appear bright red/orange whereas type III, or thin, collagen fibers appear less bright and more green/yellow in sections stained with PSR and viewed using polarized light. The large pink region in the Movat's stain in Fig. 3.4 revealed an extensive asymmetric accumulation of fibrin, with little fibrillar collagen as confirmed by the lack of bright birefringence in the associated PSR image. Yet, at some locations near the expanding adventitia, brownish/light blue colors suggested the presence of small pockets of GAGs (e.g., white asterisk in Fig. 3.4a) and collagen fibers (white arrows in Fig. 3.4b), which may mark regions where the thrombus was beginning to remodel towards a collagenous tissue. Such a deposition of GAGs and fibrillar collagen may have reflected a wound healing type response, perhaps mediated by myofibroblasts consistent with the co-localized αSMA staining (Fig. 3.4c) and known ability of this cell type to deposit significant amounts of collagen [182, 183]. Regardless, Fig. 3.5 shows nearly sequential sections that were located farther yet from the center of the lesion and stained with PSR (a), Movat's pentachrome (b), or Alcian blue (c), with thresholding used to highlight fibrin in the Movat's stain and GAGs in the Alcian blue

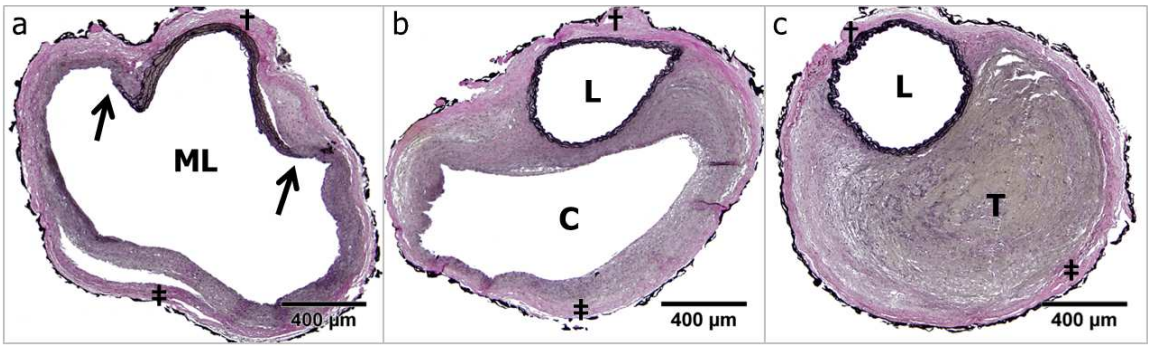

Figure 3.3: Representative Verhoeff Van Gieson (VVG)-stained cross-sections that reveal the three distinct formations that were observed in each of the five dissecting aneurysms studied. Note: the wavy elastic fibers within the aortic media appeared black; in contrast, the black fragments along the outermost perimeter are due to India ink that was used in mechanical tests that are reported elsewhere. Formation (a): merged lumen (ML), with arrows indicating locations where the media ruptured, thus allowing the true lumen and outer cavity (false lumen) to communicate. Formation (b): intact lumen (L) and cavity (C) separated by remodeled tissue; this cavity is presumably a false lumen. Formation (c): intact lumen (L) and intramural thrombus (T). The symbols † and ‡ denote locations used for subsequent analysis of the waviness and concentration of fibrillar collagen.

stain. These sections contained more collagen (Fig. 3.5a) and correspondingly more GAGs (Fig. 3.5c) and less fibrin (Fig. 3.5b) within the intramural region presumably occupied by thrombus at some time. Indeed, the collagen and GAGs tended to co-localize in regions devoid of fibrin, hence implying a replacement process.

Given that it should take some time for fibrin to break down and for synthetic cells to invade the thrombus and produce significant amounts of collagen, Figs. 3.4 and 3.5 may suggest different relative 'ages' for the thrombus, that is, times since that portion of the thrombus was either formed from or in contact with the flowing blood. Thus, one might speculate that the youngest thrombus existed closest to the center of the lesion where the merged lumen could have continued to provide flowing blood (formation (a), Fig. 3.3a), and hence fibrinogen and platelets, whereas the oldest region of the same thrombus existed farthest from the merged lumen and hence the flowing blood. This possibility is supported by findings in Fig. 3.6, which show higher magnification images $(60\times)$ of thrombus from progressively greater distances (left to right) from the patent cavity (i.e., locations separated axially by 880 microns within the same thrombus that is seen in Fig. 3.4). Note again that the spatio-temporal decrease in fibrin (pink) corresponded with the increase in GAGs (blue) and collagen (birefringent in the darkfield image). Moreover, the sequence of picrosirius red stained images (b,d,f) revealed both an increase in collagen concentration and fiber thickness (brighter red) with remodeling, or aging, of the thrombus. The 'holes' in the birefrigent images likely corresponded to locations of synthetic cells, although possibly caniculi (cf. [184]).

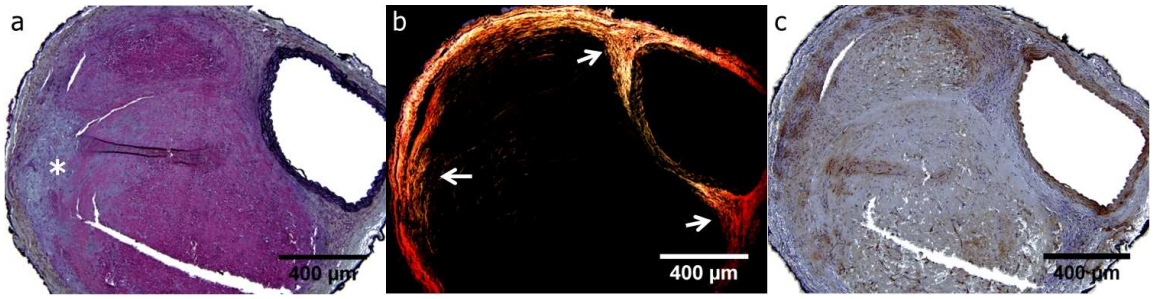

Figure 3.4: Movat's Pentachrome (a), dark-field picrosirius red (b), and alpha-smooth muscle (c) stained images of nearby aneurysmal cross-sections. Note that the Movat's stain shows elastic fibers as black, fibrin as pink/red, GAGs as light blue, and collagen as brownish/gray; the darkfield picrosirius stain shows collagen type I or thicker fibers as bright red/orange and collagen type III or thinner fibers as less bright and more green/yellow; the alpha smooth muscle strain shows both smooth muscle cells and myofibroblasts as brown. Hence, pink regions in (a) reveal thrombotic material (fibrin) that had not remodeled, which was confirmed by the lack of fibrillar collagen in the associated regions within (b). In contrast, regions wherein the pink was replaced by brownish / light blue colors in (a) indicated regions wherein the fibrin may have started to remodel, presumably via the deposition of GAGs (white asterisk in a) and fibrillar collagen (e.g., horizontal white arrow in b) by co-localized invading αSMApositive cells, which may well have been myofibroblasts.

During our examinations of sections stained with PSR, we also noticed changes in collagen organization and appearance within the adventitia when comparing regions close to the true lumen (e.g., denoted by † in Fig. 3.3) with those well away from the lumen (e.g., denoted by ‡ in Fig. 3.3). Because of the tremendous asymmetric increase in diameter, collagen well away from the lumen must necessarily have remodeled (that is, collagen can only extend on the order of 10% once straight, yet some portions of the adventitia farthest from the lumen must have elongated on the order of 150 to 200% during the 28-day period of study). Fig. 3.7 shows two darkfield images that highlight representative differences in collagen organization between locations † and ‡. Quantified differences in collagen waviness and concentration, relative to near normal values, are shown in Fig. 3.8 at these two locations for all three formations (a: merged lumen, b: lumen plus cavity, c: lumen plus intramural thrombus in Fig. 3.3). Specifically, comparisons between locations ‡ and † in the adventitia are given by dark gray bars for the three formations in Fig. 3.3 (i.e., $a-c_1$ here). In contrast, comparisons between collagen within a remodeled intramural thrombus and adventitial location † are given by the light gray bars (bar c_2). Zero denotes a waviness or concentration equivalent to that in the adventitia nearest the lumen (location †), which was assumed to be the closest to normal within this cross-section. This analysis suggested that the remodeled collagen fibers at location ‡ were always less wavy than the more normal collagen fibers at location †, which is reflected by the decrease in entropy (formations $a-c_1$). Conversely, remodeled collagen fibers within the intramural thrombus were significantly more disorganized/wavy than normal as reflected by the increased entropy (bar c_2). No significant differences were found in collagen waviness amongst the

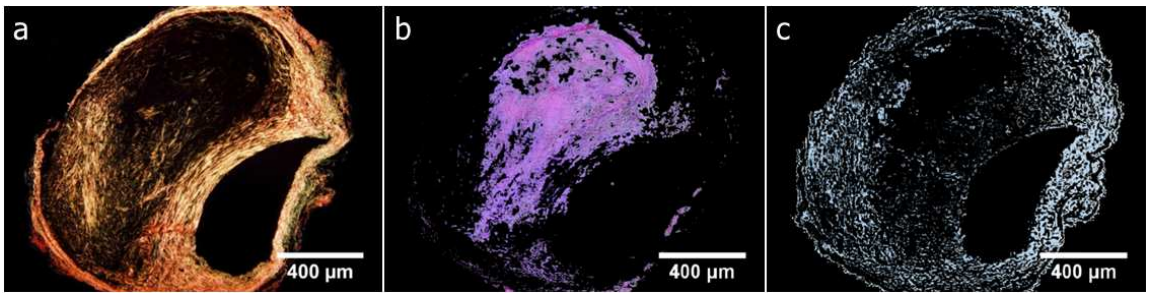

Figure 3.5: Representative images from nearby cross-sections that were located distant from the center of the lesion. Isolated constituents were highlighted by polarizing light or thresholding: (a) dark-field polarized light image of a picrosirius-stained section showing fibrillar collagen, (b) thresholded image of pink thrombus revealed by a Movat's Pentachrome stained section, and (c) thresholded image of a bluish deposition of glycosaminoglycans (GAGs) revealed by a separate Alcian blue stained section. Notice the lack of collagen in areas of fibrin-rich thrombus, but the colocalization of fibrillar collagen and GAGs in the remodeled regions. Note: The single constituents in panels b and c were extracted from the original images using color thresholding in ImageJ.

three thrombi shown in Fig. 3.6, however (i.e., the picrosirius stained images in panels (b), (d), and (f)). These objective quantitative findings were expected based on visual assessments, as, for example, when comparing collagen organization in Fig. 3.7a (more normal adventitia) with Fig. 3.6b, d, and f (remodeled intramural thrombus).

Results for the concentration of collagen (Fig. 3.8b) revealed a significant decrease in the remodeled adventitia compared to the normal adventitia (formations $a - c_1$). This finding was also consistent with our visual impression from images such as that in Fig. 3.7, wherein collagen appeared more densely packed at location † compared with location ‡. The lowest concentration of collagen fibers was found in the remodeled intramural thrombus, bar c_2, but the specific value of the concentration depended on both the location within the thrombus and the remodeling time. For example, the mean relative difference (relative to near normal collagen; cf. Fig. 3.7a) and corresponding standard errors of the mean for collagen concentration of the young, older, and oldest thrombus were $-56.8 \pm 6.2\%$, $-31.7 \pm 2.6\%$, and $14.1 \pm 0.9\%$, respectively. This progressive increase in collagen concentration appeared to be consistent with an increasing thrombus age / remodeling time (cf. Fig. 3.6).

3.4 Discussion

Angiotensin-II is a potent vasopressor having pleiotropic activity. For example, systemic increases of Ang-II in the bloodstream can cause vasoconstriction throughout the arterial tree, and thus increased systemic blood pressure; conversely, local increases of Ang-II

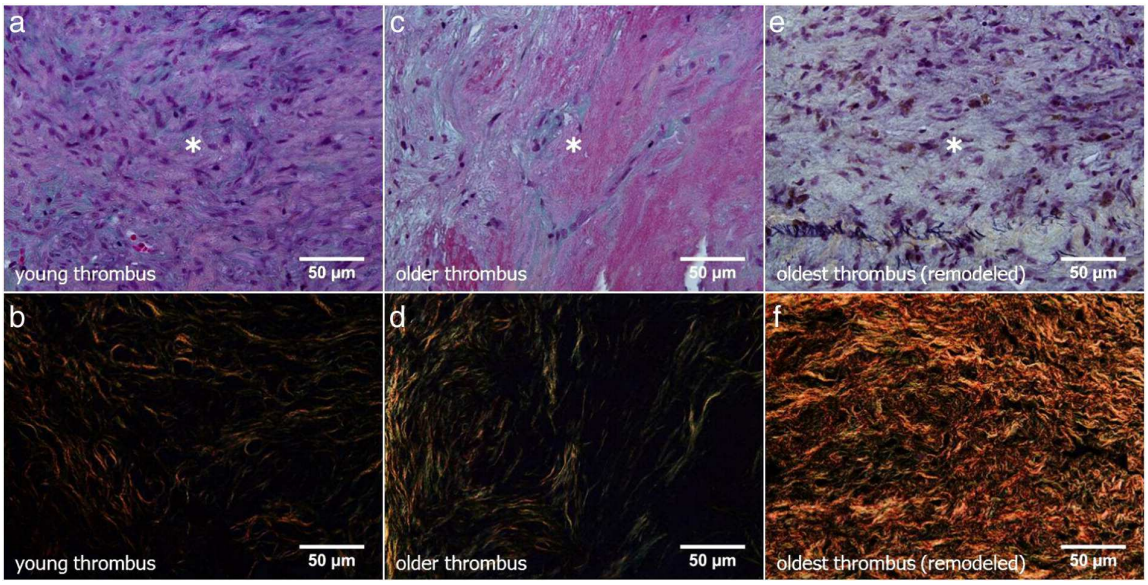

Figure 3.6: Close-up $(60\times)$ images of three regions of intramural thrombus stained with either Movat's Pentachrome (top panels) or picrosirius red (bottom panels). Panels (a) and (b) show thrombus that was closest to the center of the lesion, which likely represented the 'youngest' thrombus, that is, replenished due to its proximity to the flowing blood. Panels (c) and (d) are from the same lesion but ~ 880 microns farther from the center, and thus likely represent a slightly older thrombus. Panels (e) and (f) are from a region ~ 1760 microns away from the center of the lesion, and thus likely farthest from the free flowing blood and thereby the oldest. The series of the picrosirius-stained images (b,d,f) highlights changes in collagen structure and organization from that originally laid down around cells or canaliculi (circular structures) in the youngest (or biologically most active) thrombus (b), to more fibrillar collagen structures in (d), and finally to highly remodeled thrombus in (f). The increase in collagen concentration was consistent with the decrease of fibrin, which appeared pink/red in the Movat's stain. Recall that this dramatic remodeling took place within about three weeks.

within the arterial wall can lead to the increased production of diverse chemokines, cytokines, and proteases, which can cause significant localized remodeling of the wall. Although hypertension is a risk factor for human aortic aneurysms and dissections, [168] showed that Ang-II results in dissecting suprarenal aortic aneurysms in mice independent of blood pressure. Rather, it appears to be the macrophages and other inflammatory cells that are recruited to the media and adventitia of the suprarenal aorta that play key roles in the initiation and development of these AAAs [185] while other large arteries are spared [186]. Indeed, this concept of a localized macrophage mediated pathogenesis is consistent with the stimulation of monocyte chemoattractant protein 1 by Ang-II [187], which facilitates the recruitment of monocytes / macrophages to the aortic wall.

Although aortic lesions resulting from subcutaneous infusion of Ang-II in the mouse are typically suggested to model certain aspects of abdominal aortic aneurysms, AAAs seldom

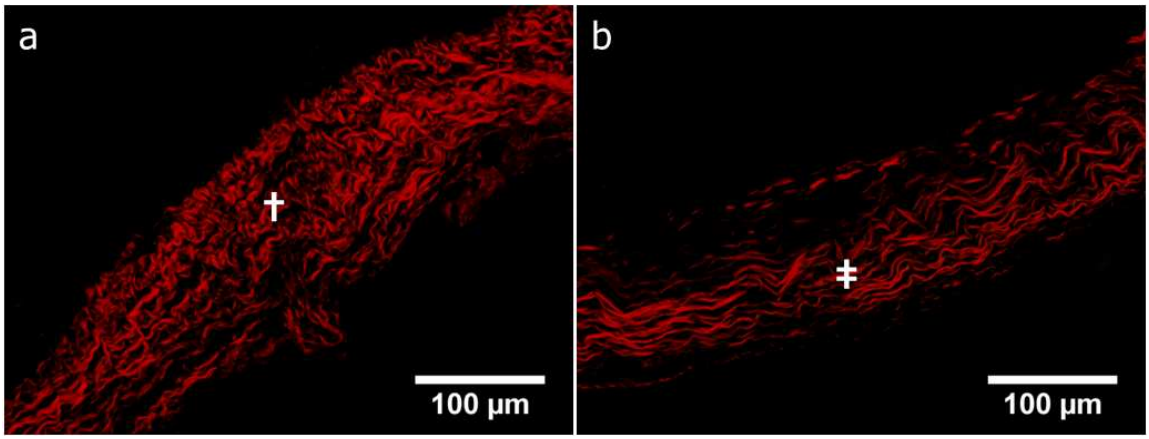

Figure 3.7: Representative dark-field images of sections stained with picrosirius red to highlight collagen fibers in the adventitia at location † (presumed nearly normal adventitia just behind the lumen) and location ‡ (clearly remodeled collagen, well opposite the site of †). Both locations are defined in Fig. 3.3.

dissect in humans. In contrast, the present findings are consistent with the early report by [173] that Ang-II induced aneurysms in the mouse arise following an aortic dissection. For this reason, this animal model may be a better model of some aspects of TAAs, which often dissect and are similarly not well understood biomechanically [161, 188]. Nevertheless, a detailed study of histological and mechanical characteristics of this mouse model will increase our general understanding of the initiation and propagation of dissecting arteries and aneurysms. Towards this end, of course, there is a need for additional longitudinal data, particularly at early time points when the lesion initiates.

Consistent with prior reports (cf. [176]), we found that the dissection at 28 days presented as three prototypically different formations along the axial direction (cf. Figs. 3.2 and 3.3): a central region wherein medial elastic lamellae fragmented completely and the true lumen merged with a false lumen; regions distal and proximal to the central region wherein the media remained intact but there existed a large intramural cavity (false lumen) without thrombus; and regions more distal and proximal to the central region wherein the media remained intact but the intramural cavity was filled with either thrombus or remodeled thrombus consisting largely of GAGs and collagen. Little prior attention has been directed toward the potential remodeling of the intramural thrombus. Note, therefore, that clinical observations in patients having a dissecting TAA suggest that a patent false lumen may be a potential risk factor for continued aortic enlargement and a poor long-term outcome, but a partially thrombosed false lumen may be of even greater concern [189, 190], perhaps due to increased plasmin activity (cf. [191]) since plasmin can activate latent matrix metalloproteinases [192]. In contrast, a fully thrombosed false lumen may be protective, serving as a first step in 'aortic wall healing and remodeling after repair' [193]. The present observations support the hypothesis that a thrombus isolated from flowing blood may al-

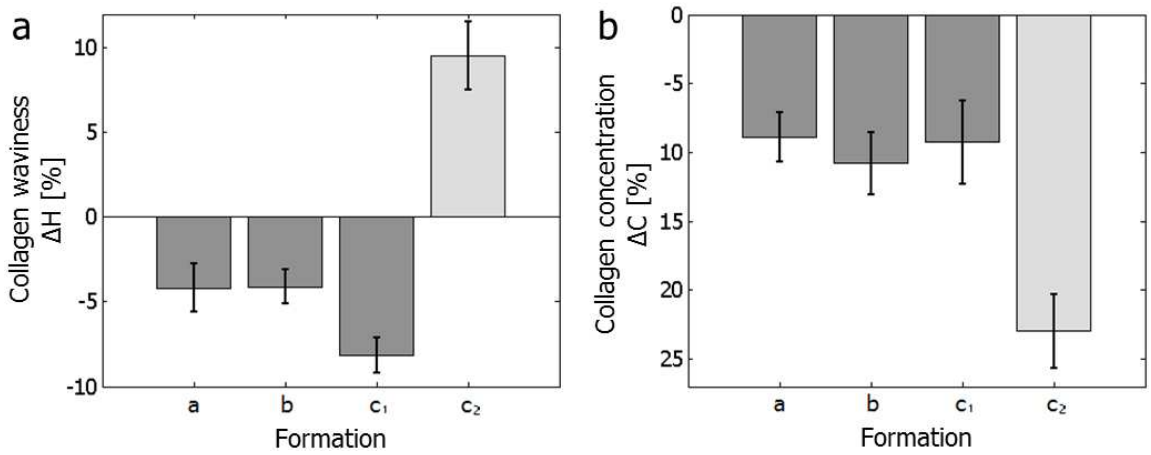

Figure 3.8: Mean relative differences (relative to near normal collagen; cf. Fig. 3.6b) and corresponding standard errors of the mean (SEM) for (a) collagen waviness and (b) collagen concentration for the three distinct cross-sectional formations present within the dissecting aneurysms. Formation (a) from Fig. 3.3 with a merged lumen (ML); formation (b) from Fig. 3.3 with an isolated lumen and cavity (L and C); formations c_1 and c_2 from Fig. 3.3 with a lumen and intramural thrombus (L and T) for regions that were either not remodeled (c_1) or remodeled (c_2) as indicated by collagen deposition. The dark gray bars (formations $a - c_1$) denote comparisons between locations ‡ and † in adventitial regions. The light gray bars (formation c_2) denote comparisons between collagen in a remodeled intramural thrombus (T) and adventitial collagen at location †. Zero thus denotes the waviness and concentration of collagen within the nearly normal adventitia behind the lumen (location †). All formations and locations are defined in Fig. 3.3.

low invading cells to replace the degrading fibrin with fibrillar collagens (cf. [194–196]), which could potentially strengthen the wall and protect it from possible further dissection or rupture, at least within that region. Indeed, this hypothesis is consistent with the tacit assumption underlying the treatment of intracranial saccular aneurysms with clot-promoting coils or flow-diverting stents. In this case, it is hoped that an intra-saccular thrombosis will form and become isolated from the bloodstream (e.g., via re-endothelialization at the orifice of the lesion), thus allowing subsequent conversion of the thrombus to collagenous tissue by invading myofibroblasts [197]. What appears to be vital, therefore, is that the intramural or intraluminal clot be isolated from flowing blood, which of course can otherwise serve as a replenishing source of platelets, leukocytes, fibrinogen (and thus fibrin), plasminogen (and thus plasmin), and so forth.

Whereas an endograft can isolate an intraluminal thrombus within an AAA from the flowing blood, such a thrombus remains in contact with the bloodstream under ‘normal’ conditions. In contrast, much of the intramural thrombus within the false lumen of a dissected artery or aneurysm could naturally become isolated from the flowing blood even if the ‘ends’ of the thrombus are never so isolated. In this case, as in the case of the coiled intracranial aneurysm (cf. [197]), it is possible that cells having synthetic capability can

invade and remodel the thrombus provided that there is sufficient oxygenation and modest levels of competing cells and biomolecules that arise from the blood Ű thrombus interface (cf. [198, 199]). Our findings support this possibility. Recall, too, that we found αSMA-positive cells within both the media, where smooth muscle cells are to be expected, and co-localized with regions experiencing new collagen and GAG deposition (cf. Fig. 3.4). It is well known that myofibroblasts exhibit heightened synthetic capability, that they are fundamental to connective tissue remodeling in many tissues and organs, and that αSMA is the most commonly used marker for this cell type [183]. Moreover, there now appears to be many possible sources of myofibroblasts, including adventitial fibroblasts and resident progenitor cells, bone marrow derived fibrocytes, smooth muscle cells, and even (via endothelial to- mesenchymal transistions) endothelial cells [182]. Although we neither attempted to confirm that the αSMA-positive cells were indeed myofibroblasts nor tried to identify cell source, our observations were consistent with a radially inward invasion of myofibroblasts from the adventitia into the thrombus (cf. Fig. 3.4), similar to that reported by [197] in a very different model of remodeling of thrombus via collagen deposition. This complex issue clearly merits further study, however, particularly given the increasing interest in adventitial cells in vascular remodeling [200].

The present findings also do not provide any further information on possible reasons why a partially thrombosed dissection may be more susceptible to further dissection or rupture. There was no indication of local adverse remodeling or failure of the wall / remnant adventitia in regions containing fibrin-rich thrombus (e.g., Supplemental Fig.2). Indeed, it appears that if the aortic wall ruptures in this mouse model, it tends to do so early in the development of the dissection (generally $4-10$ days following the initiation of Ang-II infusion; [166]), perhaps during the period when all or most of the thrombus is newly formed. We focused herein on later development, 28 days following the initiation of Ang-II, to capture different stages of thrombus development within single lesions. There is a need nonetheless to explore earlier time points further, particularly given the observation by [173] that 'Macrophage accumulation was particularly evident at the edges of the thrombi, both in regions of disrupted and intact media.' There is similarly motivation to quantify possible temporal changes in blood-borne biomarkers or factors involved in the clotting process.

Finally, we suggest one possible scenario (Fig. 3.9) that is consistent with our histological observations, that is, the existence of three distinct formations (cf. Figs. 3.2 and 3.3) in each of our five vessels and the different stages of thrombus remodeling therein. Fig. 3.9a shows the possible initiation of an intramural delamination (due, in part, to the medial accumulation of macrophages; [176]), followed by a possible propagation of this delamination in Fig. 3.9b (due to wall stresses exceeding local inter-lamellar strength) that ultimately leads to dissection along the medial Ű adventitial border and a subsequent localized transmural tear that establishes communication with the lumen. Intramural pressures caused by the blood could then contribute to the propagation of a dissection and initiate associated growth and remodeling processes within the remaining intramural constituents [201], lead-

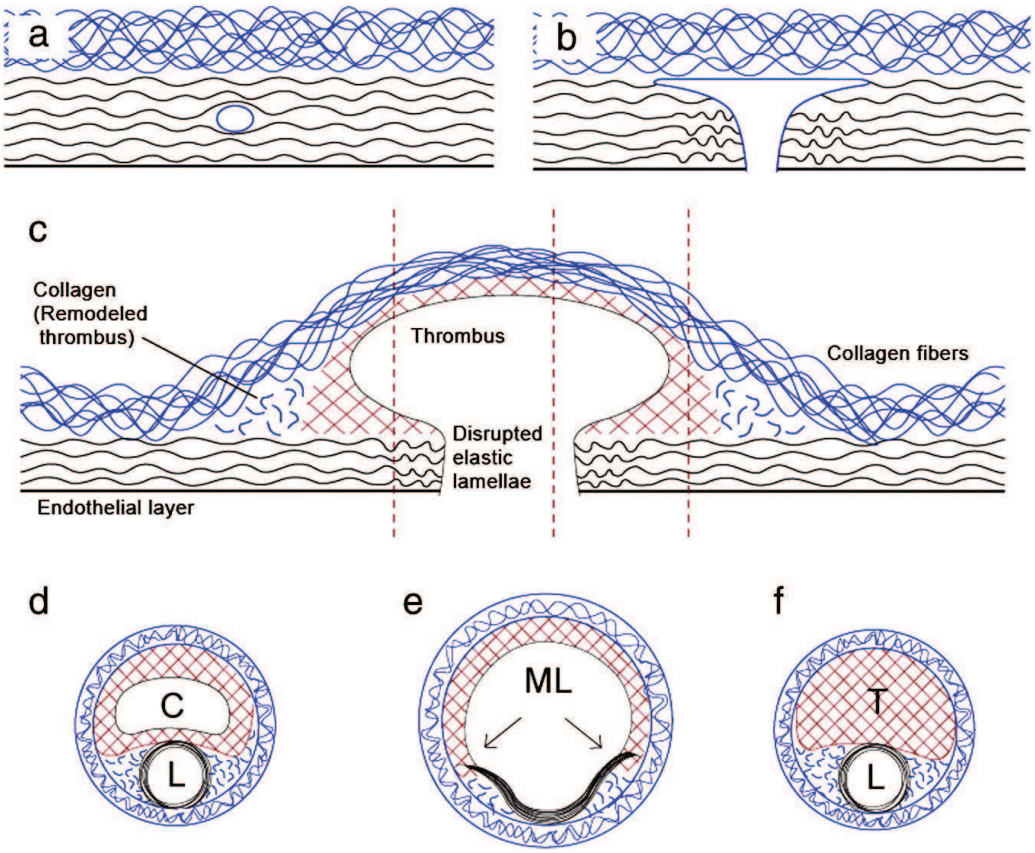

Figure 3.9: A postulated (a) intramural initiation of a localized delamination within the media of the suprarenal aorta in an ApoE$-/-$ mouse infused with angiotension-II that (b) could propagate and lead to both a dissection along the medial-adventitial plane and an intimal-medial tear, with subsequent communication with the blood stream that could allow a false lumen to extend axially (c). Moreover, consistent with Figs. 3.2 and 3.3, panels df show types of cross-sections that could arise due to the false lumen filling with thrombus on the more distal and proximal aspects, with those regions farthest from the flowing blood experiencing a replacement of fibrin with newly deposited fibrillar collagen (and GAGs). It is possible, of course, that the initial dissection could propagate within the media (not found in this study), along the medial-adventitial border, or within the adventitia, particularly if it had previously remodeled into more loosely organized collagen fibers (as often observed herein).

ing to the observed dramatic increase in vessel circumference and formation of an intramural thrombus. Regardless of the specific mechanisms responsible for the pathogenesis, Fig. 3.9c illustrates a longitudinal section as a possible scenario for an advanced, 28-day dissecting aneurysm (cf. Fig. 3.3 in [167]). Panels 3.9d$-$f show how the longitudinal section of Fig. 3.9c might appear in typical histological cross-sections, which match the three formations we observed in all five lesions (cf. Figs. 3.2 and 3.3). Additionally, relative differences in the age of the thrombus (i.e., time since it was in contact with flowing blood)

can be explained using this scenario. The youngest region of the thrombus would occur near the center of the aneurysm, where it is exposed to the blood stream via the ruptured intimal-medial layer. The oldest regions of thrombus would be farthest from the center of the lesion and not directly exposed to blood; this would allow more time, and perhaps a more permissive environment, for synthetic cells to invade the intramural thrombus and to start the remodeling process (cf. Figs. 3.4 and 3.6).

In summary, we have presented new observations related to collagen remodeling within dissecting aneurysms that arise in the most commonly employed mouse model of aortic aneurysms. The rapidly expanding adventitia clearly undergoes remarkable remodeling, but so too the intramural thrombus in regions well separated from the flowing blood. Given that replacement of thrombus by collagenous tissue may represent a favorable wound healing response, additional effort should be directed toward understanding and promoting such remodeling in arterial dissections. Insight gained could also have a broader impact, as, for example, in providing new insight relative to the use of endografts (and so-called endoleak) to treat aortic aneurysms or flow-diverting stents to treat intracranial aneurysms.

Acknowledgement. This work was supported, in part, by generous contributions to Texas A&M University by Tommie E. and Carolyn S. Lohman, grants from the NIH (R01 HL086418) and the European Commission FP7 SCATh (#248782), and a Marshall Plan Scholarship that supported A.J. Schriefl as a Visiting Assistant in Research at Yale University. We also thank Dr. E. Wilson at the Texas A&M Health Science Center for maintaining the ApoE$-/-$ colony and Dr. Y.U. Lee and Mr. J. Ferruzzi at Yale University for overseeing the initial histological preparation of the samples.

Supplementary data. Supplementary data to this article can be found online at `http://dx.doi.org/10.1016/j.thromres.2012.04.009`.

4 QUANTITATIVE ASSESSMENT OF COLLAGEN FIBER ORIENTATIONS FROM 2D IMAGES

Abstract. In this work, we outline an automated method for the extraction and quantification of material parameters characterizing collagen fiber orientations from 2D images. Morphological collagen data among different length scales were obtained by combining the established methods of Fourier power spectrum analysis, wedge filtering, and progressive regions of interest splitting. Our proposed method yields data from which we can determine parameters for computational modeling of soft biological tissues using fiber reinforced constitutive models and gauge the length-scales most appropriate for obtaining a physically meaningful measure of fiber orientations, which is representative of the true tissue morphology of the 2D image. Specifically, we focus on three parameters quantifying different aspects of the collagen morphology: first, using maximum likelihood estimation we extract location parameters which accurately determine the angle of the principal directions of the fiber reinforcement (i.e. the preferred fiber directions); second, by using a dispersion model we obtain dispersion parameters quantifying the collagen fiber dispersion about these principal directions; third, we calculate the weighted error entropy as a measure of changes in the entire fiber distributions at different length-scales, as opposed to their average behavior. With fully automated imaging techniques, such as multiphoton microscopy, becoming increasingly popular (which often yield large numbers of images to analyze), our method provides an ideal tool for quickly extracting mechanically relevant tissue parameters, which have implications for computational modeling (for example, on the mesh density) and can also be utilized for the inhomogeneous modeling of tissues.

4.1 Introduction

The mechanical behavior of the arterial wall is mainly governed by the organization and composition of the three major microstructural components, collagen, elastin, and smooth muscle cells [56, 63, 202]. The influence of these components on the cardiovascular function in health and disease has been the subject of extensive research [57, 69, 123, 125–127, 130]. While elastin is load-bearing at low and (to a smaller extent) high strains, it is collagen which endows the arterial wall with strength and load resistance, thus making it the most relevant mechanical tissue constituent [22, 134, 135, 203]. Research indicates, that changes in the mechanical properties of the healthy arterial wall play a role in arterial disease and degeneration [123]. For example, increased stiffening of the vessel wall with age may (among other factors) be related to an increased ratio of collagen to elastin as

well as increased collagen cross-linking [77, 126]. Higher wall stiffness may also be a contributing factor for atherosclerosis [69]. Furthermore, changes to the mechanical environment can lead to growth and rearrangement of collagen which can cause enlargement of intracranial aneurysms, with an associated elevated rupture risk and mortality rate of 35-50% [125]. Collagen remodeling is also believed to play a role in the healing of dissecting aortic aneurysms [61]. Therefore, evaluating and monitoring morphological data on collagen within the arterial wall is essential to facilitate a better understanding of the underlying mechanical principles governing the behavior of the vessel wall. Additionally, such data can be used to improve modeling of the cardiovascular system and increase our understanding of disease progression.

Many problems related to the mechanical function of arteries can be studied in the framework of finite element (FE) analysis. FE-based constitutive models for arterial tissues are available, even in commercial codes such as Abaqus (SIMULIA, Providence, RI), and numerical modeling is a well-accepted means by which to gain insight into the functional relationships between structural and mechanical properties within arterial tissues, as well as studying tissue- and organ-level deformations or stresses [163]. Collagen fibers generally display wavy patterns in the unstressed arterial wall. When strain is applied it leads to a progressive recruitment of collagen fibers, which align themselves in preferred (principal) directions, causing the characteristic nonlinear mechanical response of arterial tissues. Higher strains effect the orientations of collagen fibers [204] resulting in an improved fiber orientation coherence and smaller dispersions of the entire fiber families [63, 139]. Anisotropic, fiber-reinforced material laws have been developed for modeling such tissues [56, 202], and some of these models also include a measure of the fiber dispersion, see, for example, [58, 122, 205, 206].

To visualize collagen one can make use of either stained histological sections (common stains: picrosirius red, hematoxylin and eosin, Masson's trichrome, Movat's pentachrome), or different microscopy techniques: for example, polarized microscopy [36, 139]; electron microscopy ([179] and references therein); fluorescence microscopy [207]; multiphoton microscopy (MPM) [46, 49, 50, 208], featuring enhanced penetration depth in soft biological tissues, good optical sectioning, and good resolution. Both, fluorescence microscopy and MPM, utilize collagen as a source of second harmonic generation (SHG) [48, 209, 210] and autofluorescence [43–45], which allows for direct observation without staining. For a brief overview of structural quantification of collagen fibers in arterial walls see [55].

To assess morphological collagen data from two-dimensional (2D) images in a simple, fast and automated fashion, we use a Fourier-based image analysis approach in combination with wedge filtering and progressive regions of interest (ROIs) splitting. Fourier power spectrum analysis and wedge filtering are both well established techniques for characterizing collagen organization based on the autocorrelation of intensity fluctuations within a given image [179, 180, 211–215]. ROI splitting is a tool for extracting morphological

data from sub-images, allowing us to assess changes of such data among varying length-scales.

Our approach differs from afore mentioned works, in that we focus on extracting relevant biomechanical material parameters which can be used directly in numerical modeling. We aim to provide an automated method to span the work of an experimentalist focused on obtaining high quality images from soft tissues, and a computational modeling of such tissues using material parameters extracted from 2D images. Specifically, we demonstrate the following: first, the accurate determination of the principal directions of fiber reinforcement (i.e. the preferred fiber directions), second the quantification of the fiber dispersion about this principal direction, third the gauging of appropriate length-scales for characterizing important features of the tissue morphology (which has implications on the FE mesh density of the geometrical model), and finally a comparison of the entire fiber distributions (instead of averaged measures) among different length-scales using higher-order statistics.

4.2 Methods and Materials

4.2.1 Images

To validate and demonstrate our methods in a controlled setting, we generated two binary test images, as shown in Fig. 4.1. Both test images are 1511×1511 pixels in size and contain 100 straight white lines, randomly distributed so that no two lines touch each other. The lengths of the lines vary according to a Gaussian distribution with a standard deviation of 35% of the mean length. In panel (a) all lines are aligned parallel at 25° (0° and 90° correspond to the horizontal and vertical axes of the image, respectively). In panel (b) 30% of the lines have been randomly rotated to yield a Gaussian distribution with a mean of 45° and a standard deviation of 10°. All random numbers were generated using MATLAB (MathWorks Inc., MA, USA).

Figure 4.2 gives an overview of three microscopy images we chose for our studies. Panel (a) shows a grayscale version of a representative micrograph of a picrosirius red (PSR) stained in-plane tissue section of the human intima (image size: 1936×1936 pixels) The use of autopsy material from human subjects for this study was approved by the Ethics Committee of Medical University Graz (#: 21-288 ex 09/10). We obtained the image via polarized microscopy through the course of a different research study; details regarding the tissue preparation and histological procedures can be found in [61]. The image features two almost symmetrically arranged collagen fiber families with respect to the main cylinder axes, indicated by the white dashed lines in panel (a). The circumferential and axial directions of the vessel correspond to 0° and 90°, respectively. Figure 4.2(b) shows a MPM image of one collagen fiber family taken from an in-plane section of the human media

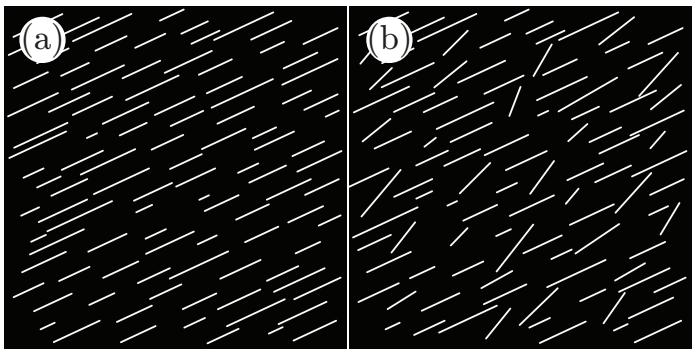

Figure 4.1: Two binary test images, each 1511×1511 pixels, containing 100 randomly distributed straight lines with varying lengths according to a Gaussian distribution (sd: 35%). In panel (a) all lines are oriented at 25° (0° is circumferential); in panel (b) 30% of the lines have been randomly rotated to match a Gaussian distribution with a mean of 45° and a standard deviation of 10°.

(image size: 1237×1237 pixels). The SHG signal of collagen was detected using a commercially available coherent anti-Stokes Raman scattering (CARS) and SHG microscope system based on a Leica SP5 (Leica Microsystems, Inc.). The device is equipped with a picosecond solid state laser-based light source (picoEmerald; APE, Germany; HighQ Laser, Austria) with integrated optical parametric oscillator (OPO). The SHG signal of collagen was generated by tuning the OPO to 830 nm. Backscattered SHG signal was collected in epi-mode using a non descanned detector (Epi-NDD) and a BP $465/170$ filter. Imaging was performed using a Leica HCX PL APO CS 40.0×0.25 oil objective. Figure 4.2(c) shows a SHG image of collagen fibers from a transversal section of chicken cartilage (image size: 1443×1443 pixels). For details regarding tissue preparation and imaging see [215].

4.2.2 Fourier transformation and wedge filtering

To obtain material parameters for applications in computational modeling, our first task is to extract quantitative data regarding collagen fiber orientations from 2D images. Toward this end, we represent the original grayscale image by a distribution function $f(x,y)$, where (x,y) defines a point in the real 2D image. Using a 2D Fast Fourier Transformation (FFT) we obtain $\mathcal{F}(f(x,y)) = F(u,v)$, where (u,v) is a point in the Fourier space. To avoid frequency-domain effects originating from periodic discontinuities at the boundaries of the original image, we first apply a window using a raised cosine function which reduces the grayscale values to 0 at the image periphery (see Fig. 4.3(a)). After FFT, we perform a coordinate shift, transforming the lowest spatial frequency to the origin, from where it increases as we move towards the image edges. The Fourier Transform (FT) is then multiplied with its complex conjugate F^*, yielding the power spectrum P, namely

$$P(u,v) = F(u,v) \cdot F^*(u,v). \tag{4.1}$$

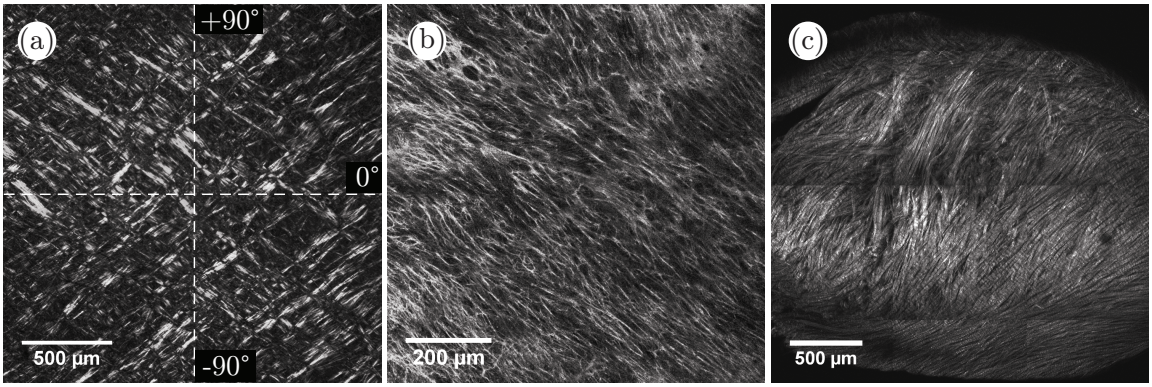

Figure 4.2: Representative experimental images: panel (a) displays an in-plane section of a human intima of the thoracic aorta (image size: 1936×1936 pixels), showing two collagen fiber families almost symmetrically arranged with respect to the major cylinder axes (indicated by the white dashed lines, 0° and 90° correspond to the circumferential and axial direction of the vessel, respectively); panel (b) shows an in-plane section of the human media (image size: 1237×1237 pixels) featuring one collagen fiber family; panel (c) shows collagen fibers in a transversal section of the chicken cartilage (image size: 1443×1443 pixels). The grayscale image in panel (a) was obtained using polarized light and picrosirius red staining. Images in panels (b) and (c) were obtained using second harmonic generation microscopes.

Figure 4.3(b) displays the Fourier power spectrum shown with a logarithmic intensity scale of the windowed image of Fig. 4.3(a). Note the 90° shift of the axes owing to the Fourier transformation. Frequency components of the collagen fibers along different orientations are represented as changes in amplitude, $I(\Phi)$, along a specific angle Φ. The two fiber families are visible as two white elongated clouds oriented between the major axes.

The collagen fibers are now discriminated by spatial frequency and orientation. We use wedge-shaped orientation filters to extract the fiber angles and their corresponding amplitudes from the power spectrum [211]. The amplitudes $I(\Phi)$ are obtained by summation of every $P(u,v)$ within individual wedges (1° wedge width), yielding a discrete distribution of relative amplitudes as a function of the angle Φ. For these angles to correlate with the real image, we shift them back by 90°, as shown in Fig. 4.3(c). For subsequent fitting, we smooth the relative amplitudes using a moving average filter with a span range of 5°. The effect of data smoothing is illustrated in Fig. 4.3(d).

4.2.3 Distribution fitting

To describe the angular distribution of fibers, say $\tilde{\rho}(\Phi)$, we use a π-periodic von Mises distribution similar to [122, 202], given by

$$\tilde{\rho}(\Phi) = \frac{\exp[b\cos(2(\Phi-\mu))]}{2\pi I_0(b)}, \tag{4.2}$$

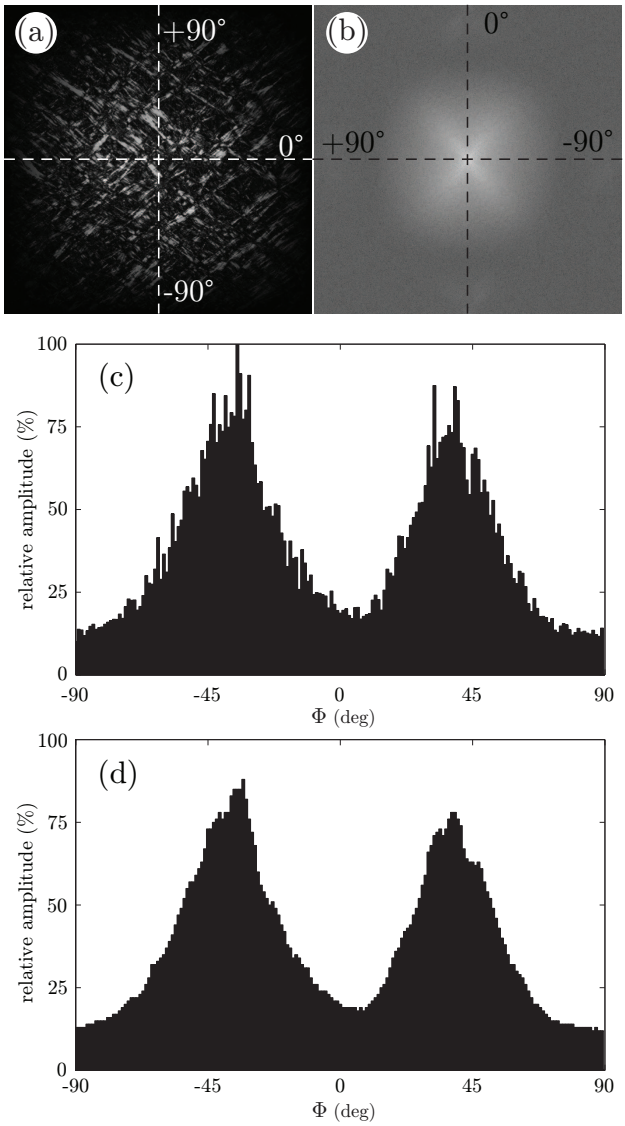

Figure 4.3: Panel (a) shows the windowed grayscale image of the intima, as shown in Fig. 4.2a. Panel (b) displays the Fourier power spectrum of (a), visualized with a logarithmic intensity scale and the lowest frequency at the origin. Panel (c) displays the discrete angular distribution of relative amplitudes $I(\Phi)$ of the windowed grayscale image, obtained through 1° wedge filtering of the power spectrum shown in (b). Panel (d) shows the effect of smoothing the amplitudes using a moving average filter with a span range of 5°. The frequency components in (a) of the collagen fibers along different orientations are represented in (b) as changes in amplitude along a specific angle Φ. Two fiber families are visible in (b) as two white elongated clouds oriented between the major axes. Note the 90° shift of the axes from (a) to (b) owing to the Fourier transformation. All angles in (c) are shifted back by 90° to correlate with the angles of the collagen fibers in the real image.

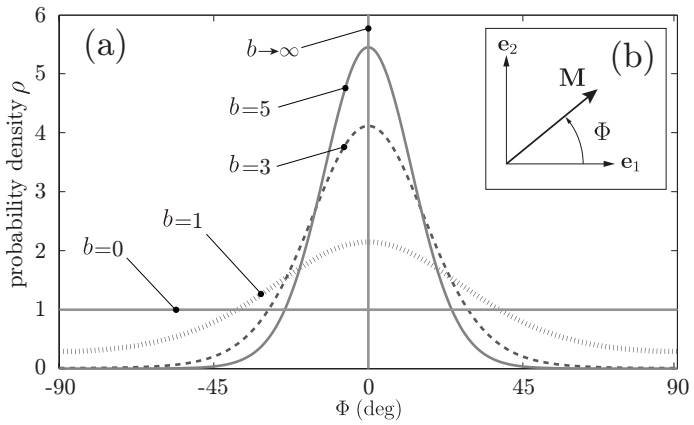

Figure 4.4: Panel (a) is a graphical representation of five two-dimensional von Mises distributions $\rho(\Phi)$ for five different concentration parameters. For $b = 0$, $\rho(\Phi) = 1$ is a uniform distribution (representing an isotropic fiber distribution) while for $b \to \infty$ the distribution becomes a Dirac delta function at angle μ (here centered at zero). Each distribution is normalized to π. Panel (b) shows the unit vector $\mathbf{M}$ defined by the angle Φ in a two-dimensional Cartesian coordinate system with the basis vectors $\mathbf{e}_1$ and $\mathbf{e}_2$.

where Φ denotes the angle, $b \in [0, \infty]$ the concentration parameter determining the shape of the distribution, and $\mu \in [-\pi/2, \pi/2)$ the location parameter describing the mean (or principal) fiber orientation (see Fig. 4.4(a)). Both parameters (b and μ) are determined during the fitting process. $I_0(b)$ in (4.2) is the modified Bessel function of the first kind of order zero and the function of order n is defined by

$$I_n(b) = \frac{1}{\pi} \int_0^{\pi} \exp[b\cos(\alpha)]\cos(n\alpha)\,\mathrm{d}\alpha. \tag{4.3}$$

Note that the von Mises distribution is an angular distribution and a close approximation to the wrapped normal distribution (which is the normal distribution wrapped around the circle) [216]. The von Mises distribution is normalized according to [202], such that

$$\frac{1}{\pi} \int_{-\pi/2}^{\pi/2} \rho(\Phi)\,\mathrm{d}\Phi = 1, \tag{4.4}$$

which yields the density function

$$\rho(\Phi) = \frac{\exp[b\cos(2(\Phi - \mu))]}{I_0(b)}. \tag{4.5}$$

Note that the location parameter μ becomes zero in the model since the x_1-axis of the coordinate system and the mean fiber direction are made to coincide (see Fig. 4.4(b)). From eq. (4.5) we can compute the dispersion parameter

$$\kappa = \frac{1}{\pi} \int_{-\pi/2}^{\pi/2} \rho(\Phi) \sin^2(\Phi)\, \mathrm{d}\Phi = \frac{1}{2}\left(1 - \frac{I_1(b)}{I_0(b)}\right), \tag{4.6}$$

with $\kappa \in [0, 1/2]$. For an isotropic fiber distribution $\kappa = 1/2$ ($b = 0$), in the case of complete fiber alignment, i.e. no dispersion, $\kappa \to 0$ ($b \to \infty$), as illustrated in Fig. 4.4(a).

We obtained an analytical solution for κ using the trigonometric identity $\sin^2 x = (1 - \cos 2x)/2$, yielding the result shown in (4.6). Since $\rho(\Phi)$ is π-periodic, (4.3) also holds for the integration limits $[-\pi/2, \pi/2]$. Note that κ is half of the circular variance [217]. The dispersion measure κ can be used to construct a symmetric structure tensor $\mathbf{H}$ which describes the fiber distribution in a continuum mechanical framework. Note that this approach assumes a planar, symmetric fiber distribution and is only appropriate for modeling thin lamellar structures or a subset of 3D problems under the assumption of an in-plane arrangement of the fibers (see discussion for more details).

To fit the distribution from Fig. 4.3(d), we use maximum likelihood estimation (MLE). The fundamental properties of the FT (see discussion) allow us to generate the fiber angle data set (required for MLE) from the amplitude distribution. For this purpose, we treat the distribution of relative amplitudes as a histogram, where the number of fiber angles equates to the value of the corresponding amplitude. For instance, from a relative amplitude value of 20% at 0° we generate 20 angles with 0°. This approach ensures that the created angular data set can reproduce the original amplitude distribution and provides us with a sufficient number of angles for the MLE.

As can be seen in Fig. 4.3(d), the distribution is composed of two fiber families, with a summation of the amplitudes at the overlapping region. Therefore, we use a mixture of two von Mises distributions, given by

$$\rho_{\mathrm{mix}}(\Phi) = \rho_1(\Phi) + \rho_2(\Phi) = \sum_{i=1}^{2} \frac{\exp[b_i \cos(2(\Phi - \mu_i))]}{I_0(b_i)}. \tag{4.7}$$

Thus, four parameters are fitted, namely the concentration parameters b_1 and b_2 and the location parameters μ_1 and μ_2 of the two distinct distributions. Note that the mixture of the two von Mises distributions in (4.7) does not need to be normalized to π by a constant factor, since it is only used in the fitting process for determining the four fitting parameters [218], and is not used further in the model.

4.2.4 Varying length-scale analysis

To determine meaningful measures of fiber orientations at different length-scales, we divide the original image continuously into ever smaller sub-images, denoted as regions-of-interest (ROIs). With each subsequent dividing step n, the number of ROIs grows exponentially by n^2, as illustrated for $n = 1$-4 in Fig. 4.5(a). Every ROI is windowed (see above) and the Fourier power spectrum is calculated according to (4.1). We then fit a line through the center of the power spectrum in a least squares sense [179], from which the overall fiber angle φ is determined for each ROI (Fig. 4.5(b)). Note that φ could also be determined by means of wedge filtering, but since we are only interested in one parameter for each ROI (instead of the entire angular distribution of amplitudes for each ROI) it is computationally (much) more efficient to fit a line through the power spectrum. This yields n^2 angles φ within the original image for each dividing step n, illustrated in Fig. 4.5(c) as a histogram for $n = 30$ (0° and 90° correspond to the horizontal and vertical direction of the image, respectively). From this angular distribution we determine two measures describing the average behavior of the calculated fiber orientations: the mean angle $\overline{\varphi}_{\mathrm{m}}$ and the median angle $\overline{\varphi}_{\mathrm{mdn}}$. We provide both measures in the illustrative example ($n = 30$) in Fig. 4.5(c). Normalizing the histogram to $\sum_{i=1}^{n^2} I(\varphi_i) = 1$ yields the computed probability mass function (PMF) $p_{\mathrm{c}}(\varphi)$, which we use in the subsequent analysis. Using both $\overline{\varphi}_{\mathrm{m}}$ and $\overline{\varphi}_{\mathrm{mdn}}$, we aim to determine an appropriate range for n, where the resulting distribution of n^2 fiber angles $\varphi_i\,(i = 1, n^2)$ reflects the inhomogeneous morphology of the collagen fibers in the image. We achieved this goal by determining a range where $\overline{\varphi}_{\mathrm{m}}$ and $\overline{\varphi}_{\mathrm{mdn}}$ display (relatively) stable behavior among subsequent partitions (n's).

To test if the calculated distributions from dividing images into ROIs reflect the inhomogeneity of the morphology, we plot statistical measures across different subdivisions (i.e. different n's) of images. In this context, the weighted error entropy is the most relevant statistical measure [219, 220]. Error entropy has been used in the context of stochastic learning as a reliable metric, and has the ability to capture arbitrary statistics [221]. The error entropy E is defined as

$$E(n) = \frac{1}{\pi} \sum_{i=-\pi/2}^{\pi/2} p_{\mathrm{d}}(\varphi_i, n) \log_2[p_{\mathrm{d}}(\varphi_i, n)], \tag{4.8}$$

where

$$p_{\mathrm{d}}(\varphi_i) = \mathrm{abs}[p_{\mathrm{c}}(\varphi_i) - p_{\mathrm{a}}(\varphi_i)]. \tag{4.9}$$

While p_{d} quantifies the difference between the computed (p_{c}) and actual (p_{a}) PMF, the error entropy $E(n)$ quantifies the uncertainty in the difference between the two distributions.

Hence, when the two distributions are identical, the error entropy is zero. However, this assumes that both distributions p_{c} and p_{a} are centered around the same value (a difference

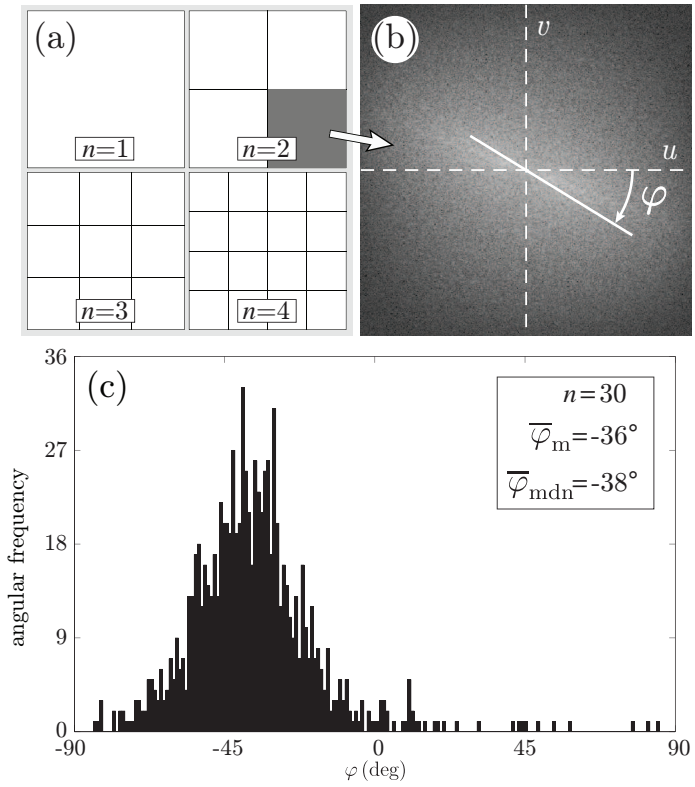

Figure 4.5: Schematic of the steps to determine collagen fiber distributions at decreasing length-scales (increasing dividing steps n). The original image (panel (a), $n = 1$) is continuously divided into an increasing number of regions-of-interest (ROIs), yielding n^2 ROIs at each step n, as illustrated for $n = 1$-4 in (a). For every ROI, the Fourier power spectrum is calculated, from which the overall fiber angle φ of this ROI is determined by fitting a line through the center of the power spectrum in a least squares sense, as shown in (b). Panel (c) is a representative histogram of all angles for $n = 30$, yielding the angular distribution (900 angles) of the original image from Fig. 4.2(b) at this length-scale (0° corresponds to the horizontal direction of the image). Normalizing the histogram by $\sum_{i=1}^{n^2} I(\varphi_i) = 1$ yields the computed probability mass function (PMF) $p_c(\varphi)$. To describe the average behavior of this distribution, the mean angle $\overline{\varphi}_m$ and the median angle $\overline{\varphi}_{mdn}$ are determined.

distribution which is Dirac delta at a different mean value has less error entropy than a difference distribution which is centered around the correct mean). To prevent this occurrence, we weight the error entropy with difference in mean values. The weighted error entropy is given by

$$E_w(n) = \text{abs}[\mu_{p_c}(n) - \mu_{p_a}(n)][k + E(n)], \tag{4.10}$$

where k is a weighing constant and μ_{p_c} and μ_{p_a} are the mean values of the given distributions. In order to determine the weighted error entropy, the actual PMF (p_a in equation (4.9)) must be computed if it is not known. For the first two test images (Figs 4.1(a) and (b)), p_a is the input PMF (the normalized angular distribution of the lines). Because p_a is usually unknown for experimental images (for example, Figs 4.2(b) and 4.2(c)), we

choose a specific PMF to be p_{a}, where the gradient of absolute entropy of the PMF stabilizes and reaches a plateau. To ensure that the chosen p_{a} is robust, we perform a perturbation analysis. If n yields the ROI size when the gradient of absolute entropy stabilizes, we also choose theoretical distributions corresponding to $(n-3)$ and $(n+3)$. A robust choice would imply that our results (the plots of weighted error entropy E_{w}) do not change for such small perturbations in the chosen theoretical PDF p_{a}.

4.3 Results

We have developed automated methods to extract collagen fiber orientations and associated dispersions at different length-scales from 2D images, which can then be used in computational modeling. To this end, we focused on three key parameters: first, the dispersion parameter κ, which is a well established and used measure of anisotropy [122, 202, 206]; second, the fiber angles $\overline{\varphi}_{\mathrm{m}}$ and $\overline{\varphi}_{\mathrm{mdn}}$, as a measure for the average orientation of a given fiber distribution; third, the weighted error entropy E_{w}, which analyzes and compares entire fiber distributions rather than the averaged fiber orientations, which is, therefore, useful when average measures are not sufficient. Furthermore, the behavior of the average fiber angles and weighted error entropy at different length-scales allows us to determine an appropriate range of ROI sizes, which will yield fiber distributions representing the tissue morphology from the image, which has implications for computational modeling (for example, on the mesh density). Our method is based on transforming an image to Fourier space where the power spectrum is calculated, from which the above mentioned parameters can be extracted (see Figs 4.3 and 4.5).

4.3.1 Distribution fitting

To obtain the dispersion parameter κ, we fit a given angular distribution using MLE. As an illustrative example we choose the (more challenging) case of an image featuring two (rather than one) collagen fiber families (Fig. 4.2(a)). The result of fitting a mixture of two von Mises distributions (equation (4.7)) is shown in Fig. 4.6. The fitting parameters are $b_1 = 2.503, \mu_1 = -39.6^\circ$ and $b_2 = 2.149, \mu_2 = 39.4^\circ$ for the two distributions, respectively (b denotes the concentration parameter and μ the location parameter). Using (4.6) and the shape parameters b_1 and b_2, the dispersion parameters $\kappa_1 = 0.1173$ and $\kappa_2 = 0.1396$ were calculated. To quantify the goodness of the fit, we use the Pearson χ^2 test (yielding a p-value) and the coefficient of determination R^2. For the fit in Fig. 4.6 we obtained $p = 0.8535$ and $R^2 = 0.935$.

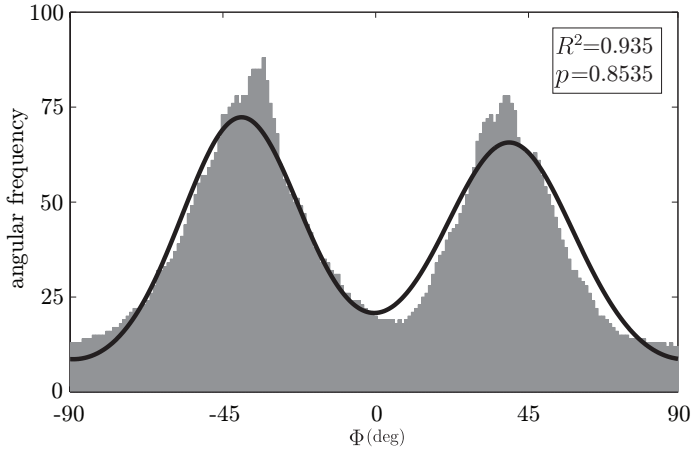

Figure 4.6: Angular distribution of the collagen fibers in Fig. 4.2(a) (0° corresponds to the circumferential direction of the vessel). The two distinct peaks correspond to the two collagen fiber families, almost symmetrically arranged around the circumferential direction, visible in Fig. 4.2(a). The fit was performed using maximum likelihood estimation and two superimposed von Mises distributions with four fitting parameters: one concentration and location parameter for each fiber family ($b_1 = 2.503$, $\mu_1 = -39.6°$, $b_2 = 2.149$, $\mu_2 = 39.4°$). The dispersion parameters for each family are $\kappa_1 = 0.1173$, $\kappa_2 = 0.1396$.

4.3.2 Varying length-scale analysis

Figure 4.7(a) shows the behavior of the average fiber angles $\overline{\varphi}_{\mathrm{m}}$ and $\overline{\varphi}_{\mathrm{mdn}}$ with increasing $n \in [0,75]$ (decreasing ROI size) for the first test image from Fig. 4.1(a). Initially, both measures yield the correct angle of 25° in accordance with the actual input PMF (p_{a}), which is a Dirac delta distribution located at 25° (see Fig. 4.1(a)). The mean angle starts to deviate from the correct angle around $n = 13$ (left arrow in Fig. 4.7(a)) marking the upper cut-off point for $\overline{\varphi}_{\mathrm{m}}$, while the median angle shows a more stable behavior yielding the appropriate angle $(\pm 0.5°)$ until the upper cut-off point for $\overline{\varphi}_{\mathrm{mdn}}$ around $n = 36$ (right arrow).

For the weighted error entropy (E_{w}) in Fig. 4.7(b), p_{a} was chosen to be a Dirac delta distribution located at 25°, corresponding to the actual PMF of the first test image. Note that if instead of the Dirac delta distribution we choose p_{a}, based on the results of the perturbation analysis (not plotted), where the gradient of absolute entropy stabilizes (rather than the known Dirac delta distribution), it results in the theoretical distribution, verifying our scheme for computing the unknown actual PMFs for images of soft tissues. The weighted error entropy is quite stable until around $n = 13$. While the reliable estimate for the median holds until $n = 36$ (upper cut-off point for $\overline{\varphi}_{\mathrm{mdn}}$ in (a)), the entire PMF only shows a relatively stable behavior for a third of that range (until $n = 13$), similar to $\overline{\varphi}_{\mathrm{m}}$.

The results in Fig. 4.8(a) for $\overline{\varphi}_{\mathrm{m}}$ and $\overline{\varphi}_{\mathrm{mdn}}$ of the second test image, which includes some

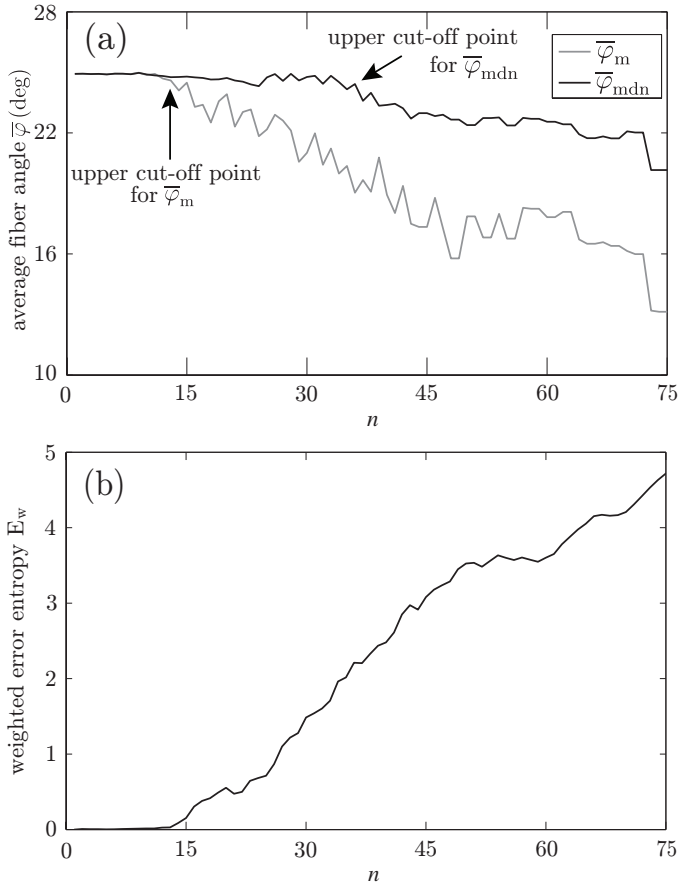

Figure 4.7: Results for the first test image (Fig. 4.1(a)): panel (a) shows the mean angle $\overline{\varphi}_{\mathrm{m}}$ and the median angle $\overline{\varphi}_{\mathrm{mdn}}$ for increasing dividing steps n, and panel (b) shows the weighted error entropy E_{w}. Both measures $\overline{\varphi}_{\mathrm{m}}$ and $\overline{\varphi}_{\mathrm{mdn}}$ in (a) yield the correct angle of 25° until around $n = 12$, confirming the capability of this method for extracting accurate angular data across different length-scales. The mean angle $\overline{\varphi}_{\mathrm{m}}$ starts to loose accuracy around $n = 13$ (upper cut-off point for $\overline{\varphi}_{\mathrm{m}}$), while the median angle is more stable $(\pm 0.5^{\circ})$ up to $n = 36$ (upper cut-off point for $\overline{\varphi}_{\mathrm{mdn}}$). The weighted error entropy in panel (b), is relatively stable until around $n = 13$, corresponding to only minor changes in the probability mass functions (PMFs) across these length-scales.

dispersion (see Fig. 4.1(b)), show a very different behavior with respect to the first test image. Initially the mean angle $\overline{\varphi}_{\mathrm{m}}$ yields increased values around 30° (owing to the fact that 30% of the fiber angles are distributed with a mean of 45°) and starts to drift off at $n = 17$. Overall, the values for $\overline{\varphi}_{\mathrm{m}}$ fluctuate with increasing n, and a stable behavior is never observed. The median angle $\overline{\varphi}_{\mathrm{mdn}}$ on the other hand only fluctuates in the beginning of the analysis (n = 1-10), and stabilizes at a lower cut-off point of about $n = 11$ (see arrow); $\overline{\varphi}_{\mathrm{mdn}}$ is then stable up to $n = 24$ ($\pm 0.5^{\circ}$) before it starts to drift away. The weighted error entropy in Fig. 4.8(b) indicates that after an initial increase the PMFs do not change much until $n = 14$, after which $E_{\mathrm{w}}(n)$ shows a steeper increase.

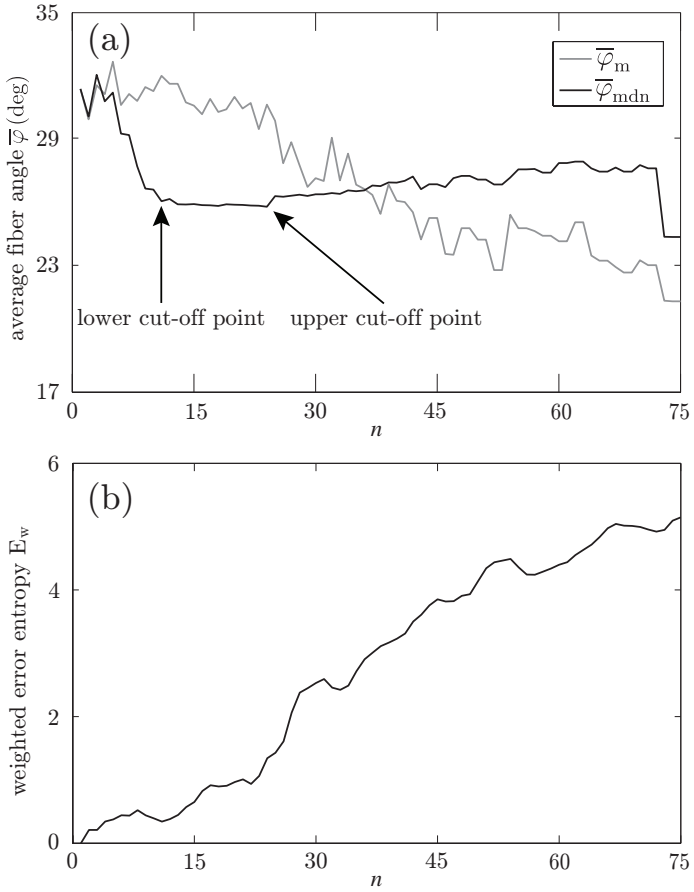

Figure 4.8: Results for the second test image which includes dispersion (Fig. 4.1(b)): panel (a) shows the mean angle $\overline{\varphi}_{\mathrm{m}}$ and the median angle $\overline{\varphi}_{\mathrm{mdn}}$ for increasing dividing steps n, and panel (b) shows the weighted error entropy E_{w}. In (a) the mean angle $\overline{\varphi}_{\mathrm{m}}$ fluctuates and does not stabilize owing to the dispersion, and is, therefore, not suited for identifying a range of appropriate ROI sizes. On the other hand, the median angle $\overline{\varphi}_{\mathrm{mdn}}$ initially fluctuates but stabilizes around $n = 11$, yielding a lower cut-off point (left arrow); $\overline{\varphi}_{\mathrm{mdn}}$ is then stable up to $n = 24$ (upper cut-off point) before it starts to drift away. In the stable range of $\overline{\varphi}_{\mathrm{mdn}}$ from $n = 11$ to $n = 24$, the n^2 angles from all ROIs yield an angular distribution representing the orientation of lines in the input image. The weighted error entropy E_{w} in (b) shows that after an initial increase the PMFs do not change much until $n = 14$.

Figure 4.9 displays the results of the average fiber angles in panel (a), and the weighted error entropy in panel (b) of a SHG image featuring collagen fibers in an in-plane section of the human media (shown in Fig. 4.2(b)).

Both $\overline{\varphi}_{\mathrm{m}}$ and $\overline{\varphi}_{\mathrm{mdn}}$ have a lower cut-off point at $n = 3$. After $n = 19$, $\overline{\varphi}_{\mathrm{m}}$ drifts away sharply, while $\overline{\varphi}_{\mathrm{mdn}}$ displays a (relatively) stable range until the upper cut-off point at approximately $n = 40$. The weighted error entropy curve features two regimes: (i) a very

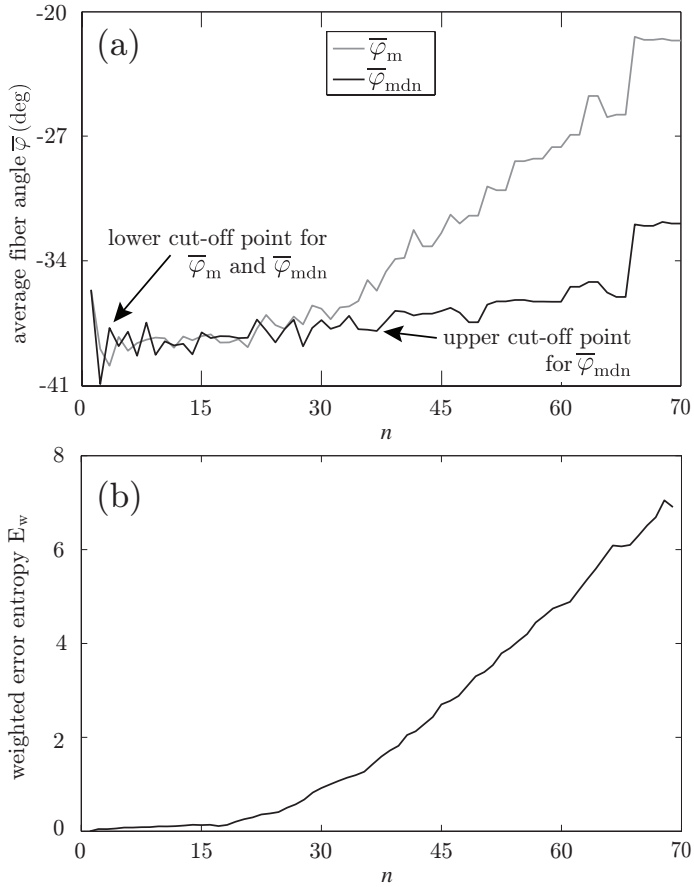

Figure 4.9: Results for the second harmonic generation image of collagen fibers in the human media (Fig. 4.2(b)): panel (a) shows the mean angle $\overline{\varphi}_{\mathrm{m}}$ and the median angle $\overline{\varphi}_{\mathrm{mdn}}$ for increasing dividing steps n, and panel (b) shows the weighted error entropy E_{w}. In (a) we observe a lower cut-off point for both angles $\overline{\varphi}_{\mathrm{m}}$ and $\overline{\varphi}_{\mathrm{mdn}}$ at $n = 3$. While $\overline{\varphi}_{\mathrm{m}}$ starts to drift away after $n = 19$, the median angle $\overline{\varphi}_{\mathrm{mdn}}$ displays a (relatively) stable behavior over a wider n-range until about $n = 40$, followed by a small angular drift at decreasing ROI sizes. The weighted error entropy E_{w} in panel (b) displays small changes of the probability mass functions (PMFs) up to $n = 18$. The entropy increase beyond that point coincides to the length-scale where the stable region for $\overline{\varphi}_{\mathrm{m}}$ in (a) starts to break down.

stable region until $n = 18$, and (ii) a monotonic, almost linear increase henceforth. This is similar to the drift in the curve for $\overline{\varphi}_{\mathrm{m}}$, while the drift is less steep for $\overline{\varphi}_{\mathrm{mdn}}$.

The results from the analysis of the SHG image featuring collagen fibers of the chicken cartilage (shown in Fig. 4.2(c)) are displayed in Fig. 4.10. Both, $\overline{\varphi}_{\mathrm{m}}$ and $\overline{\varphi}_{\mathrm{mdn}}$ in panel (a) have a lower cut-off point at $n = 4$, followed by a stable domain until the upper cut-off point at $n = 25$. In the stable domain, $\overline{\varphi}_{\mathrm{m}}$ yields values approximately 6° higher compared to $\overline{\varphi}_{\mathrm{mdn}}$. The weighted error entropy in Fig. 4.10(b) has a trend similar to Fig. 4.9(b), with a stable regime followed by an almost linearly increasing curve. In the beginning of

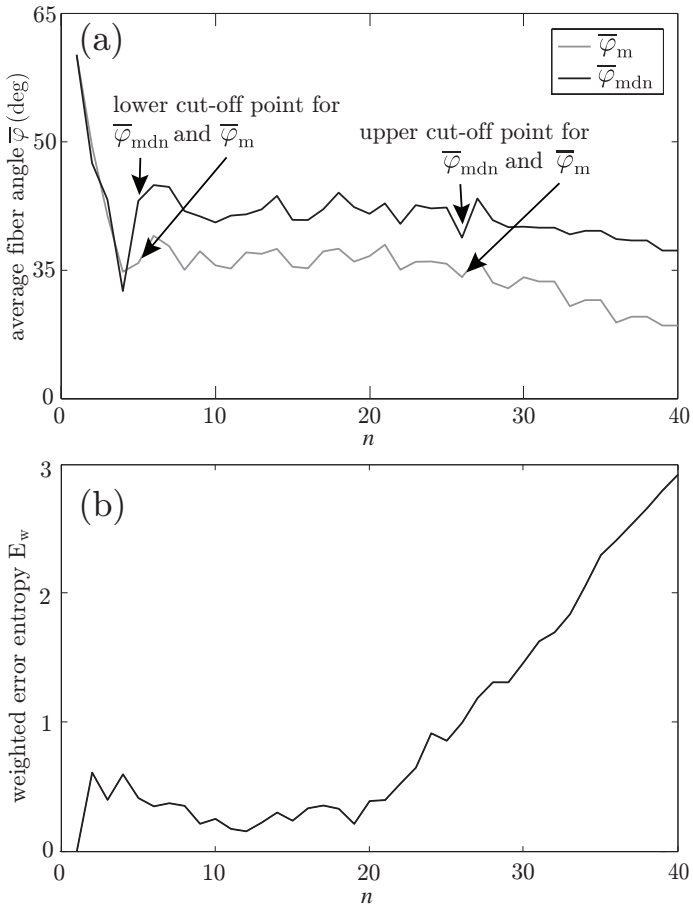

Figure 4.10: Results for the second harmonic generation image of collagen fibers of chicken cartilage (Fig. 4.2(c)): panel (a) shows the mean angle $\overline{\varphi}_{\mathrm{m}}$ and the median angle $\overline{\varphi}_{\mathrm{mdn}}$ for increasing dividing steps n, and panel (b) shows the weighted error entropy E_{w}. In (a) we observe a lower cut-off point for both angles $\overline{\varphi}_{\mathrm{m}}$ and $\overline{\varphi}_{\mathrm{mdn}}$ at $n = 4$, below which both measures yield unstable values owing to artifacts and different collagen fiber orientations at the perimeter of the cartilage. Both measures show a stable behavior up to $n = 25$ (upper cut-off point), though the values for $\overline{\varphi}_{\mathrm{m}}$ are approximately 6° higher compared to $\overline{\varphi}_{\mathrm{mdn}}$. The behavior of the weighted error entropy E_{w} up to around $n = 6$ in (b) confirms the existence of an initially unstable domain (highlighted in (a)), followed by a stable and low weighted error entropy regime up to about $n = 21$.

Fig. 4.10(b), up to around $n = 6$, E_{w} reveals changes in the PMF owing to afore mentioned artifacts. This is not the case for E_{w} in Fig. 4.9(b), because the analyzed image (shown in Fig. 4.2(b)) does not contain regions with very different fiber orientations (compare Fig. 4.2(b) with Fig. 4.2(c)).

4.4 Discussion

In this paper we outline an automated Fourier-based imaging analysis method to extract and quantify material parameters characterizing collagen fiber orientations from 2D images. Our method combines Fourier power spectrum analysis and wedge filtering (two well-established image analysis tools for morphological data extraction, see, for example, [179, 180, 211]). Additionally, we show how ROIs (sub-images) can be utilized to obtain useful orientation information among different length-scales.

We aim to extract data from which we can (i) determine material parameters for computational modeling of soft biological tissues using fiber reinforced constitutive models and, (ii) gauge which length-scales are most appropriate to capture tissue morphology, which can also have implications for computational modeling (for example, mesh density). Specifically, we focus on three key parameters: first, we compute the dispersion parameter κ, a measure of anisotropy [122, 202, 206]. Mainly, κ is based on a three-dimensional (3D), rotationally symmetric von Mises distribution. Since we deal with 2D images, we make use of the 2D equivalent as discussed in [202]. Second, we introduce two measures for the average orientation of a given distribution $(\overline{\varphi}_{\mathrm{m}}, \overline{\varphi}_{\mathrm{mdn}})$ and show that $\overline{\varphi}_{\mathrm{mdn}}$ is the more appropriate measure to use if the collagen fibers are dispersed. In the presence of fiber families the average orientation corresponds to the preferred (or principal) fiber direction of one fiber family [61], and hence can be used as a parameter for continuum mechanics-based constitutive models (see, for example, [56, 107, 120, 136, 222] and references therein). Third, we calculate the weighted error entropy E_{w} as a measure of changes in the entire fiber distributions at different length-scales, as opposed to their average behavior.

4.4.1 Analysis validation

In our approach, three fundamental properties of the FT are pertinent, ensuring that the distribution of relative amplitudes in the Fourier space is a representation of the collagen fiber distribution. They are: (i) the rotation of a collagen fiber results in an equal rotation in the Fourier space (*the rotational property*), (ii) the Fourier transform of a region containing several fibers is equal to the sum of the individual Fourier transforms of the same fibers (*the addition theorem*), and (iii) a spatial shift of a fiber does not affect the amplitude of its Fourier transform (*the shift theorem*). Hence, Fourier space provides a proper representation of the fiber orientations of a 2D image.

Generally, the dimensions of any original image used for our analysis should be much larger than the structures of interest shown in the image (in our case collagen fibers) to ensure that they can still be contained within ROIs at increasingly smaller length scales. To validate the functionality of our method we created two test images shown in Figs 4.1(a) and (b). The purpose of the first test image (panel (a)) is to verify the capability of the

method to extract correct angular data among various length-scales. The distribution of all lines in the first test image corresponds to a Dirac delta function at 25°. Both average measures ($\overline{\varphi}_{\mathrm{m}}$, $\overline{\varphi}_{\mathrm{mdn}}$) yield the correct angles of 25° in the range of $n = 1$-12 (see Fig. 4.7(a)). As expected, $\overline{\varphi}_{\mathrm{mdn}}$ is more stable at increasingly smaller ROI sizes (increasing n) than $\overline{\varphi}_{\mathrm{m}}$.

To investigate which of the two average measures is more appropriate if the fibers are dispersed, we modified the first test image to include some dispersion, resulting in the second test image shown in Fig. 4.1(b). From the results in Fig. 4.8(a) it becomes evident that the mean average measure $\overline{\varphi}_{\mathrm{m}}$ does not stabilize. It is, therefore, not suited for identifying a range of ROI sizes that would yield angular distributions which are representative for the orientations of the lines (simulated fibers). On the other hand, the behavior of the median average measure $\overline{\varphi}_{\mathrm{mdn}}$ shows three interesting characteristics: (i) it yields a lower cut-off point, which represents a maximum ROI size above which the average angles $\overline{\varphi}_{\mathrm{mdn}}$ of the entire distributions fluctuate highly as n changes; (ii) it yields an upper cut-off point, which marks a minimum ROI size below which the angular values start to drift away; and (iii) it identifies a stable range of ROI sizes between both cut-off points. Such stable ranges can only be observed if the underlying distributions (from which $\overline{\varphi}_{\mathrm{mdn}}$ is determined) reflect the orientations of the features in the image. If, for example, a ROI size is too large, details within individual ROIs are smeared out and information is lost. On the other hand, if a ROI size is too small the information within individual ROIs is compromised by, for example, image artifacts, resolution limits or edge effects.

4.4.2 Distribution fitting

We use MLE to fit a mixture of two von Mises distributions to the angular distribution obtained from the image in Fig. 4.2(a), featuring two collagen fiber families in the human intima of the thoracic aorta [61]. The results of this fitting are shown in Fig. 4.6, and as a measure of the goodness-of-fit we determined the p and R^2 values. Since the Pearson χ^2-test depends on the size of the data set (i.e. the number of generated angles), we also calculate the coefficient of determination R^2. Since R^2 is computed by comparing the original distribution with the estimated PDF, it does not depend on the number of angles and is, therefore, an additional measure for the goodness-of-fit independent of p. We also emphasize that R^2 is not optimized during the fitting procedure.

We would like to note that although it is quite common to fit a curve to a histogram using the least squares method, there are some drawbacks to this approach that should be kept in mind. For one, least squares fitting depends on the bin size of the histogram. Another potential pitfall arises from the *normality assumption*, which states that the errors are normally distributed with mean zero. Since bin counts in a histogram are non-negative this assumption does not hold. Also the *constant variance assumption* and the *independent-errors assumption* are not justified when fitting distributions [223].

4.4.3 Fiber angles and dispersion

In the literature, the importance of collagen fiber orientations on the mechanical behavior of arterial walls has been well established, see, for example, [55, 61, 140, 202]. To account for the effect of strain on changes in the fiber orientations and the angular distributions, to approximate the *in vivo* strain state of arteries as well as to ensure more straightened fibers necessary for angular measurements, the investigated samples were usually either pressurized or pre-stretched biaxially beforehand [125, 137–139]. Our approach allows for a fast and automated determination of the angular distribution from 2D images. By fitting a given distribution (in our example a distribution of two fiber families, see Figs 4.2(a) and 4.3) with a mixture of two von Mises distributions, we can compute the principal fiber orientations μ_1, μ_2, and the corresponding dispersion parameters κ_1, κ_2, one for each fiber family (see Fig. 4.6).

Note that this approach assumes a planar, symmetric fiber dispersion for each fiber family individually. Such 2D data can be directly applied to mechanical modeling of thin lamellar tissue structures on the basis of membrane or thin shell theory, for example, cerebral arteries, using appropriate constitutive models (see, for example, [122, 202] for further discussion). However, many arteries behave as thick-walled cylindrical tubes, for example, the human aorta, and hence 3D modeling approaches are required. In this case, for a subset of fully 3D problems, one can make use of the (mainly) in-plane arrangement of the collagen fibers in arterial walls. For example, in the case of the human descending aorta and common iliac arteries, the collagen fibers lie in the plane of the tissue (angular deviation $\approx \pm 9^\circ$) [61]. The assumption of in-plane arranged collagen fibers is not necessarily appropriate for other soft tissues. For example, in the articular cartilage the fibers display very different orientations depending on the specific zone. In the tangential zone they lie within the transversal plane, a variety of orientations are observed for the middle zone, while in the deep zone the fiber arrangement is perpendicular to the transversal plane [224]. To ensure that our analysis yields correct material parameters, most of the collagen fibers should lie within the sectioning (imaging) plane in order to avoid projections to this plane, which would lead to deviations in length and (possibly) angles from the true morphological state. Therefore, in the case of an in-plane arrangement of the collagen fibers the 2D collagen fiber data obtained through our method may also be used for 3D modeling (using the 2D κ parameter according to equation (4.6)) under the assumption of strictly in-plane organized collagen fibers (neglecting the out-of-plane deviations is a simplification of the problem with regards to computational modeling, motivated by experimental observations [61]).

4.4.4 Varying length-scale analysis

We developed an analysis method which continuously splits an image into increasingly smaller ROIs to obtain a physically meaningful measure of fiber orientations across length-scales. In most applications, mean and median measures suffice when we are interested in the average behavior of fiber families. Using two test images we have shown that the median angle $\overline{\varphi}_{\text{mdn}}$ is the more appropriate measure to use for this purpose.

To demonstrate the applicability and usefulness of our method on microscopy images of soft tissues containing collagen fibers, we ran our analysis on SHG images of the human media and the chicken cartilage (see Figs 4.2(b) and (c), respectively). Results for both images, as shown in Figs 4.9(a) and 4.10(a), reveal a stable range of ROI sizes, located between the lower and upper cut-off point, where $\overline{\varphi}_{\text{mdn}}$ shows only small fluctuations ($\pm 3^{\circ}$). The advantage of the length-scale analysis can be seen in Fig. 4.10(a), where a ROI size in the range of $n = 1$-4 leads to highly fluctuating values for $\overline{\varphi}_{\text{mdn}}$, followed by a wide range $(n = 5\text{-}25)$ of stable behavior before $\overline{\varphi}_{\text{mdn}}$ slowly drifts away. Using our method, a finite element analyst can, for example, determine an appropriate mesh density (based on a ROI size where $\overline{\varphi}_{\text{mdn}}$ shows stable behavior) which also captures the relevant tissue structure. For example, the cartilage tissue in Fig. 4.2(c) features very different fiber orientations at the perimeter compared to the center of the tissue. If a ROI size is too large, this specific tissue inhomogeneity will be lost. Only if the ROI size is small enough, can such spatial changes in orientation be resolved. Analysis of the cartilage tissue shown in Fig. 4.10(a) tells us, that a mesh density corresponding to a ROI size between $n = 5$-25 is appropriate to capture important structural features of the image.

However, if average measures are not sufficient (for example, quantification of the risk of a pathological condition such as an abdominal aortic aneurysm [225]), and to depict how higher-order statistical measures vary across different values for n, we compare weighted error entropies across different values n. There are different measures which can be used to compute the distance between two distributions [226–228]. For example, the Kullback-Leibler divergence [229] is a measure of distance between two distributions, but it is not symmetric and is only defined for two distributions whose range of non-zero values is the same (which is not the case in our examples). Mutual information, as another example, quantifies how much the knowledge of one variable reveals about another variable. However, correlation information between the two variables is needed, and such information is not available in our case. The weighted error entropy E_{w} is an appropriate measure for our purpose. It compares entire fiber distributions (rather than the averaged behavior) and reveals, how much of the tail information is lost when averaged behavior is considered. For the microscopy images in our study, the weighted error entropy shows that the entire fiber distributions start to change with increasing n before a change in $\overline{\varphi}_{\text{mdn}}$ can be observed (cf. panels (a) and (b) in both Figs 4.9 and 4.10). Therefore, if one is interested in the behavior of the entire fiber distributions, a study of E_{w} helps to identify ranges of n where

calculated fiber distributions are similar, and at which length-scale they start to differ.

The usefulness of both parameters $\overline{\varphi}_{\mathrm{mdn}}$ and E_{w} is illustrated in the results for the second test image (Fig. 4.1(b)) in Fig. 4.8. For example, if one is interested in determining an appropriate ROI size capturing local changes in tissue morphology, then a corresponding ROI size ranging from $n = 11$-20 is suitable, since in this range $\overline{\varphi}_{\mathrm{mdn}}$ shows a (relatively) stable behavior. On the other hand, if the behavior of the entire PMF is of interest, then the result for E_{w} tells us that we are loosing information starting around $n = 14$, which is insight that can not be gained from average measures.

Another valuable aspect of our methods pertains inhomogeneous computational modeling of tissues. For this purpose the location-specific structural parameters (fiber angle κ) obtained for every ROI can be incorporated element-wise into a FE mesh. Such patient-specific data allows for a more precise modeling of the cardiovascular system and could help improve our understanding of the interaction between collagen fiber morphology and arterial wall mechanics.

Limitations. The method we present extracts morphological data from 2D images and is, therefore, not able to capture true 3D fiber orientations and dispersions. As it is the case with other methods which aim to quantify fiber angles, it is a prerequisite for the collagen fibers to be (mostly) straightened (see [61] and references therein). Such data can be used for modeling within the framework of membrane or thin shell theory, but are limited to a subset of 3D physical problems and soft biological tissues (see discussion). To fit the fiber distribution we use MLE which requires a sufficient number of fiber angles. Our method does not measure fiber angles directly, but extracts them from Fourier power spectra. While this automated approach for extracting orientational information from images is well established, we want to emphasize that the resulting fiber angle distributions do not represent accurate fiber angle counts. The choice for the upper and lower cut-off points to determine a (relatively) stable dividing range (n range), with the aim of obtaining physically meaningful fiber orientations which reflect the tissue morphology, must be made manually. Depending on the input image this choice can either be very evident or in the case of slow drifts with increasing n-values less defined.

Acknowledgement. This work was partly supported by the European Commission under the 7th Framework Programme in the scope of the project SCATh – Smart Catheterization, Grant Agreement Number 248782, and by an AHA postdoctoral fellowship grant to S. Sankaran, University of California, USA. We also thank Dr. Heimo Wolinski, University of Graz, Austria, and Dr. Magnus B. Lilledahl, Norwegian University of Science and Technology, Norway, for generously providing us with MPM images, i.e. Figs. 4.2(b) and 4.2(c).

5 3D QUANTIFICATION OF FIBRILLAR STRUCTURES IN OPTICALLY CLEARED TISSUES

Abstract. We present a novel approach allowing for a simple, fast and automated morphological analysis of 3D image stacks (*z*-stacks) featuring fibrillar structures from optically-cleared soft biological tissues. Five non-atherosclerotic tissue samples from human abdominal aortas were used to outline the multi-purpose methodology, applicable to various tissue types. It yields a 3D orientational distribution of relative amplitudes, representing the original collagen fiber morphology, identifies regions of isotropy where no preferred fiber orientations are observed, and determines structural parameters throughout anisotropic regions for the analysis and numerical modeling of biomechanical quantities such as stress and strain. Our method combines optical tissue clearing with second-harmonic generation imaging, Fourier-based image analysis, and maximum likelihood estimation for distribution fitting. With a new sample preparation method for arteries, we present for the first time a continuous 3D distribution of collagen fibers throughout the entire thickness of the aortic wall, revealing novel structural and organizational insights into the three arterial layers.

5.1 Introduction

The importance of fibrillar collagen in arterial tissue has long been known [22, 63]. It is not only mechanically the most important tissue constituent [55, 56], but research indicates that it also plays an important role in arterial disease and degeneration [69, 126] as well as in the healing of dissecting aortic aneurysms [93], which makes the evaluation of morphological collagen data within arterial walls essential for an improved understanding of vascular health and mechanics. The architecture of the arterial wall, however, represents a major experimental challenge: first, its thickness up to $\sim 1.4\,\mathrm{mm}$ [61] of non-transparent material limits the application of optical techniques to assess the orientation of fibrillar collagen; second, the specific detection of collagen in the three layers of the aortic wall typically requires labeling techniques such as the use of antibodies that are not feasible in thick tissues; third, since the orientation of the fibrillar collagen in the arterial wall responds to the internal blood pressure, any preparation of arterial wall samples for subsequent analysis requires preservation of *in vivo* conditions to obtain reliable information about the orientation of fibrillar collagen.

The use of optical clearing for enhanced visualization of morphological structures in whole organs or thick tissue structures has seen a renewed interest of late. Measurements based on spectroscopy techniques, polarization or optical coherence microscopy as well as nonlinear imaging techniques such as two-photon fluorescence and second-harmonic generation yield more valuable, otherwise virtually inaccessible information when performed on cleared (versus uncleared) soft biological tissue [230]. Often, optical clearing is based on refractive index matching of various scatterers (e.g., collagen) and the ground matrix of soft tissue (e.g., interstitial fluid), by replacing water in the tissue with a fluid of a similar index of refraction as that of the proteins [231–233]. Multiphoton microscopy (MPM) is especially suited for three-dimensional (3D) visualization [46–48] due to its optical sectioning capability using sequential automated slicing (z-stacks) [234]. In combination with optically cleared tissue there is no more need for manual slicing to obtain images of whole organs or thick tissue structures and furthermore leaves the tissue whole for traditional histological investigations.

At the same time, numerical modeling based on continuum mechanical frameworks has developed into a powerful tool for hypothesis testing and verification of theoretical frameworks against experimental and clinical observations; see, e.g., [155, 235]. Despite the broad range of tissues studied through computational analyses (e.g., arteries, cartilage, heart, cornea, etc.), numerical models share the commonality of requiring physiologically determined material and/or structural parameters that can usually be obtained from biomechanical experiments [236], clinical data [130] or can be extracted from images [237].

Such an analysis, however, requires the integration of various tasks from different disciplines such as tissue preparation and imaging techniques, image analysis as well as numerical modeling. In this study, we aim to overcome these limitations by developing a new, simple, fast and automated method which is a novel way of combining well-established techniques and expertise from different fields for the purpose of extracting and quantifying 3D morphological data from optically cleared whole tissues.

Specifically, we combine tissue clearing using a solution of benzyl alcohol to benzyl benzoate (BABB) [238, 239] with second-harmonic generation (SHG) imaging of fibrillar collagen [49, 50], Fourier-based image analysis for characterizing collagen organization [179, 180, 211], and maximum likelihood estimation (MLE) for distribution fitting of 3D-orientational data sets [216]. Firstly, our method yields the 3D distribution of amplitudes (1° resolution) representing the orientations of fibrillar collagen extracted from a z-stack; secondly it identifies isotropic regions in the tissue where no preferred fiber orientations are observed; thirdly it identifies regions of anisotropy characterized by two structural parameters: one describing the preferred (or principal) orientation of the fibers (denoted μ), and the other describing the degree of fiber alignment (or concentration) about that preferred orientation (denoted b). Both structural parameters can be utilized directly in numerical modeling codes using fiber-reinforced constitutive laws [56, 122, 155].

In general, our method is suited to analyze images containing (straightened) fibrillar structures independent of the type of tissue or material. In this work we use non-atherosclerotic human abdominal aortic tissue samples to explain our approach and additionally introduce a new sample preparation method which allows for the fixation of whole blood vessels approximating *in vivo* geometries (by considering axial pre-stretches and *in vivo* blood pressures [61, 139]). Using our method we are able to present for the first time a continuous 3D distribution (1° resolution) of collagen fiber orientations throughout the entire thickness of the human abdominal aortic wall with a thickness of approximately 1 mm.

5.2 Material and Methods

5.2.1 Tissue preparation and fixation

Five human abdominal aortas without atherosclerotic changes of type IV or higher [146] (age in years and gender (m/f): 53 m, 64 m, 65 f, 65 f, 77 m) were harvested within 24 h of death. The use of autopsy material from human subjects for this study was approved by the Ethics Committee of Medical University of Graz (#: 21-288 ex 09/10). All samples were cleaned from the surrounding tissue, and anatomic landmarks (such as branching of the common iliac arteries) were used to ensure consistent sample locations for all five vessels. To reconstruct the *in vivo* stress/strain state of the abdominal aortas, we developed a custom made device which enabled us to mount the intact aortic tube, stretch it axially and simultaneously pressurize it. The axial stretch was controlled through a video extensometer, the pressure was automatically monitored and kept constant through a high precision pressure reducer (control range: 5.0-200.0 $\pm$ 0.1 kPa). The mounting device was encased in a pneumatic glass basin filled with 4% paraformaldehyde (PFA), where the pre-stretched and pressurized vessel was kept for 12 h for sufficient fixation. All vessels were pre-stretched 12% in the axial direction based on the lower bound of *in vivo* values reported, [148], and pressurized at the average systolic arterial pressure (SAP) of 130 mmHg. After chemical fixation the newly stiff vessel was removed from the mounting device for subsequent optical clearing.

5.2.2 Optical clearing

The vessels were rinsed with phosphate buffered saline (PBS; pH 7.4) to wash off excess PFA, and dehydrated using a graded ethanol series with each step lasting 45 min, according to the following protocol: 50%, 70%, twice at 95%, and twice at 100%. For optical clearing we used a solution of 1:2 benzyl alcohol to benzyl benzoate (BABB). Each vessel was initially submerged into a solution of 1:1 ethanol:BABB for 4 h before submerging them into a 100% BABB solution where they remained to clear for at least 12 h before imaging.

All steps involved in the tissue preparation, fixation and optical clearing were performed at room temperature.

5.2.3 Histology

Cleared aortic specimens were embedded in paraffin and sectioned at five microns. The resulting cross-sections were then stained with picrosirius red (PSR) to highlight fibrillar collagen and Elastica Van Gieson (EVG) to highlight elastin. All images were acquired with a Nikon 80i microscope in combination with Nikon NIS-Elements F software. Magnification was set to $600\times$. Images from the PSR-stained sections were acquired using appropriate polarizing optics.

5.2.4 Nonlinear optical imaging

Second-harmonic generation (SHG) imaging of collagen was performed using an imaging setup consisting of a picosecond laser source and an optical parametric oscillator (OPO; picoEmerald; APE, Germany; HighQ Laser, Austria) integrated into a Leica SP5 confocal microscope (Leica Microsystems, Inc.). To induce SHG of collagen the OPO was tuned to 880 nm. Detection of backscattered second-harmonic signal was achieved using a BP $465/170$ emission filter and with a non-descanned detector (NDD) in epi-mode. Image acquisition was performed using a Leica HCX IRAPO L $25\times/0.95$ water objective with a working distance of 2.5 mm for deep tissue imaging; z-stacks (3D image stacks) of the cleared aorta specimens were acquired using $0.62\times0.62\times1\,\mu$m sampling ($x/y/z$). Image processing of z-stacks (3D Gaussian filtering) and subsequent volume rendering was performed using Amira visualization software (Visage Imaging, Inc.).

5.2.5 Fiber orientation assessment.

To extract collagen fiber orientations from 2D images we used a Fourier-based image analysis method in combination with wedge filtering [237]. Towards this end, we applied a window using a raised cosine function to reduce the grayscale values to 0 at the image periphery, which could otherwise cause frequency-domain effects in subsequent steps. Next we applied a Fast Fourier Transformation (FFT) to the windowed grayscale image, represented by a distribution function $f(x,y)$ where (x,y) are spatial coordinates, yielding $\mathcal{F}(f(x,y)) = F(u,v)$ where (u,v) is a point in Fourier space. After performing a coordinate shift, which transforms the lowest spatial frequency to the origin, we calculated the power spectrum P by multiplying the Fourier Transform with its complex conjugate, namely

$$P(u,v) = F(u,v)\cdot F^*(u,v). \tag{5.1}$$

To extract the fiber directions from the power spectrum, which are now discriminated by spatial frequency and orientation, we used wedge-shaped orientation filters [211]. By means of summation of every $P(u,v)$ within individual 1° wedges, we obtained a discrete distribution of relative amplitudes $I(\Phi)$ (in %) as a function of the corresponding fiber angle Φ. Finally, the angular distribution was shifted back by 90° to adjust for the shift owing to the Fourier transformation. This procedure was performed for all n images in a z-stack, yielding a 3D dataset per z-stack containing $I(\Phi)$ of every image. The angles Φ and amplitudes I for individual images n were stored in the x-, y-, and z-directions of the dataset, respectively; $\Phi = 0^\circ$ and $\Phi = 90^\circ$ correspond to the horizontal and vertical axes of the images, as well as to the circumferential and axial directions of the vessel, respectively.

5.2.6 Determination of anisotropy.

In order to perform meaningful distribution fitting, we first distinguish between anisotropic and isotropic angular fiber distributions (the latter is not subjected to subsequent distribution fitting). Towards this end, we first smoothed the amplitudes of the original 3D dataset using moving average filters in the z- and then in the x-direction with a span range of 17° and 33°, respectively. To ensure that our choice for both span ranges was robust we performed a perturbation analysis. Note that a robust choice implies that the outcome regarding isotropy or anisotropy was not affected by small perturbations ($\sim \pm 5^\circ$) of either span range. To check for isotropy of a given distribution we made use of the fact that the cumulative distribution function (CDF) $F(\Phi)$ of an isotropic distribution is a straight line. Therefore, we calculated the CDF of every (now smoothed) angular distribution in the 3D dataset, according to

$$F = \sum_{\Phi_i=-90^\circ}^{x} I(\Phi_i), \tag{5.2}$$

where $-90^\circ \leq x \leq 89^\circ$, fitted it with a first-order polynome and determined the corresponding R^2 value as a measure of the goodness-of-fit. If the resulting R^2 value was above a threshold of 0.998 then the distribution was considered isotropic, otherwise anisotropic. We determined the appropriate threshold value by running a perturbation analysis for a broad range of potential thresholds. The most suited threshold value was identified based on where the results (isotropy or anisotropy) would correspond well to the fiber morphology visible in the original images. An illustrative example is shown in Fig. 5.1.

5.2.7 Distribution fitting.

To fit the anisotropic distributions using maximum likelihood estimation (MLE) we first needed to determine the number of major peaks (fiber families) for every distribution $I(\Phi)$

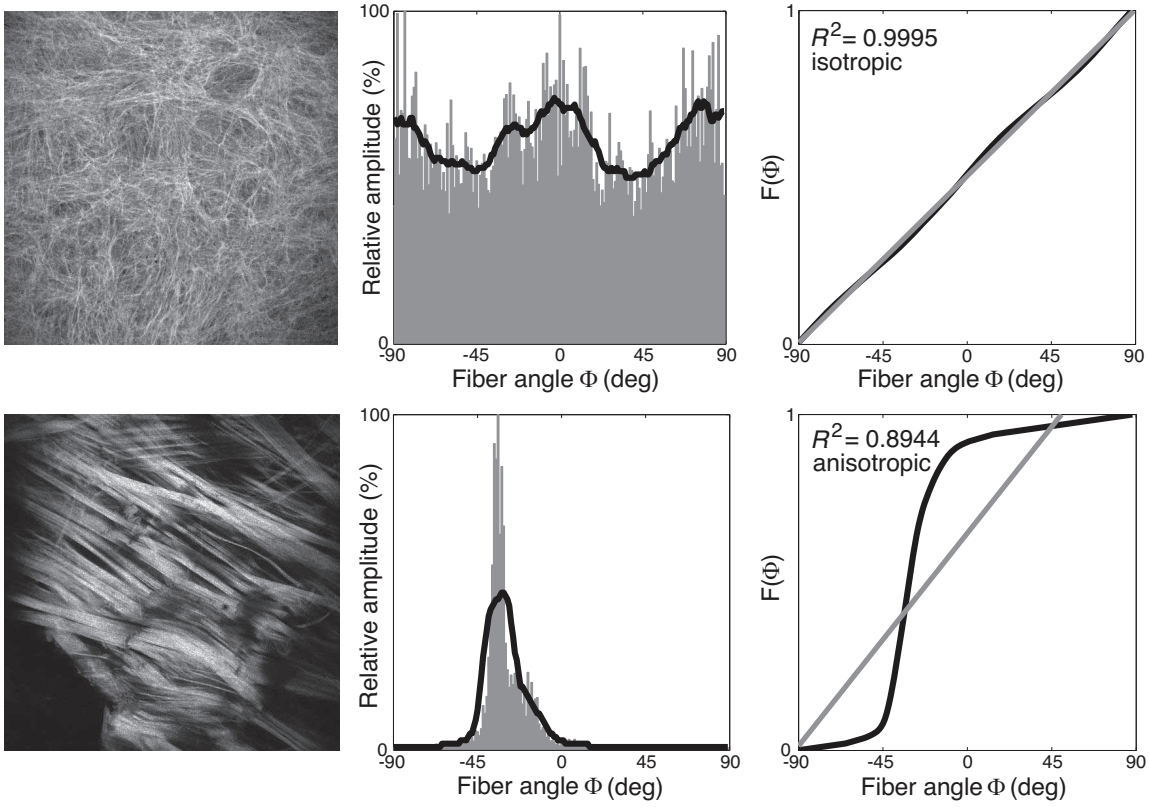

Figure 5.1: Schematic of steps to distinguish between images showing an isotropic versus anisotropic fiber distribution. Two cases, one classified as isotropic (top row) and another one classified as anisotropic (bottom row) are shown. All images were acquired using second-harmonic generation imaging. The distribution of relative amplitudes (gray bars, second column) was determined through Fourier-based image analysis and subsequently smoothed using a moving average filter (solid black curves). From the smoothed distribution the cumulative distribution function $F(\Phi)$ was calculated (third column, black curves), fitted with a first-order polynome (gray curves), and the corresponding R^2 value was determined. If R^2 was above a threshold level of 0.998 then the distribution was considered to be isotropic, otherwise anisotropic.

in a 3D dataset and second, the approximate locations Φ of those peaks used as starting parameters for subsequent MLE fitting. To that end, we first smoothed the amplitudes of the original (unsmoothed) 3D dataset using moving average filters in the *z*- and then in the *x*-direction with a span range of 7° for both directions. Next we used a standard peak detection algorithm, based on the alternating signs of the derivatives, to identify local maxima or minima in the smoothed angular distribution, yielding the locations of the major peaks. Subsequently, amplitude offsets were removed by subtracting the smallest amplitude value from every $I(\Phi)$. Depending on the number of peaks *m* (which was either one or two per image), each distribution was then fitted with either one or a mixture of two π-periodic

von Mises distributions [122, 202, 237], given by

$$\rho(\Phi) = \sum_{i=1}^{m} \frac{\exp\{b_i \cos[2(\Phi - \mu_i)]\}}{I_0(b_i)}. \tag{5.3}$$

The fitting parameters are the concentration parameter b_i, determining the shape of the von Mises distribution (increased b_i-values correspond to narrower (more anisotropic) distributions), and the location parameter μ_i, describing the preferred (or principal) fiber orientation. Normalization is not necessary since $\rho(\Phi)$ was only used to determine the fitting parameters [218]; $I_0(b_i)$ denotes the modified Bessel function of the first kind of order zero, namely

$$I_0(b_i) = \frac{1}{\pi} \int_0^{\pi} \exp(b_i \cos\alpha) \mathrm{d}\alpha, \tag{5.4}$$

with $i = 1, 2$.

5.3 Results

The orientations of collagen fibers in a z-stack are represented by the 3D distribution of the corresponding amplitudes with 1° resolution. By fitting this distribution using MLE and π-periodic von Mises distributions (either one or a mixture of two in the case of two fiber families), our method identifies specific regions of isotropy within the tissue and characterizes anisotropic regions by determining both structural parameters b and μ.

5.3.1 Optical clearing and histology

Figure 5.2 illustrates the effect of optical clearing using a solution of BABB; a segment of a human abdominal aorta before and after clearing is shown in the top row, left and right panel, respectively. Note the translucent nature of the cleared vessel, also visible by the lighter shadow under the same lighting conditions. To ensure that the clearing procedure did not negatively affect the microscopic structure of collagen fibers we performed additional investigations on histological sections. Representative picrosirius red (PSR) and Elastica Van Gieson (EVG) stained cross-sections are shown in the bottom row of Fig. 5.2, left and right panel, respectively. Both revealed that collagen (bright red under polarized light) and elastin (black in the EVG stained section) are consistent with observations one can expect from standard formalin fixed, paraffin embedded tissue samples.

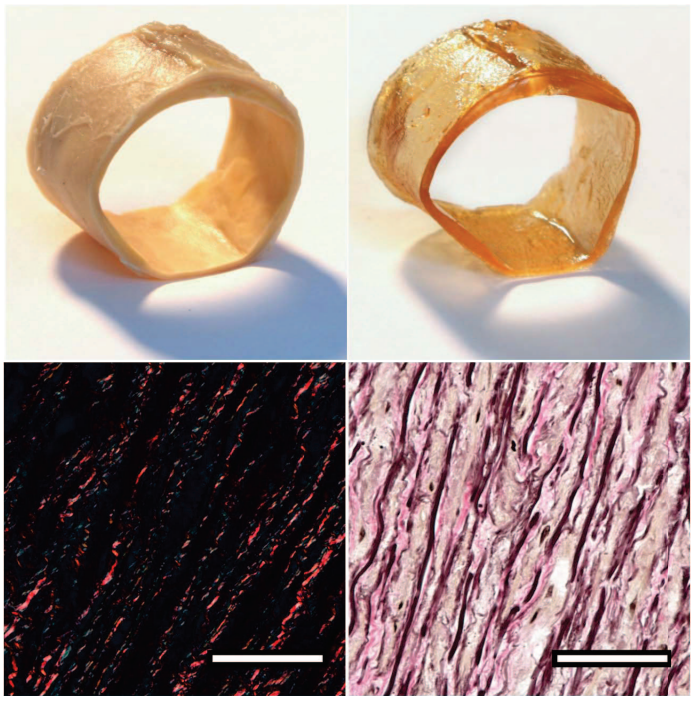

Figure 5.2: Effect of optical clearing using BABB. Top row: left and right panels show a segment of a human abdominal aorta before and after optical clearing, respectively. Note the translucent appearance of the cleared vessel, also visible by the lighter shadow under the same lighting conditions. Bottom row: both cross-section images were obtained from optically cleared tissues and stained subsequently with picrosirius red for visualizing collagen (left; collagen appears bright red under dark-field polarized light) and Elastica Van Gieson as a general stain (right; elastic fibers and nuclei appear black, collagen stains pink, muscle and cytoplasm stains light brown/yellowish). The appearances of both images are consistent with photographs of standard formalin fixed tissues.

5.3.2 3D visualization

The left panel in Fig. 5.3 shows a volume rendered radial projection (circumferential/radial plane; x/z) of an image stack (z-stack), featuring collagen fibers throughout the thickness of the aortic wall. In-plane volume rendered projections (circumferential/axial plane; x/y) of regions from the intima, media, and adventitia are highlighted individually in the smaller panels I, II and III, respectively; the horizontal and vertical sides of panels I-III correspond to the circumferential (x) and axial (y) axes of the vessel. Note the different fiber morphologies between the three arterial layers: in the adventitia (panel I) the fibers were generally organized in thick fiber bundles, oriented mostly diagonally (with high variations) between the major axes; in the media (panel II) the fibers were organized closer to the circumferential direction of the vessel but still showed two preferred fiber orientations; in the intima (panel III) we observed both, regions of preferred fiber orientations as well as regions of increasingly isotropic fiber morphologies.

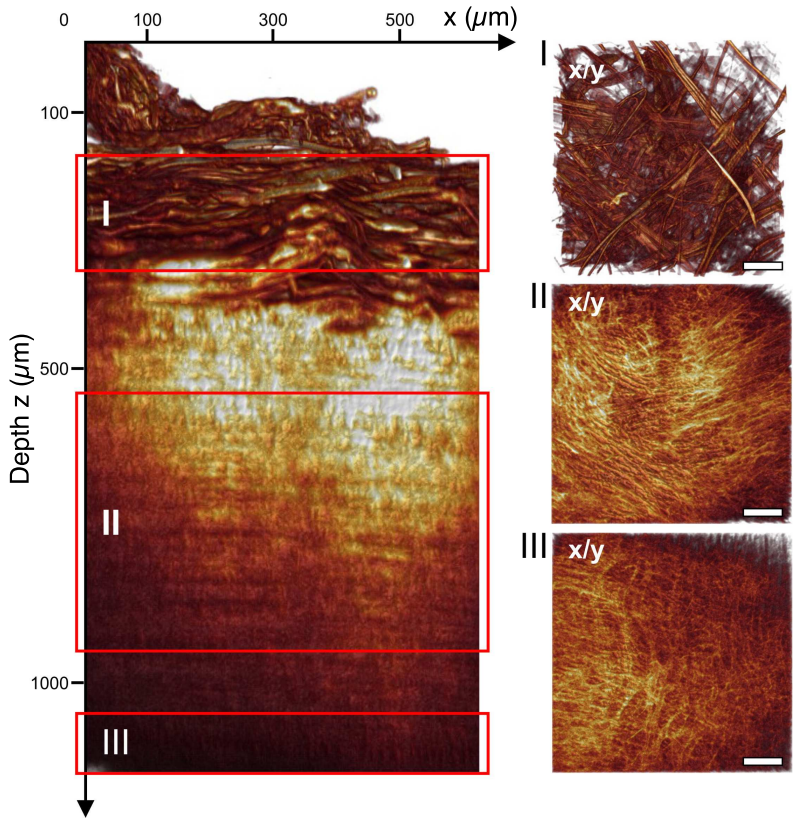

Figure 5.3: Volume rendering of optical sections through an entire aortic wall acquired using second-harmonic generation imaging. The left panel shows a radial projection (circumferential/radial plane; x/z) highlighting fibrillar collagen throughout the thickness a human abdominal aortic wall (age: 65yr, gender: f). The three smaller panels on the right are in-plane projections (circumferential/axial plane; x/y) from regions inside the adventitia (I), media (II), and intima (III), indicated by the red boxes in the left panel. Note the marked differences in collagen fiber morphology between the three arterial layers. Generally, the adventitia displayed characteristic fiber bundles, often organized as two counter-rotating fiber families oriented mostly between the major vessel axes; in the media the fiber bundles changed into one fiber family, organized in a layered structure with alternating orientations closer to the circumferential direction. The intima of this vessel was characterized by a mostly isotropic organization of collagen fibers, while intimas of other vessels also displayed anisotropic fiber morphologies.

5.3.3 Continuous 3D fiber orientations

Figure 5.4, top panel, is a representation of the 3D collagen fiber orientations with a 1° resolution throughout the entire thickness of the aortic wall (obtained from the z-stack shown in Fig. 5.3); $\Phi = 0°$ and 90° denote the circumferential and axial directions of the vessel, respectively. The colors denote relative changes in amplitudes ranging from dark blue (0%) to dark red (100%). Therefore, orientations of preferred (or principal)

fiber directions (or fiber families) appear red while blue corresponds to orientations with only few to no fibers present. The dashed lines indicate the transition regions between the arterial layers. In the adventitia we observed highly aligned fiber orientations (note the relatively large dark blue areas between red regions of preferred orientations) with often two counter-rotating fiber families present, generally oriented between the major vessel axes. The adventitia is followed by a marked transition layer (indicated by the striped box on the left), characterized by a change in appearance of the collagen fibers. The thick fiber bundles visible in the adventitia could not be observed anymore and the preferred orientations of the fibers became axial ($\sim 90^\circ$). Subsequently comes the media which displayed a layered structure of alternating preferential fiber orientations (layers of single fiber families with alternating orientations) closer to the circumferential direction, located around $\Phi \sim \pm 20^\circ$. Next, the intima of this vessel was characterized by an isotropic fiber morphology which at regions closest to the lumen changed into preferred fiber orientations in the axial direction.

We emphasize that we observed strong biological variabilities in fiber orientations among the intimas of different aortas; while some showed preferential orientations in various directions (depending on the sample it could be, e.g., two fiber families oriented diagonally or one fiber family oriented axially or circumferentially), others displayed mostly isotropic regions. A representative example which highlights these changes in morphology throughout the entire thickness of the wall is given in the bottom panel of Fig. 5.4, where the relative amplitudes at the locations $\Phi = +27^\circ$ (dashed black curve) and $\Phi = -27^\circ$ (gray curve) as a function of depth z are plotted. In the adventitia the shapes of both amplitude curves tend to overlap, suggesting that two fiber families lie within the same imaging plane (circumferential/axial plane; x/y) which was confirmed by individual MPM images of the adventitia revealing the presence of two fiber families. In the media, on the other hand, the similar behavior of both curves clearly changes into an alternating pattern, characteristic for a layered fiber family structure with alternating orientations (Fig. 5.4, top).

5.3.4 Parameter determination for numerical modeling

A representative example of fitting the fiber orientations extracted from a single MPM image (taken from the media) using MLE with one π-periodic von Mises distribution is shown in Fig. 5.5 including corresponding R^2 and P values as a measure for the goodness of fit. From the fit we obtained the location parameter $\mu = -22.7^\circ$ describing the principal fiber orientation of the distribution as well as the concentration parameter $b = 1.44$ which determines the shape of the von Mises distribution. Both, μ and b were calculated for every image in the z-stack, yielding the continuous behavior of both parameters throughout the thickness of the entire wall, as shown in Fig. 5.6. Note that regions with no data points correspond to regions with isotropic fiber distributions.

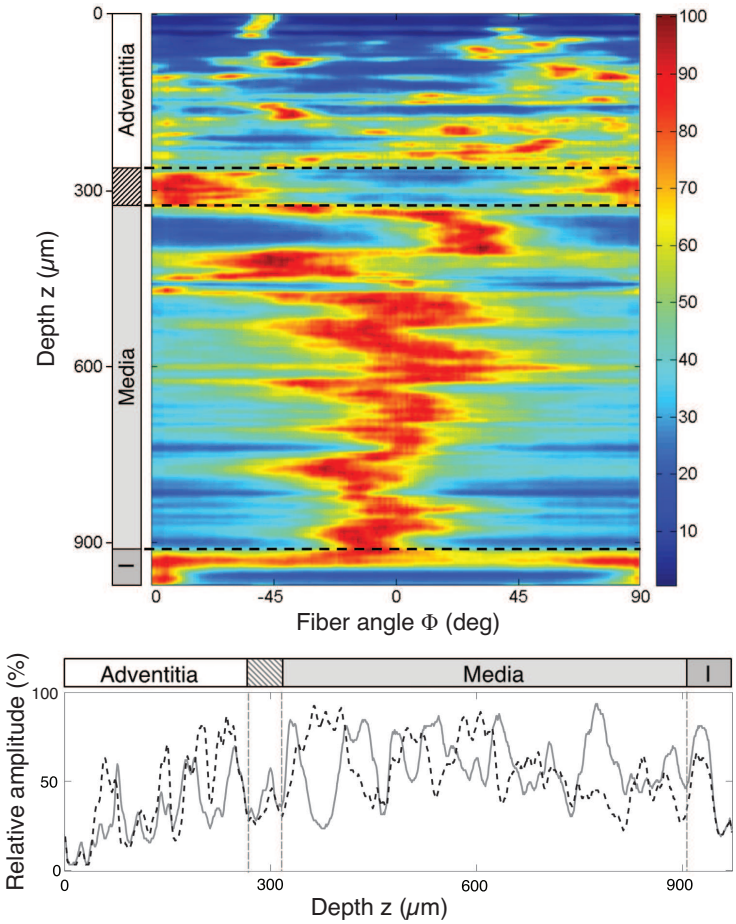

Figure 5.4: Representation of the 3D collagen fiber orientations throughout the entire thickness of a human abdominal aortic wall (age: 65yr, gender: f). Top panel: the angles $\Phi = 0^\circ$ and 90° denote the circumferential and axial directions of the vessel, respectively, the colors correspond to relative amplitudes ranging from dark blue (0%) to dark red (100%). Orientations of preferred fiber directions appear red, while blue regions represent orientations with a low fiber density. The striped box on the left indicates the transition layer between the adventitia and the media; I = intima. Bottom: changes of relative amplitudes as a function of depth at two representative locations. The dashed black curve corresponds to amplitudes at $\Phi = +27^\circ$, the gray curve at $\Phi = -27^\circ$ (0° = circumferential). A similar behavior of both curves in the adventitia turns into an alternating pattern in the media, indicating a change in the structural organization of collagen fibers between the two layers; from two fiber families in the adventitia to one fiber family with alternating orientations in the media.

The results in Fig. 5.6, top panel, highlight that in the adventitia often two counter rotating fiber families were observed oriented at around $\Phi \sim \pm 45^\circ$, while in the media only one fiber family with alternating orientations closer to the circumferential direction ($\Phi \sim \pm 20^\circ$) was present. In the transition layer between the adventitia and the media a preferred axial

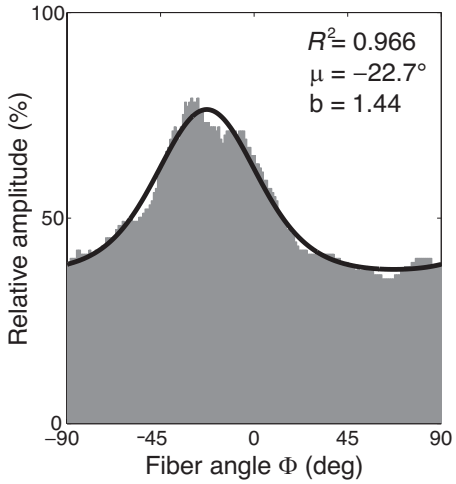

Figure 5.5: Angular distribution of relative amplitudes fitted with a π-periodic von Mises distribution. The distribution was extracted from a single MPM image taken from the media featuring one fiber family (corresponding to the location at 634 μm in Fig. 5.4, top). The angles $\Phi = 0^\circ$ and 90° denote the circumferential and axial directions of the vessel, respectively. From the fit we extracted the location parameter μ describing the preferred (or principal) fiber orientation and the concentration parameter b as a measure of the degree of fiber alignment about μ. An increase in b corresponds to a narrower (more anisotropic) distribution.

fiber orientation was observed. The intima of this vessel consisted largely of isotropic regions, which changed into one fiber family oriented in the axial direction closest to the lumen. The concentration parameter b showed relatively small variations throughout the media (Fig. 5.6, bottom) and was generally slightly higher in the adventitia ($\bar{b}_\mathrm{a} = 1.55 \pm 0.89$, mean $\pm$ s.d.) compared to the media ($\bar{b}_\mathrm{m} = 1.33 \pm 0.42$), indicating that the observed collagen fiber distributions were more aligned (more anisotropic) in the adventitia. The very high values for b at the beginning of the adventitia ($b > 5$) correspond to images containing only a few highly aligned thick collagen fiber bundles, as can be seen in Fig. 5.3 (panel I), and were omitted in the calculation of $\bar{b}_\mathrm{a}$. In the intima, close to the lumen, we observed an increased fiber alignment ($\bar{b}_\mathrm{i} = 3.57 \pm 0.74$).

5.4 Discussion

Based on established tools from different research fields we are introducing a new method, which allows for a simple, fast and automated structural analysis of collagenous tissues or whole organs that have been optically cleared and imaged using nonlinear microscopy. Our method yields a 3D orientational distribution accurately representing the morphology of fibrillar tissue structures, and it additionally extracts structural parameters that can be

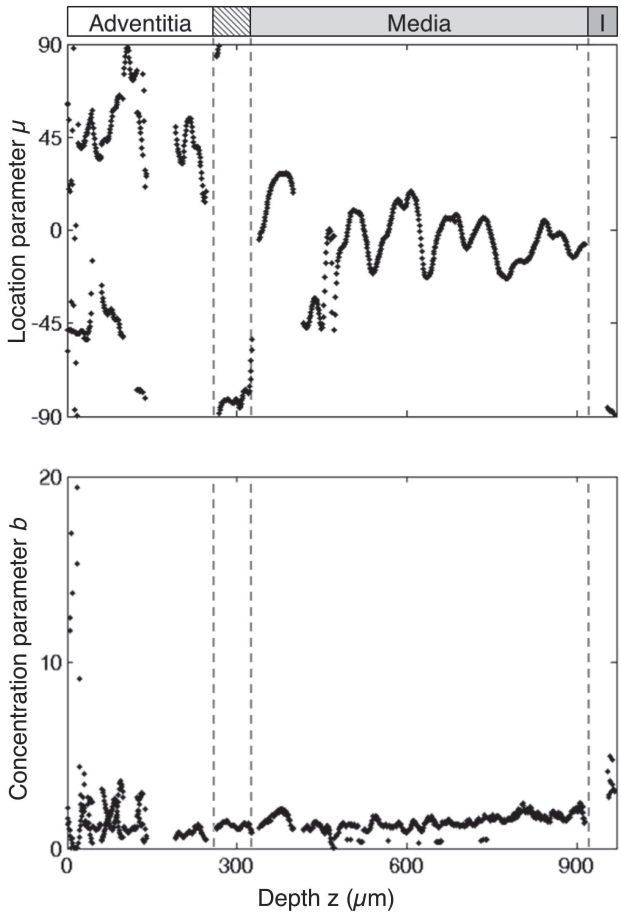

Figure 5.6: Changes in preferred fiber orientations and fiber alignment throughout the entire thickness of the aortic wall. Top: in the adventitia often two counter rotating principal fiber directions were observed while the media was characterized by alternating principal directions, oriented closer to the circumferential direction of the vessel. In the intima (I) only regions closest to the lumen showed anisotropic fiber alignment in the axial direction ($\sim \pm 90^{\circ}$), oriented along the direction of blood flow. Bottom: the concentration parameter b quantifies the degree of fiber alignment about the preferred fiber orientation μ (Fig. 5.5), therefore, describing its degree of anisotropy. Increasing b values correspond to a narrower (more aligned) distribution. Generally, in the adventitia increased values of b were found compared to the media. Note that values of approximately $b > 4$ typically came from images containing a few highly aligned fiber bundles.

utilized in numerical models for soft biological tissues. We used tissue samples from human abdominal aortas to outline the method and in the course of this paper we presented novel results pertaining to the structure of aortic walls.

To approximate the *in vivo* condition of the vessel as closely as possible we developed a custom made device allowing us to mount and chemically fixate (using formalin) the intact segment (tube) of the abdominal aorta as a whole, and subsequently apply a physi-

ologically axial pre-stretch (approximately 12% [148]) and simultaneously pressurize it at constant systolic arterial pressure of 130 mmHg. The influence and importance of pressurization and axial pre-stretches upon fiber morphology has been previously reported [61, 137, 139, 204] and is not only a prerequisite for mimicking *in vivo* states of the vessel, but also leads to (mostly) straightened collagen fibers necessary for a correct determination of fiber angles. Furthermore, our new sample preparation method allows for future studies of the influence of arterial blood pressure on collagen fiber orientations or investigations of microstructural recruitment variables for collagen [240].

Optical clearing using BABB leads to an increase in MPM penetration depth from $\sim 120\,\mu$m (in the uncleared sample) to more than 1 mm, enabling us to image the entire thickness of the vessel wall without physically damaging the tissue [230]. Histological investigations using standard tissue stains (PSR and VVG) confirmed that the microstructural tissue components (collagen and elastin) were still intact after optical clearing (Fig. 5.2). A comparison of fiber distributions before and after clearing showed that the microscopical orientations were not affected by the clearing process.

Using second-harmonic generation imaging, we can show, for the first time, a complete 3D visualization of collagen fibers throughout the entire wall thickness of a human abdominal aorta (Fig. 5.3, Supplementary Videos 1 and 2). Visually we observed some basic similarities between the five vessels we investigated: the adventitias showed characteristic fiber bundles, often organized as two counter-rotating fiber families, mostly oriented between the major vessel axes (Fig. 5.3, panel I); next came a transition layer leading to the media in which the marked organization into fiber bundles disappeared; the medias generally displayed one fiber family organized in a layered structure with two alternating preferential orientations; the observed morphologies among the five intimas varied greatly, therefore, rendering general statements inadequate for the used number of samples. Some displayed large areas of isotropic fiber distributions while others showed preferential fiber orientations in various directions. For example, the intima of the vessel in Fig. 5.3 consisted of isotropic orientations adjacent to the media which became anisotropic close to the lumen, oriented along the direction of the blood flow (top panels Figs. 5.4 and 5.6). These observations are consistent with previously reported mean values for the three arterial layers [61], where two fiber families were observed in the adventitia and media and several fiber families as well as isotropic distributions were found in the intimas. Instead of having to rely on mean values for each layer, our new method provides the required 3D spatial depth resolution to show in detail how the fiber families are organized within each layer.

To extract the fiber orientations from images we employed Fourier power spectrum analysis in combination with wedge filtering [179, 180, 211, 237]. Firstly, it is the rotational property, secondly the addition theorem and thirdly the shift theorem of the Fourier transform that ensure that the fiber orientations visible in an image are correctly represented by the distribution of relative amplitudes in Fourier space.

A statistical analysis of the cumulative distribution functions (CDF), calculated from amplitude distributions, was used as an objective measure to identify regions of isotropy and anisotropy in the tissue. Note that anisotropic regions are characterized by a preferred direction of fiber orientations versus isotropic regions which show arbitrary fiber orientations. For distribution fitting of anisotropic regions we used either one or (in the case of two preferred fiber orientations) a mixture of two von Mises distributions from which we determined μ, describing the principal fiber orientation and b, a measure for the fiber alignment about μ (Fig. 5.5). Our choice for using a von Mises distribution was based on well-established modeling frameworks of arterial tissues [122, 202, 205, 206, 237], in which b can be utilized to calculate dispersion parameters which, together with μ, can be directly used in the numerical modeling or finite element analyses, even in commercial codes such as Abaqus (SIMULIA, Providence, RI). The decision to perform distribution fitting through MLE instead of a simple least-squares method was motivated by its independence of bin size and the potential pitfalls arising from the normality-, constant variance-, and independent-errors assumptions [223]. Using our method, we present for the first time the (continuous) values of both modeling parameters μ and b throughout the thickness of the human aortic wall (Fig. 5.6).

The 3D quantification of fiber orientations (Fig. 5.4, top) confirmed our visual impression that the collagen fibers in the adventitia were oriented more axially and showed higher anisotropy (note the dark blue regions between preferred orientations) compared to the media, where they were oriented closer to the circumferential direction and the fiber alignment was less pronounced (note the light blue to turquoise regions indicating some presence of fibers in all directions). By analyzing the behavior of relative amplitudes throughout the entire thickness of the aortic wall, we were able to identify depth-resolved changes in the structural organization of the collagen fiber families (Fig. 5.4, bottom). For the first time we present continuous quantitative data showing the presence of two counter rotating fiber families in the adventitia (lying within axial-circumferential planes), while only one fiber family with alternating orientations between sequential axial-circumferential planes was found in the media. The results for the location parameter μ in Fig. 5.6, top panel, additionally highlighted the alternating nature of preferred fiber orientations in the media, and the more fluctuating orientations in the adventitia, which was found to be characteristic of all five vessels and corresponds well with previously reported differences in the qualitative mechanical stress-stretch response of abdominal aortas [204] and carotid arteries [58].

Compared to previous studies of collagen organization in human arteries [137, 139, 241], our method is non-destructive, yields continuous data throughout the entire thickness of soft biological tissues, therefore, allowing for investigations of specific locations inside the tissue (e.g., transition regions between the three arterial layers). Due to the automated nature of our method, it is not subject to limitations such as human measurement bias or fair sampling (both pose a risk when, e.g., measuring collagen fiber angles using polarized light [61]).

With an ultimate tensile strength in the range of 50-100 MPa [26], collagen fibers are responsible for the strength and load resistance of the arterial wall. Therefore, understanding their microscopic structure and changing morphologies throughout the three layers of the wall is key in the analysis of mechanical quantities such as stress and strain, both of which are used as a basis for numerical modeling of growth and remodeling processes, see, e.g., [127].

Acknowledgment This work was partly supported by the Austrian Science Funds (FWF) to A.J.S. (project I 503-B11), as well as to H.W. and S.D.K. (project SFB F3005 Lipotox).

REFERENCES

[1] Vuorio E, De Crombugghe B. The family of collagen genes. *Annu. Rev. Biochem.* 1990; **59**:837–872.

[2] Van der Rest M, Garrone R. Collagen family of proteins. *FASEB J.* 1991; **5**:2814–2823.

[3] Diez J. Arterial stiffness and extracellular matrix. *Atherosclerosis, Large Arteries and Cardiovascular Risk*, Safar ME, Frohlich ED (eds.), Karger: Basel, 2007; 76–95.

[4] Hulmes DJS. Collagen diversity, synthesis and assembly. *Collagen: Structure and Mechanics*, Fratzl P (ed.), Springer, 2008; 15–47.

[5] Grant RA. Content and distribution of aortic collagen, elastin and carbohydrate in different species. *J. Atheroscler. Res.* 1967; **7**:463–472.

[6] Fitzsimmons CM, Shanahan CM. Vascular extracellular matrix. *Panvascular Medicine*, Lanzer P, Topol EJ (eds.). Springer: Berlin, 2002; 217–231.

[7] Reiser K, McCormick RJ, Rucker RB. Enzymatic and nonenzymatic cross-linking of collagen and elastin. *FASEB J.* 1992; **6**:2439–2449.

[8] Molnar J, Fong KS, He QP, Hayashi K, Kim Y, Fong SF, Fogelgren B, Szauter KM, Mink M, Csiszar K. Structural and functional diversity of lysyl oxidase and the LOX-like proteins. *Biochim. Biophys. Acta* 2003; **1647**:220–224.

[9] Lucero HA, Kagan HM. Lysyl oxidase: an oxidative enzyme and effector of cell function. *Cell Mol. Life Sci.* 2006; **63**:2304–2316.

[10] Verderio EA, Johnson TS, Griffin M. Transglutaminases in wound healing and inflammation. *Prog. Exp. Tumor Res.* 2005; **38**:89–114.

[11] Ward NP, Hulmes DJS, Champman JA. Collagen self-assembly in vitro: electron microscopy of initial aggregates formed during the lag phase. *J. Mol. Biol.* 1986; **190**:107–112.

[12] Ottani V, Martini D, Franchi M, Ruggeri A, Raspanti M. Hierarchical structures in fibrillar collagens. *Micron* 2002; **33**:587–596.

[13] Wess TJ. Collagen fibrillar structure and hierarchies. *Collagen. Structure and Mechanics,* Fratzl P (ed.), Springer-Verlag: Heidelberg, 2008; 49–80.

[14] Hodge AJ, Petruska JA. Recent studies with the electron microscope on ordered aggregates of the tropocollagen molecule. *Aspects of Protein Chemistry,* Ramachandran GN (ed.). Academic Press: London, 1963; 289–300.

[15] Bouteille M, Pease DC. The tridimensional structure of native collagenous fibrils, their proteinaceous filaments. *J. Ultrastruct. Res.* 1971; **35**:314–338.

[16] Pease DC, Bouteille M. The tridimensional ultrastructure of native collagenous fibrils, cytochemical evidence for a carbohydrate matrix. *J. Ultrastruct. Res.* 1971; **35**:339–358.

[17] Hulmes DJS, Miller A, Parry DAD, Piez KA, Woodhead-Galloway J. Analysis of the primary structure of collagen for the origins of molecular packing. *J. Mol. Biol.* 1973; **79**:137–148.

[18] Hofmann H, Fietzek PP, Kuhn K. Comparative analysis of the sequences of the three collagen chains a1 (i), a2 (ii) and a1 (iii); Function and genetic aspects. *J. Mol. Biol.* 1980; **141**:293–314.

[19] Fraser RDB, MacRae TP, Miller A, Suzuki E. Molecular conformation and packing in collagen fibrils. *J. Mol. Biol.* 1983; **167**:497–521.

[20] Provenzani PP, Vanderby R. Collagen fibril morphology and organization: implications for force transmission in ligament and tendon. *Matrix Biol.* 2006; **25**:71–84.

[21] Parry DAD, Barnes GRG, Craig AS. A comparison of the size distribution of collagen fibrils in connective tissues as a function of age and a possible relation between fibril size distribution and mechanical properties. *Proc. R. Soc. Lond. B* 1978; **203**:305–321.

[22] Ottani V, Raspanti M, Ruggeri A. Collagen structure and functional implications. *Micron* 2001; **32**:251–260.

[23] Kannus P. Structure of the tendon connective tissue. *Scand. J. Med. Sci. Spor.* 2000; **10**:312–320.

[24] Fratzl P, Misof K, Zizak I, Rapp G, Amenitsch H, Bernstorff S. Fibrillar structure and mechanical properties of collagen. *J. Struct. Biol.* 1997; **122**:119–122.

[25] Gordon JE. *The science of structures and materials*. Scientific American Library: Distributed by Freeman: New York, 1988.

[26] Fung YC. *Biomechanics. Mechanical Properties of Living Tissues*. 2nd edn., Springer-Verlag: New York, 1993.

[27] Wainwright SA, Biggs WD, Currey JD, Gosline JM. *Mechanical Design in Organisms*. Princeton University Press, 1976.

[28] Vincent V. *Structural Biomaterials*. Princeton Univ. Press: New Jersey, 1990.

[29] Holzapfel GA. Biomechanics of soft tissue. *The Handbook of Materials Behavior Models. Volume III, Multiphysics Behaviors, Chapter 10, Composite Media, Biomaterials*, Lemaitre J (ed.), Academic Press: Boston, 2001; 1049–1063.

[30] Diamant J, Keller A, Baer E, Litt M, Arridge RGC. Collagen: Ultrastructure and its relation to mechanical properties as a function of ageing. *Proc. R. Soc. Lond. B* 1972; **180**:293–315.

[31] Misof K, Rapp G, Fratzl P. A new molecular model for collagen based on synchrotron x-ray scattering evidence. *Biophys. J.* 1997; **72**:1376–1381.

[32] Folkhard WE, Mosler W, Geerken E, Knörzer E, Nemetschek-Gonsler H, Nemetschck T, Koch MHJ. Quantitative analysis of the molecular sliding mechanism in native tendon collagen - Time-resolved dynamic studies using synchrotron radiation. *Int. J. Biol. Macromol.* 1986; **9**:169–175.

[33] Valentin G. *Die Untersuchung der Pflanzen und der Thiergewebe in polarisiertem Lichte*. Wilhelm Engelmann: Leibzig, 1861.

[34] Schmidt WJ. Polarisationsoptische Analyse des submikroskopischen Baues von Zellen und Geweben. *Handbuch der biologischen Arbeitsmethoden, Abt V, Teil 10*, Abderhalden E (ed.). Urban & Schwarzenberg: Berlin, 1934; 435–665.

[35] Missmahl HP. Doppelbrechung der reticulären Faser und sich hieraus ergebender Nachweis von gerichtet eingelagerten Lipoiden in die reticuläre Faser. *Z. Zellforsch.* 1957; **45**:612–619.

[36] Wolman M, Kasten FH. Polarized light microscopy in the study of the molecular structure of collagen and reticulin. *Histochemistry* 1986; **85**:41–49.

[37] Junqueira LC, Cossermelli W, Brentani R. Differential staining of collagens type I, II and III by Sirius Red and polarization microscopy. *Arch. Histol. Jpn.* 1978; **41**:267–274.

[38] Junqueira LC, Bignolas G, Brentani RR. Picrosirius staining plus polarization microscopy, a specific method for collagen detection in tissue sections. *Histochem. J.* 1979; **11**:447–455.

[39] Junqueira LCU, Montes GS, Sanchez EM. The influence of tissue section thickness on the study of collagen by the picrosirius-polarization method. *Histochemistry* 1982; **74**:153–156.

[40] Roth S, Freund I. Optical second-harmonic scattering in rat-tail tendon. *Biopoly.* 1981; **20**:1271–1290.

[41] Georgiou E, Theodossiou T, Hovhannisyan V, Politopoulos K, Rapti GS, Yova D. Second and third optical harmonic generation in type I collagen, by nanosecond laser irradiation, over a broad spectral region. *Opt. Comm.* 2000; **176**:253–260.

[42] Campagnola PJ, Clark HA, Mohler WA, Lewis A, Loew LM. Second-harmonic imaging microscopy of living cells. *J. Biomed. Opt.* 2001; **6**:277–286.

[43] Richards-Kortum R, Sevick-Muraca E. Quantitative optical spectroscopy for tissue diagnosis. *Annu. Rev. Phys. Chem.* 1996; **47**:555–606.

[44] Masters BR, So PTC. Multiphoton excitation microscopy and confocal microscopy imaging of in vivo human skin: a comparison. *Microsc. Microanal.* 1999; **5**:282–289.

[45] Agarwal A, Coleno ML, Wallace VP, Wu WY, Sun CH, Tromberg BJ, George SC. Two-photon laser scanning microscopy of epithelial cell-modulated collagen density in engineered human lung tissue. *Tissue Eng.* 2001; **7**:191–202.

[46] Denk W, Strickler JH, Webb WW. Two-photon laser scanning fluorescence microscopy. *Science* 1990; **248**:73–76.

[47] Zipfel WR, Williams RM, Webb WW. Nonlinear magic: multiphoton microscopy in the biosciences. *Nat. Biotechnol.* 2003; **21**:1368–1376.

[48] Williams RM, Zipfel WR, Webb WW. Interpreting second-harmonic generation images of collagen I fibrils. *Biophys. J.* 2005; **88**:1377–1386.

[49] Zoumi A, Lu X, Kassab GS, Tromberg BJ. Imaging coronary artery microstructure using second-harmonic and two-photon fluorescence microscopy. *Biophys. J.* 2004; **87**:2778Ű–2786.

[50] Schenke-Layland K, Riemann I, Stock UA, König K. Imaging of cardiovascular structures using near-infrared femtosecond multiphoton laser scanning microscopy. *J. Biomed. Opt.* 2005; **10**:024 017.

[51] Moore KL, Dalley A. *Clinically Oriented Anatomy*. 4th edn., Lippincott Williams & Wilkins: Baltimore, 1999.

[52] Clark JM, Glagov S. Structural integration of the arterial wall. I. Relationships and attachments of medial smooth muscle cells in normally distended and hyperdistended aortas. *Laboratory Investigation* 1979; **40**:587–602.

[53] Glagov S, Vito R, Giddens DP, Zarins CK. Micro-architecture and composition of artery walls: relationship to location, diameter and the distribution of mechanical stress. *Hypertension* 1992; **10**:101–104.

[54] Labrosse MR. Structure and mechanics of the artery. *Vascular Mechanics and Pathology*, Thubrikar MJ (ed.). Springer: New York, 2007; 45–81.

[55] Holzapfel GA. Collagen in arterial walls: Biomechanical aspects. *Collagen. Structure and Mechanics*, Fratzl P (ed.), Springer-Verlag: Heidelberg, 2008; 285–324.

[56] Holzapfel GA, Gasser TC, Ogden RW. A new constitutive framework for arterial wall mechanics and a comparative study of material models. *J. Elasticity* 2000; **61**:1–48.

[57] Stary HC, Blankenhorn DH, Chandler AB, Glagov S, Insull Jr W, Richardson M, Rosenfeld ME, Schaffer SA, Schwartz CJ, Wagner WD, *et al.*. A definition of the intima of human arteries and of its atherosclerosis-prone regions. A report from the committee on vascular lesions of the council on arteriosclerosis, American Heart Association. *Circulation* 1992; **85**:391–405.

[58] Holzapfel GA, Sommer G, Gasser CT, Regitnig P. Determination of the layer-specific mechanical properties of human coronary arteries with non-atherosclerotic intimal thickening, and related constitutive modelling. *Am. J. Physiol. Heart Circ. Physiol.* 2005; **289**:H2048–2058.

[59] Sommer G, Gasser TC, Regitnig P, Auer M, Holzapfel GA. Dissection of the human aortic media: an experimental study. *J. Biomech. Eng.* 2008; **130**:021 007–1–12.

[60] von der Mark K. Localization of collagen types in tissues. *Int. Rev. Conn. Tiss. Res.* 1981; **9**:265–324.

[61] Schriefl AJ, Zeindlinger G, Pierce DM, Regitnig P, Holzapfel GA. Determination of the layer-specific distributed collagen fiber orientations in human thoracic and abdominal aortas and common iliac arteries. *J. R. Soc. Interface* 2012; **9**:1275–1286.

[62] Patel DJ, Fry DL. The elastic symmetry of arterial segments in dogs. *Circ. Res.* 1969; **24**:1–8.

[63] Roach MR, Burton AC. The reason for the shape of the distensibility curves of arteries. *Canad. J. Biochem. Physiol.* 1957; **35**:681–690.

[64] Nichols WW, O'Rourke MF. *McDonald's Blood Flow in Arteries. Theoretical, Experimental and Clinical Principles*, chap. 4. 4th edn., Arnold: London, 1998; 73–97.

[65] Oktay HS, Kang T, Humphrey JD, Bishop GG. Changes in the mechanical behavior of arteries following balloon angioplasty. *ASME 1991 Biomechanics Symposium, AMD-Vol. 120*, Spilker RL, Friedman MH (eds.), The American Society of Mechanical Engineers, 1991.

[66] Block PC. Mechanism of transluminal angioplasty. *Am. J. Cardiol.* 1984; **53**:69C–71C.

[67] Holzapfel GA, Schulze-Bauer CAJ, Stadler M. Mechanics of angioplasty: Wall, balloon and stent. *Mechanics in Biology*, Casey J, Bao G (eds.), The American Society of Mechanical Engineers (ASME): New York, 2000. AMD-Vol. 242/BED-Vol. 46, pp. 141–156.

[68] Canfield TR, Dobrin PB. Static elastic properties of blood vessels. *Handbook of Bioengineering*, Skalak R, Chien S (eds.), McGraw-Hill: New York, 1987.

[69] Halloran BG, Davis VA, McManus BM, Lynch TG, Baxter BT. Localization of aortic disease is associated with intrinsic differences in aortic structure. *J. Surg. Res.* 1995; **59**:17–22.

[70] Hai CM, Murphy RA. Cross-bridge phosphorylation and regulation of latch state in smooth muscle. *J. Appl. Physiol.* 1988; **254**:C99–106.

[71] Yu SN, Crago PE, Chiel HJ. A nonisometric kinetic model for smooth muscle. *Am. J. Physiol.* 1997; **272(3 Pt 1)**:C1025–C1039.

[72] Stålhand J, Klarbring A, Holzapfel GA. A mechanochemical 3D continuum model for smooth muscle contraction under finite strains. *J. Theor. Biol.* 2011; **268**:120–130.

[73] Murtada SC, Arner A, Holzapfel GA. Experiments and mechanochemical modeling of smooth muscle contraction: significance of filament overlap. *J. Theor. Biol.* 2012; **297**:176Ű–186.

[74] Wolinsky H, Glagov S. Structural basis for the static mechanical properties of the aortic media. *Circ. Res.* 1964; **14**:400–413.

[75] Mangell P, Länne T, Sonesson B, Hansen F, Bergqvist D. Regional differences in mechanical properties between major arteries – an experimental study in sheep. *Eur. J. Vasc. Endovasc. Surg.* 1996; **12**:189–195.

[76] Holzapfel GA, Sommer G, Regitnig P. Anisotropic mechanical properties of tissue components in human atherosclerotic plaques. *J. Biomech. Eng.* 2004; **126**:657–665.

[77] Sonesson B, Hansen F, Stale H, Länne T. Compliance and diameter in the human abdominal aorta – the influence of age and sex. *Eur. J. Vasc. Surg.* 1993; **7**:690–697.

[78] Stergiopulos N, Vulliémoz S, Rachev A, Meister JJ, Greenwald SE. Assessing the homogeneity of the elastic properties and composition of the pig aortic media. *J. Vasc. Res.* 2001; **38**:237–246.

[79] Thoma R. Über die Abhängigkeit der Bindegewebsneubildung in der Arterienintima von den mechanischen Bedingungen des Blutumlaufes: Erste Mitteilung. *Virchows Arch. path. Anat.* 1883; **93**:443–505.

[80] Thoma R. Über die Strömung des Blutes in der Gefässbahn und die Spannung der Gefässwand: I. Teil. *Beitr. Path. Anat. Allg. Pathol.* 1920; **66**:92–158.

[81] Wolkoff K. Über die histologische Struktur der Coronararterien des menschlichen Herzens. *Virchows Arch. path. Anat.* 1923; **241**:42–58.

[82] Wolkoff K. Über die Altersveränderungen der Arterien bei Tieren. *Virchows Arch.* 1924; **252**:208–228.

[83] Andrus SB, Portman OW. Comparative studies of spontaneous and experimental atherosclerosis in primates. *Some Recent Developments in Comparative Medicine*, T-W-Fiennes RN (ed.). Academic Press: London, 1966; 161–177.

[84] Geer JC, McGill Jr HC, Robertson WB, Strong JP. Histologic characteristics of coronary artery fatty streaks. *Laboratory Investigation* 1968; **18**:565–570.

[85] Jaffe D, Hartroft WS, Manning M, Eleta G. Coronary arteries in newborn children: Intimal variations in longitudinal sections and the relationships to clinical and experimental data. *Acta Paediatr. Scand. Suppl.* 1971; **219**:3–28.

[86] McGill HC. The lesion. *Atherosclerosis III*, Schettler G, Weizel A (eds.). Springer-Verlag: Berlin, 1974; 27–38.

[87] Zarins CK, Giddens DP, Bharadvaj BK, Sottiurai VS, Mabon RF, Glagov S. Carotid bifurcation atherosclerosis. quantitative correlation of plaque localization with flow velocity profiles and wall shear stress. *Circ. Res.* 1983; **53**:502–514.

[88] Caro CG, Parker KH, Fish PJ, Lever MJ. Blood flow near the arterial wall and arterial disease. *Clin. Hemorheol.* 1985; **5**:849–871.

[89] Glagov S, Zarins CK. Is intimal hyperplasia an adaptive response or a pathological process? Observations on the nature of nonatherosclerotic intimal thickening. *J. Vasc. Surg.* 1989; **10**:571–573.

[90] Tabas I, Williams KJ, Boren J. Subendothelial lipoprotein retention as the initiating process in atherosclerosis: update and therapeutic implications. *Circulation* 2007; **116**:1832–1844.

[91] Libby P. Vascular biology of atherosclerosis: overview and state of the art. *Am. J. Cardiol.* 2003; **91**:3A–6A.

[92] Libby P, Ridker PM, Hansson GK. Progress and challenges in translating the biology of atherosclerosis. *Nature* 2011; **473**:317–325.

[93] Schriefl AJ, Collins MJ, Pierce DM, Holzapfel GA, Niklason LE, Humphrey JD. Remodeling of intramural thrombus and collagen in an Ang-II infusion ApoE-/- model of dissecting aortic aneurysms. *Thromb. Res.* 2012; **130**:e139–e146.

[94] Stary HC, Chandler B, Guyton JR, Insull Jr W, Rosenfeld ME, Schaffer SA, Schwartz CJ, Wagner WD, Wissler RW. A definition of initial, fatty streak, and intermediate lesions of atherosclerosis. A report from the committee on vascular lesions of the council on arteriosclerosis, American Heart Association. *Arterioscler. Thromb.* 1994; **14**:840–856.

[95] Stary HC, Chandler AB, Dinsmore RE, Fuster V, Glagov S, Insull Jr W, Rosenfeld ME, Schwartz CJ, Wagner WD, Wissler RW. A definition of advanced types of atherosclerotic lesions and a histological classification of atherosclerosis. A report from the committee on vascular lesions of the council on arteriosclerosis, American Heart Association. *Circulation* 1995; **92**:1355–1374.

[96] Hirsch AT, Haskal ZJ, Hertzer NR, Bakal CW, Creager MA, Halperin JL, Hiratzka LF, Murphy WRC, Olin JW, Puschett JB, *et al.*. ACC/AHA 2005 practice guidelines for the management of patients with peripheral arterial disease (lower extremity, renal, mesenteric, and abdominal aortic): a collaborative report from the american association for vascular surgery/society for vascular surgery, society for cardiovascular angiography and interventions, society for vascular medicine and biology, society of interventional radiology, and the ACC/AHA task force on practice guidelines (writing committee to develop guidelines for the management of patients with peripheral arterial disease): endorsed by the american association of cardiovascular and pulmonary rehabilitation; national heart, lung, and blood institute; society for vascular nursing; transatlantic inter-society consensus; and vascular disease foundation. *Circulation* 2006; **113**:e463–e654.

[97] Thompson RW, Geraghty PJ, Lee JK. Abdominal aortic aneurysms: basic mechanisms and clinical implications. *Curr. Prob. Surg.* 2002; **39**:110–230.

[98] McPhee JT, Hill JS, Eslami MH. The impact of gender on presentation, therapy, and mortality of abdominal aortic aneurysm in the United States, 2001-2004. *J. Vasc. Surg.* 2007; **45**:891–899.

[99] Lederle FA, Johnson GR, Wilson SE, Chute EP, Littooy FN, Bandyk D, Krupski WC, Barone GW, Acher CW, Ballard DJ. Prevalence and associations of abdominal aortic aneurysm detected through screening. aneurysm detection and management (ADAM) veterans affairs cooperative study group. *Ann. Intern. Med.* 1997; **15**:441–449.

[100] Alcorn HG, Wolfson Jr SK, Sutton-Tyrrell K, Kuller LH, O'Leary D. Risk factors for abdominal aortic aneurysms in older adults enrolled in The Cardiovascular Health Study. *Arterioscler. Thromb. Vasc. Biol.* 1996; **16**:963–970.

[101] Blanchard JF. Epidemiology of abdominal aortic aneurysms. *Epidemiol. Rev.* 1999; **21**:207–221.

[102] Thompson RW, Curci JA, Ennis TL, Mao D, Pagano MB, Pham CTN. Pathophysiology of abdominal aortic aneurysms: insights from the elastase-induced model in mice with different genetic backgrounds. *Ann. N. Y. Acad. Sci.* 2006; **1085**:59–73.

[103] Thompson RW. Basic science of abdominal aortic aneurysms: emerging therapeutic strategies for an unresolved clinical problem. *Curr. Opin. Cardiol.* 1996; **11**:504–518.

[104] Koch AE, Haines GK, Rizzo RJ, Radosevich JA, Pope RM, Robinson PG, Pearce WH. Human abdominal aortic aneurysms. immunophenotypic analysis suggesting an immune-mediated response. *Am. J. Pathol.* 1990; **137**:1199–1213.

[105] Hance KA, Tataria M, Ziporin SJ, Lee JK, Thompson RW. Monocyte chemotactic activity in human abdominal aortic aneurysms: role of elastin degradation peptides and the 67-kd cell surface elastin receptor. *J. Vasc. Surg.* 2002; **35**:254–261.

[106] Aggarwal S, Qamar A, Sharma V, Sharma A. Abdominal aortic aneurysm: A comprehensive review. *Exp. Clin. Cardiol.* 2011; **16**:11–15.

[107] Humphrey JD, Holzapfel GA. Mechanics, mechanobiology, and modeling of human abdominal aorta and aneurysms. *J. Biomech.* 2012; **45**:805–814.

[108] Blank RD, Boskey AL. Genetic collagen diseases: influence of collagen mutations on structure and mechanical behavior. *Collagen. Structure and Mechanics*, Fratzl P (ed.), Springer-Verlag: Heidelberg, 2008; 447–474.

[109] Marini JC, Forlino A, Cabral WA, Barnes AM, San Antonio JD, Milgrom S, Hyland JC, Körkkö J, Prockop DJ, De Paepe A, *et al.*. Consortium for osteogenesis imperfecta mutations in the helical domain of type I collagen: regions rich in lethal mutations align with collagen binding sites for integrins and proteoglycans. *Hum. Mutat.* 2007; **28**:209–221.

[110] Kuivaniemi H, Tromp G, Prockop DJ. Mutations in fibrillar collagens (types I, II, III, and XI), fibril-associated collagen (type IX), and network-forming collagen (type X) cause a spectrum of diseases of bone, cartilage, and blood vessels. *Hum. Mutat.* 1997; **9**:300–315.

[111] Marini JC. Osteogenesis imperfecta. *Primer on the Metabolic Bone Diseases and Disorders of Mineral Metabolism*, Favus MJ (ed.). American Society for Bone and Mineral Research: Washington, DC, 2006; 418–420.

[112] Phillips CL, Shrago-Howe AW, Pinnell SR, Wenstrup RJ. A substitution at a non-glycine position in the triple-helical domain of pro alpha 2(I) collagen chains present in an individual with a variant of the Marfan syndrome. *J. Clin. Invest.* 1990; **86**:1723–1728.

[113] Mayer SA, Rubin BS, Starman BJ, Byers PH. Spontaneous multivessel cervical artery dissection in a patient with a substitution of alanine for glycine (G13A) in the alpha 1 (I) chain of type I collagen. *Neurology* 1996; **47**:552–556.

[114] Gensure RC, Mäkitie O, Barclay C, Chan C, Depalma SR, Bastepe M, Abuzahra H, Couper R, Mundlos S, Sillence D, *et al.*. A novel COL1A1 mutation in infantile cortical hyperostosis (Caffey disease) expands the spectrum of collagen-related disorders. *J. Clin. Invest.* 2005; **115**:1250–1257.

[115] Fung YC. Elasticity of soft tissues in simple elongation. *Am. J. Physiol.* 1967; **213**:1532–1544.

[116] Fung YC. Biomechanics: its scope, history, and some problems of continuum mechanics in physiology. *Appl. Mech. Rev.* 1968; **21**:1–20.

[117] Fung YC. Stress-strain-history relations of soft tissues in simple elongation. *Biomechanics: Its Foundations and Objectives*, Fung YC, Perrone N, Anliker M (eds.). Prentice-Hall, Inc., Englewood Cliffs: New Jersey, 1971; 181–208. Chapter 7.

[118] Fung YC, Fronek K, Patitucci P. Pseudoelasticity of arteries and the choice of its mathematical expression. *Am. J. Physiol.* 1979; **237**:H620–H631.

[119] Fung YC. On the foundations of biomechanics. *J. Appl. Mech.* 1983; **50**:1003–1009.

[120] Holzapfel GA. *Nonlinear Solid Mechanics. A Continuum Approach for Engineering*. John Wiley & Sons: Chichester, 2000.

[121] Gundiah N, Ratcliffe MB, Pruitt LA. Determination of strain energy function for arterial elastin: Experiments using histology and mechanical tests. *J. Biomech.* 2007; **40**:586–594.

[122] Gasser TC, Ogden RW, Holzapfel GA. Hyperelastic modelling of arterial layers with distributed collagen fibre orientations. *J. R. Soc. Interface* 2006; **3**:15–35.

[123] O'Rourke M. Mechanical principles in arterial disease. *Hypertension* 1995; **26**:2–9.

[124] Wolinsky H, Glagov S. Comparison of abdominal and thoracic aortic medial structure in mammals. deviation of man from the usual pattern. *Circ. Res.* 1969; **25**:677–686.

[125] Humphrey JD, Canham PB. Structure, mechanical properties and mechanics of intracranial saccular aneurysms. *J. Elasticity* 2000; **61**:49–81.

[126] Länne T, Sonesson B, Bergqvist D, Bengtsson H, Gustafsson D. Diameter and compliance in the male human abdominal aorta: influence of age and aortic aneurysm. *Eur. J. Vasc. Surg.* 1992; **6**:178–184.

[127] Valentín A, Humphrey JD, Holzapfel GA. A multi-layered computational model of coupled elastin degradation, vasoactive dysfunction, and collagenous stiffening in aortic aging. *Ann. Biomed. Eng.* 2011; **39**:2027Ű–2045.

[128] Faber M, Möller-Hou G. The human aorta. Part V. Collagen and elastin in the normal and hypertensive aorta. *Acta Pathol. Mic. Sc.* 1952; **31**:377.

[129] Dobrin PB. Mechanical properties of arteries. *Physiol. Rev.* 1978; **58**:397–460.

[130] Stålhand J. Determination of human arterial wall parameters from clinical data. *Biomech. Model. Mechanobiol.* 2009; **8**:141–148.

[131] Dobrin PB. Vascular mechanics. *Handbook of Physiology. Section 2: The Cardiovascular System*, vol. III, Shepherd JT, Abboud FM (eds.). American Physiological Society: Bethesda, 1983; 65–102.

[132] Baldock C, Gilpin CJ, Koster AJ, Ziese U, Kadler KE, Kielty CM, Holmes DF. Three–dimensional reconstructions of extracellular matrix polymers using automated electron tomography. *J. Struct. Biol.* 2002; **138**:130–136.

[133] Fratzl P, Misof K, Zizak I, Rapp G, Amenitsch H, Bernstorff S. Fibrillar structure and mechanical properties of collagen. *J. Struct. Biol.* 1998; **122**:119–122.

[134] Fratzl P. Collagen: structure and mechanics, an introduction. *Collagen: Structure and Mechanics*, Fratzl P (ed.), Springer, 2008; 1–13.

[135] Montes GS. Structural biology of the fibres of the collagenous and elastic systems. *Cell Biol. Int.* 1996; **20**:15–27.

[136] Wicker BK, Hutchens HP, Wu Q, Yeh AT, Humphrey JD. Normal basilar artery structure and biaxial mechanical behaviour. *Comput. Methods Biomech. Biomed. Engin.* 2008; **11**:539–551.

[137] Canham PB, Finlay HM, Dixon JG, Boughner DR, Chen A. Measurements from light and polarised light microscopy of human coronary arteries fixed at distending pressure. *Cardiovasc. Res.* 1989; **23**:973–982.

[138] Canham PB, Finlay HM, Dixon JG, Ferguson SE. Layered collagen fabric of cerebral aneurysms quantitatively assessed by the universal stage and polarized light microscopy. *Anat. Rec.* 1991; **231**:579–592.

[139] Finlay HM, McCullough L, Canham PB. Three-dimensional collagen organization of human brain arteries at different transmural pressures. *J. Vasc. Res.* 1995; **32**:301–312.

[140] Canham PB, Finlay HM, Tong SY. Stereological analysis of the layered collagen of human intracranial aneurysms. *J Microsc.* 1996; **183**:170–180.

[141] Canham PB, Talman EA, Finlay HM, Dixon JG. Medial collagen organization in human arteries of the heart and brain by polarized light microscopy. *Connect. Tissue Res.* 1991; **26**:121–134.

[142] O'Rourke MF, Blazek JV, Morreels CL, Krovetz LJ. Pressure wave transmission along the human aorta: Changes with age and in arterial degenerative desease. *Circ. Res.* 1968; **23**:567–579.

[143] Länne T, Hansen F, Mangell P, Sonesson B. Differences in mechanical properties of the common carotid artery and abdominal aorta in healthy males. *J. Vasc. Surg.* 1994; **20**:218–225.

[144] Montes GS, Junqueira LCU. The use of the picrosirius-polarization method for the study of the biopathology of collagen. *Mem. Inst. Oswaldo Cruz* 1991; **86**:1–11.

[145] Smith JFH, Canham PB, Starkey J. Orientation of collagen in the tunica adventitia of the human cerebral artery measured with polarized light and the universal stage. *J. Ultrastruct. Res.* 1981; **77**:133–145.

[146] Stary HC. *Atlas of Atherosclerosis: Progression and Regression*. 2nd edn., The Parthenon Publishing Group: Boca Raton, London, New York, Washington, D.C., 2003.

[147] Holzapfel GA. Arterial tissue in health and disease: Experimental data, collagen-based modeling and simulation, including aortic dissection. *Biomechanical Modelling at the Molecular, Cellular and Tissue Levels*, Holzapfel GA, Ogden RW (eds.), Springer-Verlag: Wien, New York, 2009; 259–343. CISM Courses and Lectures no. 508.

[148] Learoyd BM, Taylor MG. Alterations with age in the viscoelastic properties of human arterial walls. *Circ. Res.* 1966; **18**:278–292.

[149] Labrosse MR, Beller CJ, Mesana T, Veinot JP. Mechanical behavior of human aortas: Experiments, material constants and 3-D finite element modeling including residual stress. *J. Biomech.* 2009; **42**:996–1004.

[150] Landuyt M. Structural quantification of collagen fibers in abdominal aortic aneurysms. Master's Thesis, KTH Solid Mechanics, Stockholm, and Department of Civil Engineering, Gent 2006.

[151] Stary HC. Composition and classification of human atherosclerotic lesions. *Virchows Archiv A Pathol. Anat.* 1992; **421**:277–290.

[152] Humphrey JD, Strumpf RK, Yin FCP. Determination of constitutive relation for passive myocardium: II. Parameter estimation. *J. Biomech. Eng.* 1990; **112**:340–346.

[153] Holzapfel GA, Ogden RW. On planar biaxial tests for anisotropic nonlinearly elastic solids. a continuum mechanical framework. *Math. Mech. Solids* 2009; **14**:474–489.

[154] Weisstein EW. Erfi. MathWorld–A Wolfram Web Resource 2011; `http://mathworld.wolfram.com/Erfi.html`.

[155] Holzapfel GA, Ogden RW. Constitutive modelling of arteries. *Proc. R. Soc. Lond. A* 2010; **466**:1551–1597.

[156] Finlay HM, Dixon JG, Canham PB. Fabric organization of the subendothelium of the human brain artery by polarized-light microscopy. *Arterioscler. Thromb.* 1991; **11**:681–690.

[157] Haskett D, Johnson G, Zhou A, Utzinger U, Vande Geest J. Microstructural and biomechanical alterations of the human aorta as a function of age and location. *Biomech. Model. Mechanobiol.* 2010; **9**:725–736.

[158] Holzapfel GA, Sommer G, Auer M, Regitnig P, Ogden RW. Layer-specific 3D residual deformations of human aortas with non-atherosclerotic intimal thickening. *Ann. Biomed. Eng.* 2007; **35**:530–545.

[159] Li AE, Kamel I, Rando F, Anderson M, Kumbasar B, Lima JAC, Bluemke DA. Using MRI to assess aortic wall thickness in the multiethnic study of atherosclerosis: Distribution by race, sex, and age. *Am. J. Roentgenology* 2004; **182**:593–597.

[160] Purinya BA, Kas'yanov VA. Mechanical properties of the wall of the human abdominal aorta after endarterectomy. *Mech. Comp. Mat.* 1975; **11**:598–602.

[161] Milewicz DM, Guo DC, Fadulu VT, Lafont AL, Papke CL, Inamoto S, Kwartler CS, Pannu H. Genetic basis of thoracic aortic aneurysms and dissections: Focus on smooth muscle cell contractile dysfunction. *Annu. Rev. Genomics Hum. Genet.* 2008; **9**:283–302.

[162] Sakalihasan N, Limet R, Defawe OD. Abdominal aortic aneurysm. *Lancet* 2005; **365**:1577–1589.

[163] Humphrey JD, Taylor CA. Intracranial and abdominal aortic aneurysms: similarities, differences, and need for a new class of computational models. *Annu. Rev. Biomed. Eng.* 2008; **10**:221–246.

[164] Vorp DA. Biomechanics of abdominal aortic aneurysm. *J. Biomech.* 2007; **40**:1887–1902.

[165] Daughtery A, Cassis LA. Mouse models of abdominal aortic aneurysms. *Arterioscler. Thromb. Vasc. Biol.* 2004; **24**:429–434.

[166] Barisione C, Charnigo R, Howatt DA, Moorleghen JJ, Rateri DL, Daugherty A. Rapid dilatation of the abdominal aorta during infusion of angiotensin II detected by noninvasive high-frequency ultrasound. *J. Vasc. Surg.* 2006; **44**:372–376.

[167] Cao RY, St Amand TS, Ford MD, Piomelli U, Funk CD. The murine angiotensin II-induced abdominal aortic aneurysm model: rupture risk and inflammatory progression patterns. *J. Pathol.* 2010; **1**:1–7.

[168] Cassis LA, Gupte M, Thayer S, Zhang X, Charnigo R, Howatt DA. ANG II infusion promotes abdominal aortic aneurysms independent of increased blood pressure in hypercholesterolemic mice. *Am. J. Physiol. Heart Circ. Physiol.* 2009; **296**:H1660–H1665.

[169] Goergen CJ, Azuma J, Barr KN, Magdefessel L, Kallop DY, Gogineni A, Grewall A, Weimer RM, Connolly AJ, Dalman RL, *et al.*. Influences of aortic motion and curvature on vessel expansion in murine experimental aneurysms. *Arterioscler. Thromb. Vasc. Biol.* 2011; **31**:270–279.

[170] Luo J, Fujikura F, Tyrie LS, Tilson MD, Konofagou EE. Pulse wave imaging of normal and aneurysmal abdominal aortas in vivo. *IEEE Trans. Med. Imaging* 2009; **28**:477–486.

[171] Rateri DL, Howatt DA, Moorleghen JJ, Charnigo R, Cassis LA, Daughtery A. Prolonged infusion of angiotensin II in apoe(-/-) mice promotes macrophage recruitment with continued expansion of abdominal aortic aneurysm. *Am. J. Pathol.* 2011; **179**:1542–1548.

[172] Rush C, Nyara M, Moxon JV, Trollope A, Cullen B, Golledge J. Whole genome expression analysis within the angiotensin II - apolipoprotein E deficient mouse model of abdominal aortic aneurysm. *BMC Genomics* 2009; **10**:298.

[173] Saraff K, Babamusta F, Cassis LA, Daugherty A. Aortic dissection precedes formation of aneurysms and atherosclerosis in angiotensin-II infused, apolipoprotein E-deficient mice. *Arterioscler. Thromb. Vasc. Biol.* 2003; **23**:1621–1626.

[174] Satoh K, Nigro P, Matoba T, O'Dell MR, Cui Z, Shi X, Mohan A, Yan C, Abe J, Illig KA, *et al.*. Cyclophilin A enhances vascular oxidative stress and the development of angiotensin II-induced aneurysms. *Nat. Med.* 2009; **15**:649–656.

[175] Trachet B, Renard M, De Santis G, Staelens S, De Backer J, Antiga L, Loeys B, Segers P. An integrated framework to quantitatively link mouse-specific hemodynamics to aneurysm formation in angiotensin II-infused ApoE -/- mice. *Ann. Biomed. Eng.* 2011; **39**:2430–2444.

[176] Daugherty A, Cassis LA, Lu H. Complex pathologies of angiotensin II-induced abdominal aortic aneurysms. *J. Zhejiang Univ. Sci. B* 2011; **12**:624–628.

[177] Humphrey JD. *Cardiovascular Solid Mechanics. Cells, Tissues, and Organs*. Springer-Verlag: New York, 2002.

[178] Genovese K, Collins MJ, Lee YU, Humphrey JD. Regional finite strains in an angiotensin II induced mouse model of dissecting abdominal aortic aneurysms. *Cardiovasc. Engr. Tech.* 2012; **3**:194–202.

[179] Xia Y, Elder K. Quantification of the graphical details of collagen fibrils in transmission electron micrographs. *J Microsc.* 2001; **204**:2–16.

[180] Bayan C, Levitt JM, Miller E, Kaplan D, Georgakoudi I. Fully automated, quantitative, noninvasive assessment of collagen fiber content and organization in thick collagen gels. *J. Appl. Physics* 2009; **105**:1–11.

[181] Collins M, Bersi M, Wilson E, Humphrey JD. Mechanical properties of suprarenal and infrarenal abdominal aorta: implications for mouse models of aneurysms. *Med. Eng. Phys.* 2011; **33**:1262–1269.

[182] Hinz B, Phan SH, Thannickal VJ, Galli A, Bochaton-Pillat ML, Gabbiani G. The myofibroblast: one function, multiple origins. *Am. J. Pathol.* 2007; **170**:1807–1816.

[183] Tomasek JJ, Gabbiani G, Hinz B, Chaponnier C, Brown RA. Myofibroblasts and mechano-regulation of connective tissue remodeling. *Nat. Rev. Mol. Cell Bio.* 2002; **3**:349–363.

[184] Wang DHJ, Makaroun MS, Webster MW, Vorp DA. Effect of intraluminal thrombus on wall stress in patient-specific models of abdominal aortic aneurysm. *J. Vasc. Surg.* 2002; **36**:598–604.

[185] Tieu BC, Lee C, Sun H, Lejeune W, Recinos III A, Ju X, Spratt H, Guo DC, Milewicz D, Tilton RG, *et al.*. An adventitial IL-6/MCP-1 amplification loop accelerates macrophage-mediated vascular inflammation leading to aortic dissection in mice. *J. Clin. Invest.* 2009; **119**:3637–3651.

[186] Bersi MR, Collins MJ, Wilson E, Humphrey JD. Disparate changes in the mechanical properties of murine carotid arteries and aorta in response to chronic infusion of angiotensin-II. *Int. J. Adv. Eng. Sci. Appl. Math.* 2012; In press.

[187] Mehta PK, Griendling KK. Angiotensin-II cell signaling: physiological and pathological effects in the cardiovascular system. *Am. J. Phys.* 2007; **292**:C82–97.

[188] Grond-Ginsbach C, Pjontek R, Aksay SS, Hyhlik-Durr A, Bockler D, Gross-Weissmann ML. Spontaneous arterial dissection: phenotype and molecular pathogenesis. *Cell Mol. Life Sci.* 2010; **67**:1799–1815.

[189] Bode-Jänisch S, Schmidt A, Günther D, Stuhrmann M, Fieguth A. Aortic dissecting aneurysms Ű histopathological findings. *Forensic Sci. Int.* 2012; **214**:13–17.

[190] Clough RE, Hussain T, Uribe S, Greil GF, Razavi R, Taylor PR, Schaeffter R, Waltham M. A new method for quantification of false lumen thrombosis in aortic dissection using magnetic resonance imaging and a blood pool contrast agent. *J. Vasc. Surg.* 2011; **54**:1251–1258.

[191] Deng GG, Martin-McNulty B, Sukovich DA, Freay A, Halks-Miller M, Thinnes T, Loskutoff DJ, Carmeliet P, Dole WP, Wang YX. Urokinase-type plasminogen activator plays a critical role in angiotensin II-induced abdominal aortic aneurysm. *Circ. Res.* 2003; **92**:510–517.

[192] Lijnen HR. Plasmin and matrix metalloproteinases in vascular remodeling. *Thromb. Haemost.* 2001; **86**:324–333.

[193] Song SW, Yoo KJ, Kim DK, Cho BK, Yi G, Chang BC. Effects of early anticoagulation on the degree of thrombosis after repair of acute DeBakey type I aortic dissection. *Ann. Thorac Surg.* 2011; **92**:1367–1375.

[194] Fineschi V, Turillazzi E, Neri M, Pomara C, Riezzo I. Histological age determination of venous thrombosis: a neglected forensic task in fatal pulmonary thromboembolism. *Forensic Sci. Int.* 2009; **186**:22–28.

[195] Irniger W. Histologische Altersbestimmung von Thrombosen und Embolien. *Virchows Arch. path. Anat.* 1963; **336**:220–237.

[196] Karsaj I, Humphrey JD. A mathematical model of the evolvingmechanical properties of intraluminal thrombus. *Biorheology* 2010; **46**:509–527.

[197] Lee D, Yuki I, Murayama Y, Chiang A, Nishimura I, Vinters HV, Wang CJ, Nien YL, Ishii A, Wu BM, *et al.*. Thrombus organization and healing in the swine experimental aneurysm model. Part I. A histological and molecular analysis. *J. Neurosurg.* 2007; **107**:94–108.

[198] Folkesson M, Silveira A, Eriksson P, J JS. Protease activity in the multilayered intraluminal thrombus of abdominal aortic aneurysms. *Atherosclerosis* 2011; **218**:294–299.

[199] Houard X, Rouzet F, Touat Z, Philippe M, Dominguez M, Fontaine V, Sarda-Mantel L, Meulemans A, Le Guludec D, Meilhac O, *et al.*. Topology of the fibrinolytic system within the mural thrombus of human abdominal aortic aneurysms. *J. Pathol.* 2007; **212**:20–28.

[200] Maiellaro K, Taylor WR. The role of the adventitia in vascular inflammation. *Cardiovasc. Res.* 2007; **75**:640–648.

[201] Tiessen IM, Roach MR. Factors in the initiation and propagation of aortic dissections in human autopsy aortas. *J. Biomech. Eng.* 1993; **115**:123–125.

[202] Holzapfel GA, Ogden RW. Modelling the layer-specific 3D residual stresses in arteries, with an application to the human aorta. *J. R. Soc. Interface* 2010; **7**:787–799.

[203] Holzapfel GA, Gasser TC. A viscoelastic model for fiber-reinforced composites at finite strains: Continuum basis, computational aspects and applications. *Comput. Meth. Appl. Mech. Eng.* 2001; **190**:4379–4403.

[204] Weisbecker H, Pierce DM, Regitnig P, Holzapfel GA. Layer-specific damage experiments and modeling of human thoracic and abdominal aortas with non-atherosclerotic intimal thickening. *J. Mech. Behav. Biomed. Mater.* 2012; **12**:93–106.

[205] Ateshian GA, Rajan V, Chahine NO, Canal CE, Hung CT. Modeling the matrix of articular cartilage using a continuous fiber angular distribution predicts many observed phenomena. *J. Biomech. Eng.* 2009; **131**:61 003.

[206] Federico S, Gasser TC. Nonlinear elasticity of biological tissues with statistical fibre orientation. *J. R. Soc. Interface* 2010; **7**:955–966.

[207] Slaaf DW, Tangelder GJ, oude Egbrink MGA, Reneman RS. *Clinically Applied Microcirculation Research*, Barker JH, Anderson GL, Meneger MD (eds.), CRC Press: London, 1995; 391–405.

[208] Masters BR, So PT. Antecedents of two-photon excitation laser scanning microscopy. *Microsc. Res. Tech.* 2004; **63**:3–11.

[209] Stoller P, Reiser M, Cellier PM, Rubenchik AM. Polarization-modulated second harmonic generation in collagen. *Biophys. J.* 2002; **82**:3330–3342.

[210] Campagnola PJ, Loew LM. Second-harmonic imaging microscopy for visualizing biomolecular arrays in cells, tissues and organisms. *Nat. Biotechnol.* 2003; **21**:1356–1360.

[211] Randen T, Husoy JH. Filtering for texture classification: A comparative study. *IEEE Trans. Pattern Anal. Mach. Intell.* 1999; **21**:291–310.

[212] Kim A, Lakshman N, Petroll WM. Quantitative assessment of local collagen matrix remodeling in 3-D culture: the role of Rho kinase. *Exp. Cell Res.* 2006; **312**:3683Ű–3692.

[213] Chiu YW, Lo MT, Tsai MR, Chang YC, Hsu RB, Yu HY, Sun CK, Ho YL. Applying harmonic optical microscopy for spatial alignment of atrial collagen fibers. *PLoS One* 2010; **5**:e13 917.

[214] Timmins LH, Wu Q, Yeh AT, Moore Jr JE, Greenwald SE. Structural inhomogeneity and fiber orientation in the inner arterial media. *Am. J. Physiol. Heart Circ. Physiol.* 2010; **298**:1537–Ű1545.

[215] Lilledahl MB, Pierce DM, Ricken T, Holzapfel GA, de Lange Davies C. Structural analysis of articular cartilage using multiphoton microscopy: input for biomechanical modeling. *IEEE Trans. Med. Imaging* 2011; **30**:1635–1648.

[216] Mardia KV, Jupp PE. *Directional Statistics*. John Wiley & Sons, Ltd, 1999.

[217] Evans M, Hastings N, Peacock B. *Statistical Distribution*. John Wiley & Sons: New York, 2000.

[218] Lyons L. *Statistics for Nuclear and Particle Physicists*. Cambridge University Press: Cambridge, 1989.

[219] Kohavi R, Sahami M. Error-based and entropy-based discretization of continuous features. *Proceedings of the Second International Conference on Knowledge Discovery and Data Mining*, vol. 237, 1996; 114–Ű119.

[220] Erdogmus D, Principe JC. Comparison of entropy and mean square error criteria in adaptive system training using higher order statistics. *Proceedings of ICA*, 2000; 75–80.

[221] Erdogmus D, Principe JC. Convergence properties and data efficiency of the minimum error entropy criterion in ADALINE training. *IEEE T. Signal Process.* 2003; **51**:1966–Ű1978.

[222] Lanir Y. Constitutive equations for fibrous connective tissues. *J. Biomech.* 1983; **16**:1–12.

[223] Chatterjee S, Hadi AS. *Regression Analysis by Example*. John Wiley & Sons: New Jersey, 2006.

[224] Mow VC, Gu WY, Chen FH. Structure and function of articular cartilage and meniscus. *Basic Orthopaedic Biomechanics & Mechano-Biology*, Mow VC, Huiskes R (eds.), Lippincott Williams & Wilkins: Philadelphia, 2005; 181–258. 3rd edition.

[225] Sankaran S, Marsden AL. A stochastic collocation method for uncertainty quantification and propagation in cardiovascular simulations 2011; **133**:031 001.

[226] Matusita K. Decision rules, based on the distance, for problems of fit, two samples, and estimation. *Ann. Math. Statist.* 1955; **26**:631–640.

[227] Kailath T. The divergence and Bhattacharyya distance measures in signal selection. *IEEE T. Commun.* 1967; **15**:52–60.

[228] Cha SH, Srihari SN. On measuring the distance between histograms. *Pattern Recognition* 2002; **35**:1355–1370.

[229] Kullback S, Leibler RA. On information and sufficiency. *Ann. Math. Statist.* 1951; **22**:79–Ű86.

[230] Genina EA, Bashkatov AN, Tuchin VV. Tissue optical immersion clearing. *Expert Rev. Med. Devices* 2010; **7**:825–842.

[231] Cicchi R, Sampson D, Massi D, Pavone F. Contrast and depth enhancement in two-photon microscopy of human skin ex vivo by use of optical clearing agents. *Opt. Express* 2005; **13**:2337–2344.

[232] Hirshburg JM, Ravikumar KM, Hwang W, Yeh AT. Molecular basis for optical clearing of collagenous tissues. *J. Biomed. Opt.* 2010; **15**:055 002.

[233] Hama H, Kurokawa H, Kawano H, Ando R, Shimogori T, Noda H, Fukami K, Sakaue-Sawano A, Miyawaki A. Sca/e: a chemical approach for fluorescence imaging and reconstruction of transparent mouse brain. *Nat. Neurosci.* 2011; **14**:1481–1488.

[234] Ragan T, Sylvan JD, Kim KH, Huang H, Bahlmann K, Lee RT, So PT. High-resolution whole organ imaging using two-photon tissue cytometry. *J. Biomed. Opt.* 2007; **12**:014 015.

[235] Valentín A, Holzapfel GA. Constrained mixture models as tools for testing competing hypotheses in arterial biomechanics: A brief survey. *Mech. Res. Commun.* 2012; **42**:126–133.

[236] Humphrey JD, Delange SL. *An Introduction to Biomechanics, Solids and Fluids, Analysis and Design*. Springer-Verlag: New York, 2004.

[237] Schriefl AJ, Reinisch AJ, Sankaran S, Pierce DM, Holzapfel GA. Quantitative assessment of collagen fiber orientations from 2D images of soft biological tissues. *J. R. Soc. Interface* 2012; **9**:3081–3093.

[238] Spalteholz W. *Über das Durchsichtigmachen von menschlichen und tierischen Präparaten und seine theoretischen Bedingungen*. S. Hirzel: Leipzig, 1914.

[239] Zucker RM. Whole insect and mammalian embryo imaging with confocal microscopy: morphology and apoptosis. *Cytometry A* 2006; **69**:1143–1152.

[240] Watton PN, Hill NA, Heil M. A mathematical model for the growth of the abdominal aortic aneurysm. *Biomech. Model. Mechanobiol.* 2004; **3**:98–113.

[241] Gasser TC, Gallinetti S, Xing X, Forsell C, Swedenborg J, Roy J. Spatial orientation of collagen fibers in the abdominal aortic aneurysm's wall and its relation to wall mechanics. *Acta Biomater.* 2012; **8**:3091–3103.